Dissertation
submitted to the
Combined Faculty of Natural Sciences and Mathematics
of the Ruperto Carola University Heidelberg, Germany
for the degree of
Doctor of Natural Sciences

Presented by
M. Sc. Physics
Giulia Paci
Zevio, Italy
20.12.2018

Deciphering the multi–step nuclear transport of viral cargoes

Referees: Dr. Martin Beck
Prof. Dr. Ulrich Schwarz

Summary

Transport of molecules between the nucleus and the cytoplasm is tightly regulated by the nuclear pore complex (NPC), the "gatekeeper" of the nucleus. NPCs allow passage of small molecules (< 4 nm), whereas larger cargoes can only cross the permeability barrier if they are bound to nuclear transport receptors (NTRs), which recognize specific nuclear import and export signals (NLSs and NESs) on their surface. Among the thousands of molecules that travel through the NPC, an important class is represented by large cargoes (> 15 nm), such as pathogens, mRNAs and pre–ribosomal subunits. Strikingly, it has been observed that NPCs can accommodate Hepatitis B virus capsids of 36 nm in size, almost comparable with the dimensions of the transport channel. The mechanism for the transport of cargoes with such exceptional size are still unclear, especially the role of multivalent NTR binding.

In my PhD thesis I characterized the nuclear import properties of large cargoes in cells. In order to do so, I firstly developed a large cargo model suitable for nuclear transport studies based on virus-like particles. It comprises more than 20 different cargoes with size range 18–36 nm and different amount of NLSs exposed on their surface. Following the development of a semi-automatic kinetic cellular transport assay, I have shown that large cargoes require a minimum number of bound NTRs in order to achieve productive entry into the nucleus, and I further found evidence of a linear relationship between #NLSs and import efficiency. Moreover, the experiments revealed that the minimum threshold for import increases non-linearly with size, reaching up to an unprecedented 100 NTRs per cargo and pointing to a high drop in the transport efficiency for cargoes > 25 nm, which could represent a previously undescribed “second gate” at the NPC.

In order to go beyond the global picture from bulk import kinetics, I developed a super resolution microscopy setup and LabVIEW software for high–resolution studies of large cargo import in cells. Performing dual-color super–resolution imaging of nucleoporins and cargoes, I have shown that HBV capsids specifically dock on NPCs and interact with both the cytoplasmic component and directly with the permeability barrier. Additional single-particle tracking experiments allow me to follow the import process with high spatiotemporal resolution, dissecting the multiple steps involved in large cargo import. Integrating this knowledge with the findings from bulk kinetics studies and super-resolution microscopy paves the way for an integrated view of large cargo transport through the NPC.

Zusammenfassung

Der Transport von Molekülen zwischen Zellkern und Zytoplasma wird durch den Kernporenkomplex (NPC), den „Torhüter“ des Zellkerns, streng kontrolliert. NPCs erlauben den Durchgang von kleinen Molekülen (< 4 nm), während größere Moleküle die Permeabilitätsbarriere nur durchqueren können, wenn sie an einen Kerntransportrezeptor (NTR) gebunden sind, welcher spezifische Kernimport – und exportsignale (NLSs und NESs) auf der Oberfläche des Moleküls erkennt. Unter den Tausenden von Molekülen, die den NPC passieren, wird eine wichtige Klasse durch große Moleküle (> 15 nm) repräsentiert, zu denen Pathogene, mRNAs und preribosomale Untereinheiten gehören. Bemerkenswerterweise wurde festgestellt, dass NPCs Hepatitis B Virus Kapside mit einem Durchmesser von 36 nm, was fast mit den Dimensionen des zentralen Kanals selbst vergleichbar ist, aufnehmen können. Der Transportmechanismus von Kargos mit einer solch außergewöhnlichen Größe und vor allem die Rolle der multivalenten NTR-Bindung ist bisher noch nicht gut verstanden. Zunächst habe ich ein großes Kargo–Modell, welches für Kerntransportstudien basierend auf Virus–ähnlichen Partikeln geeignet ist, entwickelt. Es beinhaltet 20 verschiedene Kargos im Größenbereich von 18–36 nm und unterschiedlicher Anzahl an NLSs. Der Entwicklung einer halb-automatischen kinetischen zellulären Transportbestimmung folgend, habe ich gezeigt, dass große Kargos eine minimale Anzahl von gebunden NTRs benötigen, um einen produktiven Eintritt in den Nukleus zu erreichen. Des Weiteren, habe ich einen Zusammenhang zwischen der #NLSs und der Importeffizienz gefunden. Außerdem haben die Experimente offenbart, dass der Minimal-Grenzwert für den Import nichtlinear mit der Größe steigt. Dies weist auf ein mögliches, zuvor unbeschriebenes "zweites Tor" für Kargos > 25 nm für den NPC Transport hin.
Um über das globale Bild von Ensemble-Importkinetiken hinaus zu gehen, habe ich einen Mikroskop-Aufbau und eine LabVIEW–Software zur hochauflösenden Studie für den Import von großen Kargos in Zellen entwickelt. Mit dem Ausführen von zwei-Farben Super-Auflösungsabbildungen, habe ich gezeigt, dass HBV Kapside spezifisch an NPCs binden und sowohl mit zytoplasmatischen Komponenten, wie auch direkt mit der Permeabilitätsbarriere interagieren. Zusätzliche Einzel–Molekül–Experimente erlauben mir den Importprozess mit einer hoch raumzeitlichen Auflösung zu verfolgen und dabei die verschiedenen Schritte, die beim Transport von großen Molekülen involviert sind, zu unterteilen. Das Zusammenbringen dieses Wissens aus verschiedenen Technologien ebnet den Weg für einen ganzheitlichen Blick auf den Transport von großen Molekülen durch den NPC.

Publication List

1. Kozma, E., **Paci, G.**, Estrada Girona G., Lemke, E. A. & Kele, P. (2018). Fluorogenic tetrazine-siliconrhodamine probe for the labeling of non-canonical amino acid tagged proteins. *Methods in Molecular Biology*, 1728, 337–363.

2. Kozma, E., Estrada Girona G., **Paci, G.**, Lemke, E. A. & Kele, P. (2017). Bioorthogonal Double-Fluorogenic Siliconrhodamine Probes for Intracellular Super–Resolution Microscopy. *Chemical Communications*, 53 (50), 6696–6699.

3. **Paci G.**, Lemke, E. A. (2017). Shining a light on phase separation in the cell. *Cell*, 168 (1), 11-13.

4. Nikić, I., Estrada Girona, G., Kang, JH., **Paci, G.**, Mikhaleva, S., Koehler, C., Shymanska, N., Ventura Santos, C., Spitz, D., Lemke, E. A. (2016). Debugging Eukaryotic Genetic Code Expansion for Site-Specific Click-PAINT Super-Resolution Microscopy. *Angewandte Chemie International Edition*, 55 (52), 16172–16176.

5. Sakin, V., **Paci, G.**, Lemke, E. A., & Müller, B. (2016). Labeling of virus components for advanced, quantitative imaging analyses. *FEBS letters*, 590 (13), 1896–1914.

Contents

List of Figures

List of Tables

List of Abbreviations

AFM: Atomic Force Microscopy
BSA: Bovine Serum Albumin
DMSO: Dimethyl sulfoxide
DTT: Dithiothreitol
EDTA: Ethylenediaminetetraacetic acid
EM: Electron Microscopy
FBS: Fetal Bovine Serum
FCS: Fluorescence Correlation Spectroscopy
FG: Phenylalanine-Glycine
FRAP: Fluorescence Recovery After Photobleaching
FRET: Förster Resonance Energy Transfer
GDP: Guanosine-5′-diphosphate
GFP: Green Fluorescent Protein
GTP: Guanosine-5′-triphosphate
HILO: Highly Inclined and Laminated Optical sheet
IBB: Importinβ Binding domain
Impα: importinα
Impβ: importinβ
IPTG: Isopropyl β-D-1-thiogalactopyranoside
kDa: Kilo Dalton
LB: Lysogeny Broth
MBP: Maltose Binding Protein
MSD: Mean Squared Displacement
NES: Nuclear Export Signal
NLS: Nuclear Localization Signal
NPC: Nuclear Pore Complex
NTR: Nuclear Transport Receptor
Nup: Nucleoporin
OD: Optical Density
PBS: Phosphate buffer saline
PEG: Polyethylene glycol
PEI: Polyethylenimine
PFA: Paraformaldehyde
PMSF: Phenylmethane sulfonyl fluoride
PP: Polypropylene

QD : Quantum Dot
PDB: Protein Data Bank
TCEP: Tris(2-carboxyethyl)phosphine
TFF: Tangential Flow Filtration
TIRF: Total Internal Reflection Fluorescence
WGA: Wheat Germ Agglutinin

1 Introduction

1.1 The Nuclear Pore Complex

The Nuclear Pore Complex (NPC) is one of the largest macromolecular complexes in eukaryotic cells, with an estimated mass of 125 MDa [1] and formed by multiple copies of around 30 different proteins called nucleoporins (Nups). The main function of the NPC is to regulate the exchange of molecules (proteins, RNAs...) between the cytoplasm and the nucleus. Beyond physiological nucleocytoplasmic transport, the NPC plays an important role in viral infection (see [2] and [3] a review). Viruses hijack the host cellular machinery in order to replicate and spread infection, and most DNA viruses and some RNA viruses replicate in the nucleus of the host cell. Thus they must deliver their genome (and often viral proteins) to the nucleus, often exploiting the NPC and the transport machinery. NPCs also play a role in regulating chromatin organization and gene expression. Defects in the NPC itself or in the nuclear transport pathway have been associated with many diseases such as cardiomyopathies and various cancers (see [4] for a review).

1.1.1 Structure of the Nuclear Pore Complex

The structure of the NPC is characterized by a central donut–shaped scaffold, embedded in the nuclear envelope, from which flexible peripheral structures protrude both into the cytoplasm and nucleoplasm (see schematic representation in Figure 1.1). Details of the NPC scaffold structure have been clarified by many studies in recent years, combining techniques such as biochemical analyses, super–resolution microscopy, electron microscopy and X–ray crystallography [5, 6, 7, 8]. Its organization is highly modular, as different subcomplexes occur in multiple copies and assemble according to a 8–fold rotational symmetry into three stacked rings: two outer rings on the cytoplasmic and nuclear sides and an inner ring, leaving a central channel of $\approx$ 40 nm in diameter. This channel is filled by intrinsically disordered Nups, which are anchored to the NPC scaffold and constitute approximately $1/3$ of all Nups. These proteins lack a stable secondary or tertiary structure, and they are often referred to as FG-Nups for their high content in phenylalanine-glycine (FG) repeats. FG-Nups form the permeability barrier of the NPC, which allows selective control of nucleocytoplasmic transport, as will be discussed in sections 1.1.2 and 1.2.3. On the nuclear side of the NPC, FG-Nups form a flexible structure called nuclear basket [9]. On the cytoplasmic side, another flexible structure formed by FG-Nups is present, often referred to as cytoplasmic filaments. Even though these are typically represented as long filaments protruding into the cytoplasm, their structure is not yet well–characterized.

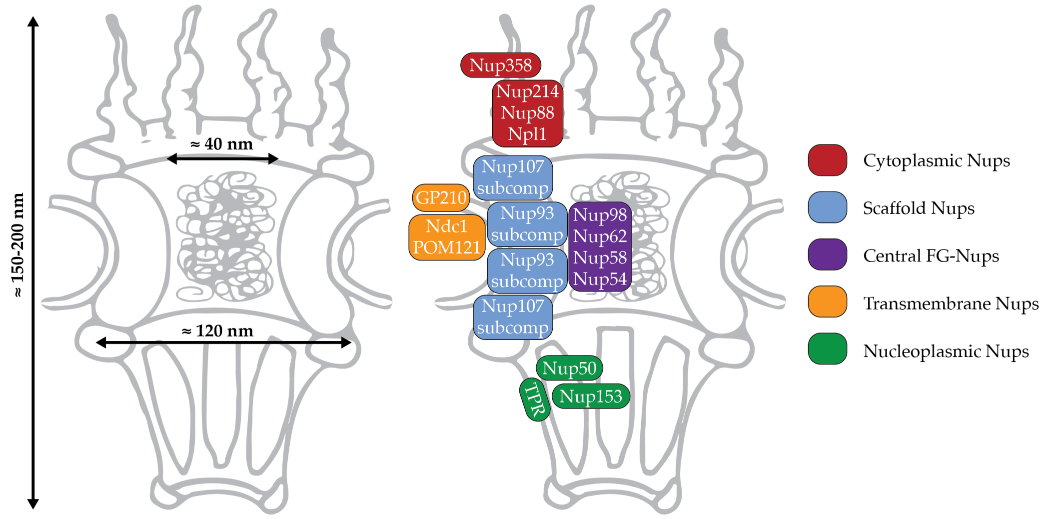

FIGURE 1.1: Scheme of the NPC structure and composition, with relevant sizes indicated on the left side and the main classes of Nups with their localization on the right. Note that Nups are frequently named according to their molecular weight (in kDa).

Plasticity of the NPC

While the last decade has witnessed a breakthrough in terms of our understanding of the NPC structure, there is a growing body of evidence that the NPC is not a "one size fits all" fixed structure, but it can present a high degree of structural plasticity and compositional variability. For example, dramatic and reversible channel diameter changes up to 35% have been observed with atomic force microscopy (AFM) of nuclear envelopes incubated with the amphipathic alcohol *trans*–cyclohexane–1,2-diol (TCHD), which is known to disrupt the interaction between FG-Nups and cause a collapse of the permeability barrier [10]. Changes in channel width and depth have also been detected as consequence of incubation with different alcohols and transport receptors [11], and dilated pore conformations have been recently reported within intact HeLa cells using cryo–electron tomography [12]. In addition to a certain structural flexibility of NPCs, it has been observed that NPCs can also have a "compositional" variability. The NPC stoichiometry has been shown to vary depending on the cell type [13], and NPCs exceeding the typical 8–fold symmetry had also previously been observed [14]. From an evolutionary point of view, NPC subcomplexes are highly conserved in vertebrates and other eukaryotes (see [15] for a review), however the final NPC assembly can present substantial differences. For example, it has been suggested that the yeast NPC has fewer copies of the Y–complex compared to the human case [16], and a recent structural study of the NPC in the early branching eukaryote alga *Chlamydomonas reinhardtii* [17] found a distinct architecture with a much wider central channel ($\approx$ 60 nm) and an asymmetric density between the nuclear and cytoplasmic rings. To what degree these different NPC conformations play a role in nuclear transport, especially for cargoes of large size, still remains to be determined.

1.1.2 Models of the NPC permeability barrier

Due to their highly dynamic nature, FG-Nups are extremely challenging to study: for this reason, the organization of these proteins in the central channel of the NPC has so far remained elusive. Several models have been proposed to describe the arrangement of FG-Nups and the subsequent effect on the mode of nuclear transport; the main ones are briefly outlined below in chronological order. More details about the nuclear transport process will be discussed in section 2.2.

Selective phase/hydrogel model

The idea that FG-Nups inside the central NPC channel can form a selective "meshwork" in virtue of their mutual interactions was first introduced by Ribbeck [18]. Small molecules would be able to freely diffuse through the meshwork, whereas larger cargoes would need to transiently dissolve the FG-FG network in order to cross the NPC. Subsequent studies showed that purified FG-domain of yeast Nups can form hydrogels with permeability barrier properties [19, 20]. Several other FG-Nups have then been found to phase separate and form hydrogels [21, 22, 23], however the applicability of the hydrogel state *in vivo* remains debated.

Oily spaghetti model

In the "oily spaghetti" model, introduced by Macara [24], FG-Nups fill the central channel quite loosely, leaving a central open "tube" of around 10 nm in diameter. Molecules smaller than this size can freely diffuse through the NPC, whereas larger cargoes bound to transporter molecules "push" FG-Nups aside and move through the NPC with a series of binding and unbinding events.

Virtual gate model

This model from Rout [25] considers that the high confinement inside the NPC central channel results in a restricted movement of the molecules passing through it and therefore in a reduction of their entropy. The densely packed FG-Nups further increase the entropic cost of inserting a molecule within the central channel. The resulting energy barrier blocks cargoes of significant size, unless they can lower it via the enthalpy of binding to FG–Nups.

Reduction of dimensionality model

In this model, introduced by Peters [26], FG repeats form a layer which lines the NPC walls in their entirety. Fast translocation of cargo–transporter complexes is attributed to a reduction of dimensionality effect: once bound to FG repeats, the cargoes slide along the NPC channel with a 2D random walk. This motion results in a faster search process to find the NPC "exit" compared to a 3D random walk, and therefore faster crossing times. In this model, hydrophilic unfolded peptide chains form a selective barrier in the NPC channel, leaving a 8–10 nm wide "tube" for the free diffusion of small molecules.

Polymer brush model

Experiments with surface–tethered FG domains have found that they can form an extended polymer brush [27], which can reversibly collapse upon exposure to transporter proteins [28]. These observations led to the formulation of a model in which elongated FG-Nups form a entropic barrier inside the NPC, that can be collapsed by cargo-transporter complexes in order to achieve NPC crossing.

Forest model

This model introduced by Yamada [29] takes into account that FG-Nups have an heterogeneous composition and that they can be classified into two families based on their charge content, a concept along what introduced in [30]. One class of FG-Nups with low charge content adopts a collapsed coil configuration, on the other hand FG-Nups with higher charge content form extended coils with fewer mutual interactions. The uneven distribution of these two types of FG-Nups inside the NPC gives rise to two distinct "zones" of transport: a central transporter where FG-Nups can rapidly deform to allow passage of large cargoes, and a peripheral "zone" occupied mainly by transporter molecules and small cargoes.

Kap–centric model

There is growing evidence that transporter molecules should be considered as an integral part of the permeability barrier, together with FG-Nups. This kap–centric view on nuclear transport is motivated by the high concentration of these proteins in cells, which have a high affinity for FG-Nups (in the nM–μM range [31, 32, 33]). Several biophysical studies looked at the interaction of surface–grafted FG–Nups with NTRs employing surface plasmon resonance [34, 35] and found that binding of NTRs to FG domains strongly depended on NTR occupancy within the FG–domain layer. A recent study in digiton–permeabilized cells [36] found evidence of two different pools of the transporter importinβ, one with high turnover and one very long-lived (several minutes). Further supporting arguments to consider transporters as integral part of the permeability barrier come from experiments in which an increase in their concentration has been seen to correlate with higher import rates [37, 38].

Another model (albeit not significantly discussed in the field anymore) is the affinity gradient model proposed by Gerace [31], based on a progressively increasing affinity of impβ for Nups along the transport channel.
Due to the complexities of probing the organization and dynamics of FG-Nups *in vivo*, it has so far been challenging to evaluate the validity of the models described above and reach a conclusion on the nature of the permeability barrier of the NPC. It is likely that the NPC operates via a combination of the mechanisms described above, due to the polymer nature of FG-Nups which can display different conformations ranging from cohesive to repellent interactions.

1.2 Nucleocytoplasmic transport

The main function of the NPC is to act as the "gatekeeper" between the nucleus and the cytoplasm, blocking undesired molecules, while at the same time allowing selective transport of up to 1000 molecules per second [18]. There are two main mechanism of transport through the NPC: passive and facilitated diffusion. Small cargoes (up to $\approx$ 40 kDa) can freely diffuse through the NPC permeability barrier, however the passage of larger molecules is hindered. These larger cargoes are transported via facilitated diffusion, by binding to nuclear transport receptors (NTRs), which recognize the nuclear localization and export signal peptides (NLSs and NESs) displayed by the cargo. In this thesis I focus on facilitated diffusion, as it is the most relevant transport mechanism for large cargoes.

It is important to note that, in recent years, it has been suggested that the NPC might form a "soft" permeability barrier, causing an increasing obstruction to large passive cargoes, but without a strict size cutoff [39]. It has also been shown that NPC crossing can depend quite dramatically on the cargo surface properties, which allows them to interact with FG-Nups. Bovine serum albumin (BSA), which is usually excluded from the nucleus, was able to cross the NPC once modified with hydrophobic amino–acid analogues [40], and a recent study based on extensive surface mutation of GFP has found that hydrophobic residues, as well as cysteines, histidines and charged arginines, have a strong translocation–promoting effect [41].

1.2.1 Nuclear transport receptors and nuclear localization signals

Nuclear localization and export signals are relatively short amino acid sequences that target cargoes for nuclear import or export: classical NLSs are characterized by the presence of basic charged amino acids like arginine and lysine, whereas non–classical ones lack basic residues. Classical NLSs (on which I focus in this thesis) can be monopartite, containing a single stretch of basic amino acids, or bipartite (two stretches of basic amino acids spaced by a linker). An example of classical monopartite NLS is the one from the Simian Virus 40 T antigen: PKKKRK [42].

Nuclear transport receptors bind to NLSs and NESs on the cargoes and facilitate their transport into and out of the nucleus by interacting with FG-Nups. Depending on their directionality, NTRs are often referred to as importins and exportins, even though some of them can act bidirectionally [43, 44]. The human β–karyopherin superfamily includes around 20 different NTRs, which are characterized by the presence of several HEAT-repeats arranged into a super–helix (see [45] for a review). The most intensively studied member of this superfamily is importinβ (impβ). The structure of impβ is quite flexible, which facilitates its binding to different substrates [46, 47, 48]. Impβ does not bind directly to the cargo NLS, but it requires the adaptor molecule impα. This 55-kDa protein is formed by stacked Armadillo (ARM) repeats, which confer more rigidity to its structure. Impα has a 40 amino acid impβ binding (IBB) domain at its N–terminus, which is autoinhibitory: structural studies have shown that in absence of NLS cargo the IBB occupies a large part of the NLS binding pocket [49] (see Figure 1.2 A). The requirement of an adaptor molecule for some importins might have evolved in order to add a further regulation layer to the transport machinery: in absence of cargoes to be transported, impα is not targeted to the nucleus, and in absence of available impβ for transport, impα does not bind the cargo. When both NLS cargo and impβ are present, the IBB domain is likely competed off the NLS binding groove, enabling the formation of the ternary import complex (see Figure 1.2 B). This can then be transported into the nucleus, as the NTRs can interact with the FG-Nups forming the permeability barrier, as will be discussed in more detail in section 1.2.3.

1.2.2 Overview of the nuclear import cycle

The main steps of the import cycle in the case of the classical NLS system are represented schematically in Figure 1.3. The process starts in the cytoplasm, with the formation of the import complex by the cargo, impα and impβ. The ternary complex then crosses the NPC barrier and, once in the nuclear basket, impβ is released by RanGTP. Impβ-RanGTP then shuttles back into the cytoplasm, whereas impα also requires the presence of the transport factor CAS in order to be dissociated from the cargo and recycled for another round of import [50, 51]. The release of RanGTP from impα and impβ is mediated in the cytoplasm by RanGAP and RanBP. Directionality of nuclear transport is established by a gradient of the two forms of Ran [52]: the cytoplasm is enriched in GDP-bound Ran and the nucleus in the GTP-bound form. This asymmetric distribution is established by the localization of the RanGTPase activating protein (RanGAP) in the cytoplasm and the Ran guanine nucleotide exchange factor RCC1 into the nucleus. RanGAP activates the GTPase–activity of Ran, converting RanGTP to RanGDP, and conversely RCC1 converts RanGDP, which is imported into the nucleus by NTF2, into RanGTP.

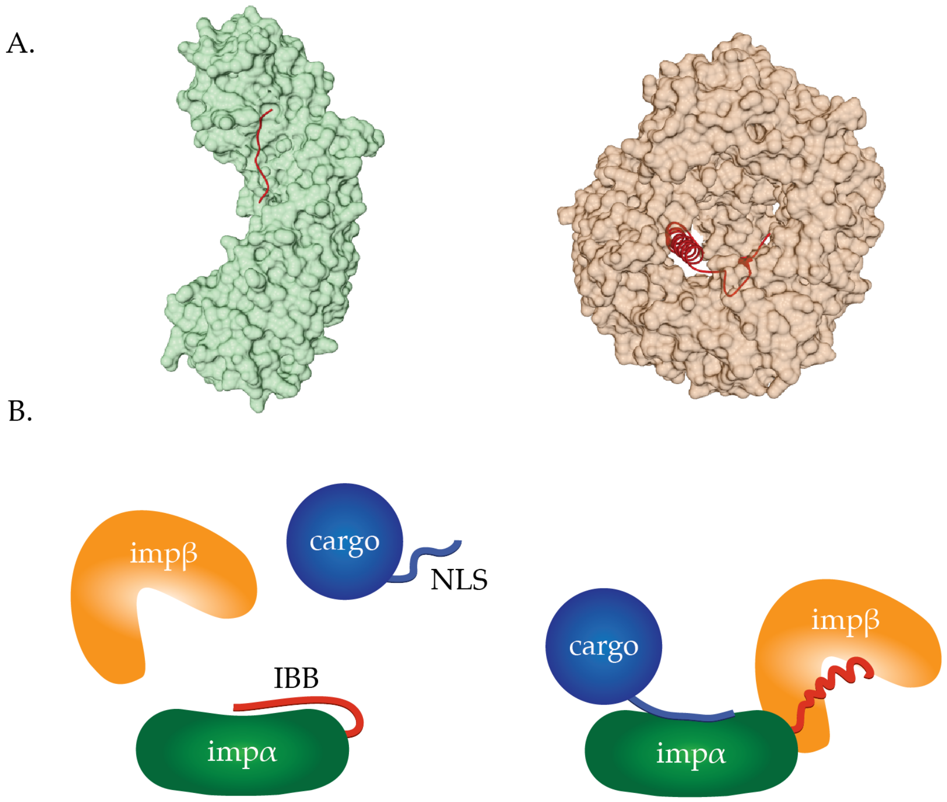

FIGURE 1.2: Molecular basis of import complex formation. (A) Autoinhibited conformation of impα (left), with the IBB highlighted in red (PDB: 1IAL). On the right, impβ bound to the IBB (PDB: 1QGK). (B) Scheme of the autoinhibitory function of impα IBB, which normally occupies the NLS–binding groove (left). Only in presence of both impβ and NLS–cargo the IBB is competed off, allowing formation of the transport complex (right).

1.2.3 Mechanism of permeability barrier crossing

As previously introduced, facilitated diffusion of cargoes through the NPC is enabled by NTRs, which can bind to FG-Nups via multiple hydrophobic grooves on their surface [53, 54, 55]. One key feature of nuclear transport is that it is at the same time fast (molecules can cross the NPC in few milliseconds) and selective. For long time it has been puzzling how NTRs with multivalent binding to FG-Nups can rapidly cross the highly concentrated NPC central channel, which presents a high number of binding partners (the FG concentration is estimated to be $\approx$ 160 mM [56]). Recent work [57, 58, 59] has shed light on this apparent "transport paradox" by showing that FG-Nups interact with NTRs via multiple low–affinity contacts which allow FG-Nups to maintain high plasticity also in the bound state. In this way, the interactions are transient enough to allow the rapid exchange of FG–motifs from the different NTR binding pockets and enable rapid transport of the cargo–NTR complex. Another study [60] supported this view and also proposed a "slide and exchange" mechanism where FG-Nups can "slide" in and out of binding pockets on

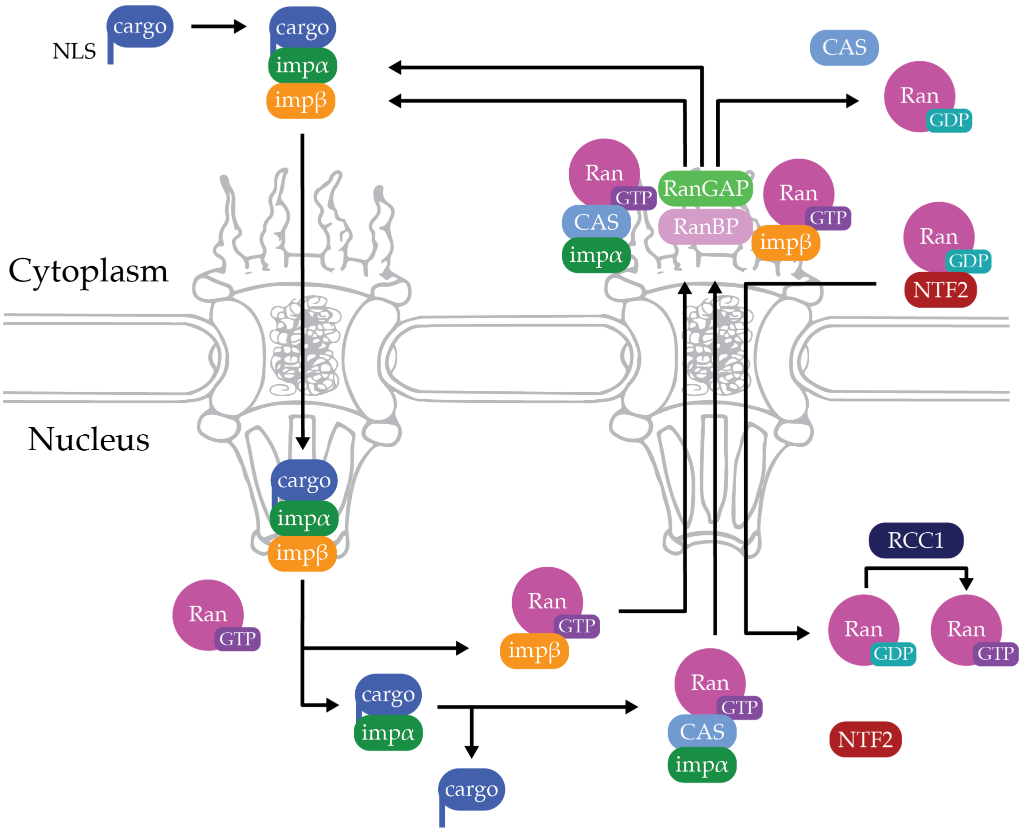

FIGURE 1.3: Simplified scheme of the nuclear import cycle.

the NTRs and transition from a strongly interacting state into a weakly interacting state, promoting fast exchange of FG–motifs through competitive displacement.

1.2.4 Experimental studies of nuclear transport

Much of our current understanding of the molecular basis of nuclear transport (e.g. formation of the transport complex, interaction of FG–Nups with NTRs) has come from biochemical and *in vitro* studies. In order to gain a more comprehensive view on nuclear transport in the physiological cellular environment, several model systems and techniques have been employed to characterize this process at increasing levels of biological complexity.

Model systems

Since the first observation of NPCs in the 1950s [61], different model systems have been used to investigate the NPC permeability barrier and nuclear transport. One of the first *in vitro* assays that allowed the study of many nuclear processes is the nuclear reconstitution extract derived from *Xenopus laevis* eggs, developed in the 1980s [62, 63, 64]. One advantage of this system is that individual Nups can be depleted prior to reconstitution, or they can be substituted with engineered versions: this has allowed investigation of different NPC permeability phenotypes, also in cases which would be lethal in the physiological context [65]. Additionaly, intact nuclear envelopes from *Xenopus*, spread on a coverglass, have been used in several atomic force microscopy (AFM) studies of the NPC [66, 67] to investigate its nanomechanical properties.

In order to study nuclear transport in a more physiological context, microinjection in live cells has been widely employed both in *Xenopus* oocytes and cultured mammalian cells [68]. Another example of studies in live cells are based on the expression of fluorescent molecules fused to NLSs or NESs, for instance in yeast [38]. The advantage of these systems is that they allow observation of the transport process under physiological conditions, however the concentrations of different transport factors are often unknown and hard to control.

An intermediate level between the *in vitro* and the physiological systems is represented by studies in permeabilized mammalian cells. This method was introduced in 1990 [69] and is based on the permeabilisation of the plasma membrane by the detergent digitonin, which does not affect internal cellular membranes due to their low cholesterol content. The treatment thus leaves the nuclear envelope intact and functional and allows reconstitution of nuclear transport upon addition of cytosol and/or purified soluble transport factors [70]. The permeabilized cell system is ideal when one wishes to study nuclear transport in cells but at the same time control the availability of transport factors in order to gain a more quantitative understanding of the process.

Techniques used to study nuclear transport

Early studies of nuclear pore permeability relied on electron or fluorescence microscopy detection of injected colloidal particles or proteins conjugated to fluorescent dyes in large cells [71, 72]. Methods based on radiotracers and autoradiography were also developed [73]: an important study employing radiolabelled NLS peptides from SV40 crosslinked to BSA showed for the first time that the NLS sequence could on its own target an "engineered" protein to the nucleus [74]. In 1984, fluorescence microphotolysis allowed to estimate the functional pore size for passive diffusion in smaller–sized cells (live hepatocytes) [75]. Many studies followed in the next decade which employed confocal laser scanning microscopy to visualize fluorescent cargoes or transport receptors, often using the previously introduced permeabilized cell assay [76, 18, 52]. These studies offered better quantification of the import kinetics for different cargoes and characterized the role of several transport factors. Among other fluorescence-based techniques, quantitative fluorescence microscopy and FRAP (Fluorescence Recovery After Photobleaching) enabled the measurement of the nuclear influx/outflux of nucleoplasmin, which was shown to follow Michaelis–Menten kinetics [77].

Recent technical advancements in microscopy have allowed to reach enough sensitivity to detect single fluorescent molecules in biological systems (see [78] and [79] for a review). Single-particle tracking is based on the observation of the protein of interest in very diluted conditions, so that individual diffraction–limited spots corresponding to the molecule positions can be fitted at each time step. This allows the reconstruction of the particle trajectory, and the study of the different import steps at a high spatio–temporal resolution. Single–particle tracking has been employed to study the residence time and localization of several transport factors [80, 81, 50], as well as the transport of different cargoes [82, 83, 84]. I will describe more details of specific single–particle studies employing large cargoes in the following section.

1.3 Nuclear transport of large cargoes

Among the thousands of molecules which are continuously transported through the NPC, one important class of cargoes is characterized by their exceptional size. I refer to these as "large" cargoes, which represent the main focus of this thesis. A prominent group of such large cargoes with high biological relevance are viral cargoes, which will be described in more detail in section 1.3.1. Other important large cargoes that need to be transported across the NPC are the 40S and 60S pre–ribosomal subunits, which are approximately 25 nm in size and are exported into the cytoplasm during the maturation process. Many other species of RNA molecules also need to be exported into the cytoplasm, especially mRNAs. Complexes of RNAs with RNA–binding proteins can reach impressive sizes, as for example the $\approx$ 50 nm Balbiani ring mRNP particles [85].

1.3.1 Viral cargoes

As many viruses require transport of their genome into the host cell nucleus as part of their life cycle, they have evolved a wide set of strategies to evade or hijack the nuclear transport machinery (see [2] and [86] for a review). For example, some viruses dock at the cytoplasmic side of the NPC and release their genome into the nucleus (Herpesvirus) or disassemble at the NPC (adenoviruses). Others disrupt the nuclear envelope (parvoviruses) or cross the NPC as intact particles (Hepatitis B virus, baculoviruses). For other important human pathogens, such as HIV-1, the mechanism of nuclear import and capsid uncoating still remains unclear [87].

Among viral cargoes, one of the most well–characterized and intriguing cases is the Hepatitis B virus (HBV). HBV is an enveloped virus which enters the cell via endocytosis: the capsid containing partially double–stranded DNA is released in the cytoplasm and travels along microtubules towards the nucleus (reviewed in [88]). The HBV capsid is formed by a single 21 kDa protein (the core protein) which assembles into T=3[1] capsids of 32 nm containing 180 copies of the core protein and T=4 capsids of 36 nm containing 240 copies. It delivers the genome into the nucleus by exploiting the nuclear transport machinery: in fact, the arginine–rich C terminus of the core protein harbors two classical NLSs [89, 90]. The C terminus is usually not exposed but buried inside the capsid [91], and its exposure has been shown to be dependent on phosphorylation of the core protein (which in turn is linked to genome maturation). *In vitro* phosphorylated capsids have been shown to bind to the nuclear envelope in an impα and β dependent way [92], and the binding could be inhibited by NLS peptides, wheat germ agglutinin (WGA) and anti–NPC antibodies. Studies in *Xenopus* oocytes injected with phosphorylated HBV particles have also shown that the intact capsids could cross the NPC and reach the nuclear basket [93], which is impressive considering that the capsid diameter is very close to the central NPC channel (see Figure 1.4). Disassembly of the capsid at the nuclear basket and release of the genome seem to be related to genome maturation and involve direct interactions of the capsid with Nup153 [94, 95].

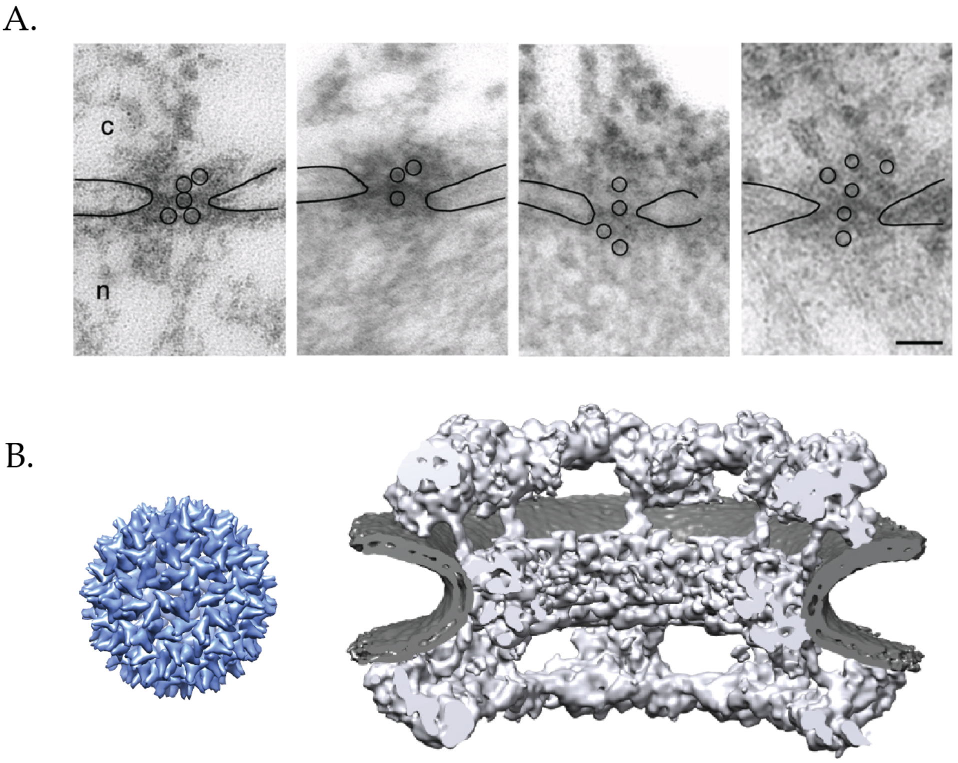

FIGURE 1.4: Nuclear import of HBV capsids. (A) EM micrographs from [93] showing HBV particles in the central NPC channel and in the nuclear basket. (B) Comparison of the HBV capsid (PDB: 1QGT) with the NPC scaffold structure [6]: the capsid diameter is comparable with the central NPC channel.

---

[1] T indicates the triangulation number, used to describe the subunit arrangement in capsids of icosahedral shape.

1.3.2 Previous studies on nuclear transport of large cargoes

When considering nuclear transport of large cargoes, one key question is how the cargo size affects its import efficiency and NPC crossing time. Intuitively, larger particles will have to displace many more FG-Nups in order to fit through the crowded NPC channel, and it might also be harder for them to dock at the cytoplasmic side and achieve productive channel entry. The effect of cargo size on NTR-mediated nuclear import has so far not been studied systematically for cargoes of very large size. The requirements for nuclear import of cargoes up to $\approx$ 700 kDa were investigated in [96]. The authors found that molecules larger than $\approx$ 500 kDa necessitated the presence of both Ran and GTP hydrolysis in order to be able to cross the NPC. In another study, coarse–grained simulation of nuclear transport allowed the authors to test a wide range of cargo sizes from 5 to 30 nm [97]. The simulations predicted a non–linear dependence of transport time with cargo size, with size having almost no effect on mean transport time for cargoes smaller than 15 nm.

One important feature of large cargoes is that they might require multiple bound NTRs in order to be effectively transported. This is supported by the fact that cargoes such as the HBV capsid can potentially expose an extremely high number of NLSs on their surface (up to 240). The idea that multivalent binding of NTRs to a single cargo can enhance its transport properties has been around for quite a long time. Experiments with pentameric nucleoplasmin already showed in 1982 that pentamers with five NLSs entered the nucleus 10 times faster than the ones with a single NLS [98]. Ribbeck and Görlich tested cargoes from 30 to 80 kDa in size and observed that the larger ones were more inefficiently imported into the nucleus [99]. When the largest cargo was tagged with two different NLSs targeting impβ and transportin, the authors observed a much more efficient import in presence of both NTRs. However, even the largest of these cargoes was still below 10 nm in size, quite far from the large biomolecules which are the focus of this thesis (> 15 nm).

The question of multivalent NTR binding on the transport of large cargoes has also been addressed by computational and theoretical studies. For instance, in [100], the authors perform coarse–grained molecular dynamics simulations to quantify the energy barrier that cargoes need to overcome to cross the NPC. They explicitly take into account the cargo size and model the multivalency of NTR binding by tuning the number of hydrophobic binding spots on the cargo surface. Their transport model predicts an optimal range of the number of hydrophobic spots depending on the size: too few binding spots would not be able to overcome the energy barrier to allow for transport, whereas too many would results into cargo "entrapment" due to an increased affinity. This description of large cargo transport is quite appealing, however "entrapment" has so far not been observed in biological experiments.

Single–particle tracking studies of large cargoes

Among previous studies of large cargo nuclear transport, the last 10 years have seen an increase of works employing high–resolution methods, such as single–particle tracking. These techniques enable the achievement of a much more detailed view of the transport process, by following single cargoes undergoing the different import/export steps at high spatiotemporal resolution.

Recombinant adeno–associated viruses of 23 nm in diameter were found to enter the nucleus of cells with an efficiency of 17% [101]. Tracking the capsids with high–speed super–resolution microscopy (SPEED) revealed an import time of 54 ms. However, it has been noted that interpretation of results from SPEED experiments is quite sensitive to experimental errors (arising from particle localization, registration and system stability) [102] so the findings should be taken with caution. Single–particle tracking was also employed to study transport of 25 nm mRNA [84] through NPCs. The authors developed a super–registration approach to precisely align the mRNA tracks to a NPC reference, reaching a 26 nm spatial precision. Results from the tracking experiments led to the formulation of a three–step transport model, consisting of docking, transport and release. Translocation through the central channel was found not be the rate limiting step, requiring only 5-20 ms compared to 80 ms for docking and release. To date, only very few high–resolution studies have looked at large cargo transport with systems where the bound NTRs or the exposed NLSs could be tuned quantitatively. As they are very relevant for the scope of this thesis, I will discuss their findings in more detail below.

One study [103] employed quantum dots (QDs) of 18 nm in diameter, functionalized with multiple copies of the IBB from snurportin-1. Such QD-IBB could bind up to 40 importinβ molecules, reaching a total diameter of 30 nm. The resulting cargo was imported quite inefficiently into permeabilized cells, so no bulk signal could be observed in the nucleus, however the authors could acquire 177 import events via single–particle tracking. The interaction time of QD-IBB with the NPC varied widely from few seconds to several minutes. Interestingly, QDs coated with 50% less IBB had a significantly longer dwell time at the NPC, arising from a slowing down of the cargo in the NPC channel.

In another study [104], the transport of a β–galactosidase cargo containing four M9 NLSs (recognized by the NTR transportin) was characterized using single–particle tracking in permeabilized cells. The cargo was $\approx$ 500 kDa and 18 x 15 x 9 nm in size. The interaction time of β–gal with the NPC was reported to be 8.7 ms, similar to the time measured for a much smaller cargo (2xGFP) albeit β–gal had a 50% lower import efficiency. A very interesting finding is that a single transportin bound per cargo enabled binding to the NPC but was insufficient for crossing the permeability barrier. To investigate the role of this multivalency effect, the authors developed a model of cargo transport in terms of diffusion in an effective free energy potential. In order to cross the permeability barrier, the cargo has to overcome the energy barrier of displacing the FG-Nups and potentially disrupting their interactions. In this framework, binding interactions between NTRs and FG-Nups lower the energy barrier felt by the transport complex. Multivalent binding results in a more significant barrier reduction, while the transiency of FG-Nups interactions with NTRs enables a fast crossing.

1.4 Objectives

Despite their high biological interest, nuclear transport of large cargoes is still poorly understood. In order to address the open questions experimentally, a suitable model system of large cargoes with defined size and NTR–binding potential is necessary. The overall goal of my thesis is to develop such a system and employ it in order to understand how the kinetics of large cargo import depend on the number of NLSs (and therefore of bound NTRs) and on size.

1.4.1 Development of a large cargo "toolkit" for nuclear import studies

My first aim is to develop a "toolkit" of biocompatible large cargoes of different defined sizes where the number of exposed NLSs can be tuned in a wide range. To do so, I intend to engineer different virus–like particles with NLS peptides bound to their surface. This will allow more controlled and quantitative analysis of the NLS number effect on import of large cargoes.

1.4.2 Effect of multiple NLSs on the transport of large cargoes

By taking advantage of the large cargo "toolkit", I then aim to quantitatively characterize the effect of different number of NLSs on the import kinetics of the large cargoes. In order to do so, I intend to develop a semi–automated imaging and analysis pipeline that will allow me to measure nuclear import in a large pool of cells at the same time. Comparing cargoes of different sizes will enable me to asses the interplay of two key parameters: NLS exposure and size. Furthermore, I aim to complement the ensemble kinetics experiment with single-particle tracking in order to gain more information on the individual transport steps. To do so, I will develop a TIRF/HILO microscopy setup and control software suitable for dual–color high–resolution studies in cells.

1.4.3 Large cargo localization at the NPC

The final aim of my thesis is to study the interaction of large cargoes at the NPC, especially looking at what changes are induced in the NPC structure itself. To do so, I aim to achieve a detailed picture of large cargo localization at the NPC, using super–resolution imaging on the previously designed setup. These experiments will also pave the way for studies of NPC plasticity during large cargo transport.

2 Materials and Methods

In this chapter I will describe the materials and methods employed to acquire and analyze the data presented in Chapter 3. Section 2.1 deals with the purification, labelling and characterization of the capsids which constitute the large cargo toolkit. In section 2.2 I describe the methods employed for nuclear transport assays in permeabilized cells, from the sample preparation to the image analysis step. Section 2.3 is devoted to the self–built experimental setup used to acquire super–resolution and single–particle tracking datasets. In section 2.4 I delineate the procedure for the acquisition and analysis of super–resolution and single–particle tracking data. Finally, section 2.5 contains the list of materials used in this study (plasmids, reagents, optical components).

2.1 Expression, purification and labelling of large cargoes

2.1.1 Expression and purification of MS2 and MS2-S37P capsids

Composition of buffers used for the purification:

- Lysis buffer: 10 mM Tris pH 7.5, 100 mM NaCl, 5 mM DTT, 1 mM $MgCl_2$, 1 mM PMSF

- Labelling buffer: 100 mM Tris pH 7.5, 100 mM NaCl, 0.2 mM TCEP, 5 mM EDTA

- SEC buffer: 10 mM Tris pH 7.5, 100 mM NaCl, 5 mM DTT

A colony of *E. coli* BL21 (DE3) AI cells containing the pBAD_MS2_Coat_Protein–(1–393) or the pBAD_MS2_Coat_Protein–(1–393)_S37P plasmids was inoculated in LB (Lysogeny Broth) medium containing 50 μg/ml ampicillin. The culture was grown overnight shaking at 37°C and then used at a 1:100 dilution to inoculate an expression culture in LB medium. Cells were incubated at 37°C while shaking. Once the culture had reached OD_{600}=0.6-0.7, protein expression was induced by adding 0.02% arabinose. The protein was expressed at 37°C shaking (180 rpm) for 4 hours. Cells were harvested by centrifugation in a Beckmann centrifuge, rotor JLA 8.100, at 4500 rpm for 20 min at 4°C. Cell pellets were transferred into 50 ml Falcon tubes, washed by resuspending them with PBS and then spun down at 5000 rpm for 15 min. Pellets were then either stored at -20°C or immediately used for purification.

For purification, pellets were resuspended in an equal volume of lysis buffer, sieved to remove clumps and lysed through 3-4 rounds in a microfluidizer (Microfluidics M110–L) at 4°C. The lysate was incubated with 0.2% PEI (Polyethylenimine) for 1 hour on ice and then clarified by centrifugation in a Beckmann centrifuge, rotor JA 25.50 at 10000 rpm for 30 min. A saturated solution of $(NH_4)_2SO_4$ was added at 4°C drop–wise to the clear lysate under continuous mild stirring up to 25% of ammonium sulphate. After 1 hour, the lysate was spun down in a Beckmann centrifuge, rotor JA 25.50 at 10000 rpm for 30 min. The supernatant was discarded, and the pellets were gently resupended with 10-20 ml lysis buffer on a rotator at room temperature. After resuspension, the lysate was again centrifuged with the rotor JA 25.50 at 10000 rpm for 30 min and the clear supernatant was collected. The supernatant was cleared using the KrosFlo (see section 2.1.4 for more details) with a 0.2 μm cutoff membrane to remove large impurities. The membrane permeate containing the cleared sample was collected on ice. In order to maximize protein retrieval, the remaining supernatant was washed with 50 ml of lysis buffer and the permeate was pooled with the previously collected one. The sample was then concentrated using the KrosFlo with a 500 kDa cutoff membrane (for the smaller MS2_S37P mutant, a 30 kDa cutoff membrane was used). The final sample was then labelled with dye/NLS peptide according to the procedure outlined in section 2.1.5. For long–term storage at -80°C, the sample was supplemented with 25% glycerol and flash–frozen with liquid nitrogen.

2.1.2 Expression and purification of I53-47 capsids

Composition of buffers used for the purification:

- Lysis buffer: 25 mM Tris pH 8.0, 250 mM NaCl, 20 mM imidazole, 1 mM PMSF, 0.2 mM TCEP
- Elution buffer: 25 mM Tris pH 8.0, 250 mM NaCl, 500 mM imidazole, 1 mM PMSF, 0.2 mM TCEP
- Dialysis buffer: 25 mM Tris pH 8.0, 150 mM NaCl 0.2 mM TCEP
- SEC buffer: 25 mM Tris pH 8.0, 150 mM NaCl, 1 mM DTT

A colony of *E. coli* BL21 (DE3) AI cells containing the pET29b(+)_I53–47A.1–B.3_D43C plasmid was inoculated in LB medium containing 50 μg/ml kanamycin. The culture was grown overnight shaking at 37°C and then used at a 1:100 dilution to inoculate an expression culture in LB medium. Protein expression was induced at OD_{600}=0.8 by adding 1 mM IPTG and carried out at 37°C shaking (180 rpm) for 3 hours. Cells were harvested by centrifugation in a Beckmann centrifuge, rotor JLA 8.100, at 4500 rpm for 20 min at 4°C. Cell pellets were transferred into 50 ml Falcon tubes, washed by resuspending them with PBS and then spun down at 5000 rpm for 15 min. Pellets were then either stored at -20°C or immediately used for purification.

The purification procedure was adapted from [105]. Pellets were resuspended in two pellet volumes of lysis buffer, sieved to remove clumps and supplemented with 1 mg/ml lysozyme and DNAse. Cells were lysed by sonication with a Branson sonifier 450, 3 times for 30 seconds, on ice. The sample was mixed between sonication cycles. The lysate was clarified by centrifugation in a Beckmann centrifuge, using the JA 25.50 rotor at 24000 g, for 35 min at 4°C. The clear lysate was then incubated with Ni–beads (1 ml/l expression) for 1-2 hours at 4°C under gentle rotation. Ni–beads with lysate were poured in a polypropylene (PP) column and the flow through (FT) was collected. Ni–beads were washed three times with 20 ml of lysis buffer followed by elution with 5 ml of elution buffer. The elution was immediately supplemented with 5 mM EDTA to prevent Ni–mediated aggregation of the sample. The buffer of the protein was then exchanged to dialysis buffer at 4°C: first for 2-3 h, then overnight with fresh buffer and again the next day for 4-5 h with fresh buffer. After dialysis, the protein was transferred to a new Falcon tube and spun down for 15 min at 5000 rpm and 4°C, in order to remove any precipitation. The protein was concentrated using the KrosFlo with a 100 kDa cutoff membrane, which also helps removing some of the unassembled capsid proteins. After concentrating down to 10 ml of volume, the sample was washed with 50 ml of dialysis buffer using the continuous buffer exchange mode of the KrosFlo. The final sample was then labelled with dye/NLS peptide according to the procedure outlined in section 2.1.5. For long–term storage, the sample was supplemented with 25% glycerol and directly transferred in a -80°C freezer.

2.1.3 Expression and purification of HBV capsids

Composition of buffers used for the purification:

- Lysis buffer: 25 mM Tris pH 7.5, 500 mM NaCl, 0.2 mM TCEP, 10 mM CHAPS
- Sucrose buffer: 25 mM Tris pH 7.5, 500 mM NaCl, 0.2 mM TCEP, 10 mM CHAPS, 60% sucrose
- SEC buffer: 25 mM Tris pH 7.5, 500 mM NaCl, 0.2 mM TCEP, 10 mM CHAPS, 10% sucrose

A colony of *E. coli* BL21 (DE3) AI cells containing the pET28a2-HBc14SH6_S81C plasmid (or the alternative HBV construct plasmids - see table in the Materials part) was inoculated in TB medium containing 50 μg/ml ampicillin. The culture was grown overnight shaking at 37 °C and then used at a 1:100 dilution to inoculate an expression culture in LB medium. Protein expression was induced at OD_{600}=0.8-1 by adding 0.02% arabinose and carried out at 20°C shaking (180 rpm) overnight. Cells were harvested by centrifugation in a Beckmann centrifuge, rotor JLA 8.100, at 4500 rpm for 20 min at 4°C. Cell pellets were transferred into 50 ml Falcon tubes, washed by resuspending them with PBS and then spun down at 5000 rpm for 15 min. Pellets were then either stored at -20°C or immediately used for purification.

The purification procedure was adapted from [106]. Pellets were resuspended in one pellet volume of lysis buffer and sieved to remove clumps. Cells were lysed by sonication 3x30 seconds, on ice. The sample was mixed between sonication cycles. The lysate was spun down in a Beckmann centrifuge, rotor JA 25.50 at 10000 rpm for 10 min. The cleared supernatant was then loaded on a step gradient 10-60% sucrose obtained by mixing lysis and sucrose buffer in appropriate ratios and by carefully layering the different percentage buffers into ultracentrifugation tubes. The lysate was then subjected to ultra–centrifugation at 28000 rpm for 3.5 hours in a SW28 rotor (Beckmann Coulter Inc.). Fractions of 2 ml were collected by gravity, by puncturing the ultracentrifugation tube from the bottom. Fractions containing the capsids were pooled and concentrated using the KrosFlo with a 500 kDa cutoff membrane. The final sample was then labelled with dye/NLS peptide according to the procedure outlined in section 2.1.5. For long–term storage at -80°C , the sample was flash–frozen in liquid nitrogen after adding 30% sucrose.

2.1.4 Specific methods used for the purification of capsids

Tangential flow filtration

Tangential flow filtration (TFF) is an alternative filtration method to typical dead–end filtration, which allows gentle buffer exchange or concentration of sensitive sample such as capsid–like particles. The main difference of this method is that the sample is under continuous flow and most of the feed flow travels tangentially across the surface of the filter, rather than into the filter. This approach has the advantage of much less caking at the membrane, which makes it ideal for samples that would easily plug a filter in traditional dead–end filtration.

A scheme of the TFF principle is displayed in Figure 2.1: briefly, the sample is flowed into hollow fibers and particles smaller than the membrane cutoff size flow out into the permeate. The sample which is retained (retentate), flows back into the membrane and the process continues in this way until completion of the buffer exchange. For capsid purification, the TFF system KR2i TFF System from Spectrum Labs was employed with modified Polyethersulfone (mPES) hollow fiber filters of different cutoff size to concentrate and buffer exchange the samples. This technique enabled a much higher sample recovery and sample integrity compared to dead–end filtration with centrifugal filters.

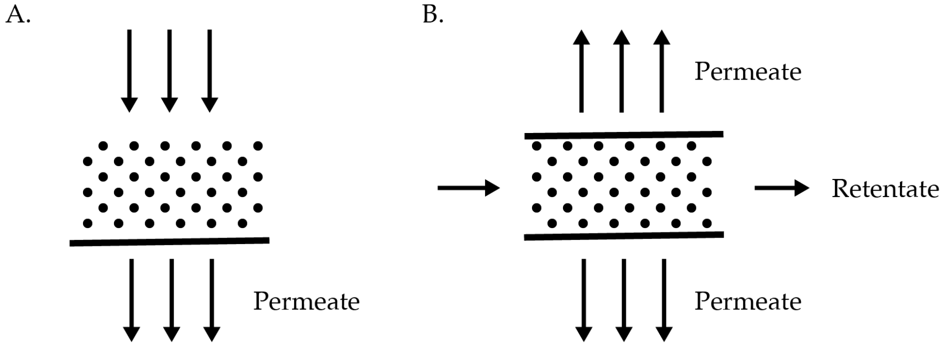

FIGURE 2.1: Principle of tangential flow filtration. In traditional dead–end filtration (A) the solution containing the protein of interest is forced directly through a membrane structure, which rapidly forms a "cake" layer, blocking the filter. In tangential flow filtration (B), the solution continuously flows parallel to the hollow fiber and particles smaller than the membrane cutoff can permeate out of the fiber. This substantially reduces caking, which can be further controlled by adjusting the flow rate and transmembrane pressure.

Negative staining EM

Successful capsid assembly was confirmed by imaging the samples with an electron microscope using negative staining. Carbon coated 300 meshes Quantifoil Cu grids were glow-discharged for 10 s in a vacuum chamber. Then, a 3 μL drop of sample was adsorbed on a grid for 2 min, blotted with Whatman's filter paper and washed 3 times with sample buffer, then 3 times with a solution of 2% uranyl acetate. Once the grids were dry, the sample was imaged using a Morgagni 268 microscope (FEI) located in the Electron Microscopy Core Facility (EMCF) at EMBL.

Dynamic light scattering

Dynamic light scattering (DLS) is a technique that allows the determination of the size distribution profile of particles in solution by measuring fluctuations of scattered light intensity over time. DLS measurements to quantify the hydrodynamic radius of capsids and test for sample aggregation / disassembly were performed on a Zetasizer Nano (Malvern). Samples were diluted to a final concentration of 0.5 μM in filtered transport buffer and spun down for 10 min at 10.000 rpm prior to each measurement. For each sample, at least 10 measurements were acquired, using a quartz cuvette. Count rates per second were typically higher than $\approx$ 200 kcps, and the polydispersity index was below 0.2, indicating a monodisperse solution. Data were analysed using the Malvern software, using the Multiple Narrow Bands fitting algorithm and Refractive Index and Absorption settings for proteins.

Fluorescence correlation spectroscopy

Fluorescence correlation spectroscopy (FCS) is a powerful method to characterize the diffusion properties of fluorescently labelled molecules [107, 108]. FCS is based on monitoring the fluctuations in fluorescence signal as labelled molecules in solution travel into and out of the observation volume (typically in the femtoliter range). Analysis of the intensity fluctuations can inform on the number of particles present in solution as well as their diffusion times. The autocorrelation function $G(\tau)$ is given by:

$$G(\tau) = \frac{\langle I(t)I(t+\tau)\rangle}{\langle I^2\rangle} \tag{2.1}$$

Where $I(t)$ is the fluorescence intensity at a time t and $I(t+\tau)$ the intensity at time $t+\tau$. The autocorrelation function is computed for different lag times τ and then fitted to extract the parameters of interest. The geometry of the excitation and detection volume can be approximated by a three dimensional Gaussian function, and thus $G(\tau)$ can be described analytically by:

$$G(\tau) = \frac{1}{N}\left(1+\frac{\tau}{\tau_D}\right)^{-1}\left(1+k^2\frac{\tau}{\tau_D}\right)^{-0.5} \tag{2.2}$$

Where N is the number of observed molecules, τ_D is the diffusion time of the molecules through the confocal volume and k is the structural parameter, which describes the shape of the detection volume.

FCS experiments were carried out on a custom–built multiparameter spectrometer confocal setup, equipped with a 60x water objective (NA = 1.27). The capsid samples were diluted to achieve a dye concentration of 20 nM in filtered transport buffer and they were spun down for 10 min at 10.000 rpm prior to the start of the experiment. For each sample, at least 10 FCS curves of 30 s each were acquired. A calibration FCS measurement with a free dye solution was carried out every 2–3 samples to measure the structural parameter and confirm the stability of the setup. Data analysis was performed with the SymphoTime software. Autocorrelation curves were computed for lag times between 0.0001 and 1000 ms and fitted with a diffusion model (see Equation 2.2).

2.1.5 Maleimide labelling of capsids

After purification, capsids were labelled via maleimide chemistry to couple a fluorescent dye and NLS peptide to the exposed cysteines. The dye / peptide were stored at -80 °C in 50 nmol aliquotes and freshly resuspended in anhydrous DMSO. The capsids were incubated with different molar excesses of dye and NLS peptide for 1-2 hours at room temperature. The reaction was then quenched by adding 10 mM DTT and the protein was spun down at 10000 rpm for 10 minutes to remove any precipitation. The excess dye was removed by loading the capsid sample on a

HiPrep Sephacryl 16/60 size exclusion column (GE Healthcare), using the appropriate SEC buffer. Relevant fractions containing the labelled capsids were then pooled and concentrated using the KrosFlo. The ratio of capsid monomers tagged with NLS peptide was quantified by the gel band ratio on a SDS PAGE gel with Coomassie staining, as the labelled monomers migrate differently due to their increased molecular weight.

2.2 Transport assays in permeabilized cells

2.2.1 Purification of NTRs

Impβ

Composition of buffers used for the purification:

- Lysis buffer: 50 mM Tris pH 7.0, 650 mM NaCl, 5 mM $MgCl_2$, 5 mM imidazole, 1 mM PMSF, 0.2 mM TCEP
- Wash buffer 1: 50 mM Tris pH 7.0, 1.5 M NaCl, 5 mM $MgCl_2$, 10 mM imidazole, 1 mM PMSF, 0.2 mM TCEP
- Wash buffer 2: 50 mM Tris pH 7.0, 650 mM NaCl, 5 mM $MgCl_2$, 15 mM imidazole, 1 mM PMSF, 0.2 mM TCEP
- Elution buffer: 50 mM Tris pH 7.0, 650 mM NaCl, 5 mM $MgCl_2$, 400 mM imidazole, 1 mM PMSF, 0.2 mM TCEP
- SEC buffer: 50 mM Tris pH 7.0, 650 mM NaCl, 5 mM $MgCl_2$, 0.2 mM TCEP

A colony of *E. coli* BL21 (DE3) AI cells containing the pTXB3-12His-Importin beta WT plasmid was inoculated in LB medium containing 50 μg/ml ampicillin. The culture was grown overnight shaking at 37°C and then used at a 1:100 dilution to inoculate an expression culture in LB medium. Cells were incubated at 37°C while shaking. Once the culture had reached OD_{600}=0.6, protein expression was induced by adding 1 mM IPTG and 0.02% arabinose. The protein was expressed at 30°C shaking (180 rpm) for 5-6 hours. Cells were then harvested by centrifugation in a Beckmann centrifuge, rotor JLA 8.100, at 4500 rpm for 20 min at 4°C.

For purification, pellets were resuspended in two pellet volumes of lysis buffer and lysed by sonication (0.5 s on, 2 s off, for 2 min). The lysate was spun down in a Beckmann centrifuge, rotor JA 25.50 at 15000 rpm for 1 h at 4°C. The clear lysate was then incubated for 1 h on Ni–beads (1 mL for each L of expression) at 4°C under gentle rotation. Beads were then poured into a PP column, washed two times with lysis buffer (with 2 column volumes), one time with wash buffer 1 (with 2 column volumes) and one time with wash buffer 2 (1.4 times the column volume). The sample was then eluted with one column volume of elution buffer. The elution was incubated for 6 h at room temperature with 100 mM β–mercaptoethanol and later dialyzed against lysis buffer without imidazole. The sample was then subjected to a second round of Ni–beads purification: it was incubated with 0.1 mL Ni–beads/l of expression for 2 h at 4°C and passed through a PP column. The flow through was collected and then concentrated to 500 μL in a centrifugal concentrator filter (Amicon Ultra, Millipore) with 30 kDa cutoff. Finally the sample was subjected to gel–filtration chromatography on a Superdex 200 (S200) column. For long–term storage at -80°C, the protein was flash frozen in liquid nitrogen after adding 25% glycerol.

Impα

Expression and purification of impα (plasmid pBAD-Importα1-FL-InteinCBD-12His) was identical to impβ.

NTF2

Expression of NTF2 (plasmid pTXB3-NTF2-intein-6His) in *E. coli* BL21 (DE3) star cells and purification was identical to impβ, but protein expression was carried out overnight at 34°C. For the size–exclusion step, a Superdex 75 column was used.

Ran

Composition of buffers used for the purification:

- Lysis buffer: 30 mM Tris pH 7.4, 0.2 M NaCl, 5 mM $MgCl_2$, 5 mM imidazole, 1 mM PMSF, 0.2 mM TCEP
- Wash buffer 1: 30 mM Tris pH 7.4, 0.2 M NaCl, 5 mM $MgCl_2$, 10 mM imidazole, 1 mM PMSF, 0.2 mM TCEP
- Wash buffer 2: 30 mM Tris pH 7.4, 0.2 M NaCl, 5 mM $MgCl_2$, 20 mM imidazole, 1 mM PMSF, 0.2 mM TCEP
- Elution buffer: 30 mM Tris pH 7.4, 0.2 M NaCl, 5 mM $MgCl_2$, 400 mM imidazole, 1 mM PMSF, 0.2 mM TCEP
- SEC buffer: 30 mM Tris pH 7.4, 0.2 M NaCl, 5 mM $MgCl_2$, 0.2 mM TCEP

A colony of *E. coli* BL21 (DE3) AI cells containing the pTXB3-Ran Human FL-Intein-CBD-12His plasmid was inoculated in LB medium containing 50 μg/ml ampicillin. The culture was grown overnight shaking at 37°C and then used at a 1:100 dilution to inoculate an expression culture in LB medium. Cells were incubated at 37°C while shaking. Once the culture had reached OD_{600}=0.6-0.8, protein expression was induced by adding 1 mM IPTG and 0.02% arabinose. The protein was expressed overnight at 18°C shaking (180 rpm). Cells were then harvested by centrifugation in a Beckmann centrifuge, rotor JLA 8.100, at 4500 rpm for 20 min at 4°C.

For purification, pellets were resuspended in one pellet volume of lysis buffer and lysed by sonication 3x30 seconds or with a microfluidizer for at least 3 rounds at 4°C. The lysate was spun down in a Beckmann centrifuge, rotor JA 25.50 at 18000 rpm for 1 h at 4°C. The clear lysate was then incubated for 2 h on Ni–beads (1 mL for each L of expression) at 4°C under gentle rotation. Beads were then poured into a PP column, and the FT was collected. Ni–beads were washed with at least 10 bead volumes of lysis buffer, and then with the same volume of wash buffers 1 and 2. The protein was eluted with 6 bead volumes of elution buffer. The elution was incubated overnight with 100 mM β–mercaptoethanol at room temperature under gentle rotation. On the following day, the protein was dialyzed against lysis buffer without imidazole and PMSF. The sample was then subjected to a second round of Ni–beads purification: it was incubated with 0.2 mL Ni–beads per liter of expression for 2 h at 4°C and passed through a PP column. The flow through was collected and then concentrated in a centrifugal concentrator filter (Amicon Ultra, Millipore) with 10kDa cutoff. Finally the sample was subjected to gel–filtration chromatography using a S200 column. For long–term storage at -80°C, the protein was flash frozen in liquid nitrogen after adding 25% glycerol.

Loading of Ran with GDP

For loading of Ran with GDP, Ran protein was incubated with a 50–fold molar excess of GDP in presence of 6 mM EDTA for 40 min on ice. The reaction was stopped by adding 25 mM $MgCl_2$, the sample was then purified over a S200 size–exclusion column to remove the excess of unreacted GDP. Success of the loading reaction could be confirmed by incubating the protein at 95°C to release the bound nucleotide and loading the supernatant after centrifugation on a POROS 20 HQ column (see Figure 2.2). A gradient of 0-1 M NaCl allowed the elution of nucleotides and the identification of GDP released from the Ran sample.

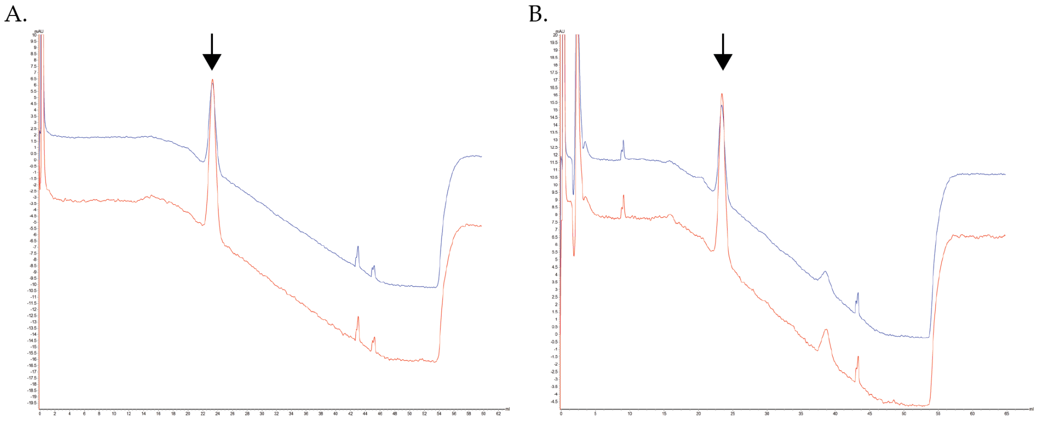

FIGURE 2.2: Chromatograms from a POROS 20 HQ column injected with a GDP reference solution (A) or with RanGDP after nucleotide release (B). The blue curve corresponds to absorbance at λ= 280 nm, the red one to λ= 254 nm. The peaks corresponding to GDP are indicated by a black arrow.

2.2.2 Purification of reference cargoes

MBP-GFP-IBB

A small cargo used in nuclear import assays was an MBP-GFP-IBB fusion. Expression and purification of this protein was analogous to to impβ.

Traptavidin-GFP-NLS

A traptavidin-GFP fusion with and without an NLS sequence was also used as a standard cargo to characterize the nuclear import assays.

Composition of buffers used for the purification:

- Lysis buffer: 50 mM Tris pH 7.5, 150 mM NaCl, 0.2% Triton X-100, 10% glycerol, 5 mM imidazole, 0.2 mM TCEP, 1 mM PMSF
- Wash buffer 1: 50 mM Tris pH 7.5, 150 mM NaCl, 0.2% Triton X-100, 10% glycerol, 10 mM imidazole, 0.2 mM TCEP, 1 mM PMSF
- Wash buffer 2: 50 mM Tris pH 7.5, 150 mM NaCl, 0.2% Triton X-100, 10% glycerol, 25 mM imidazole, 0.2 mM TCEP, 1 mM PMSF
- Wash buffer 3: 50 mM Tris pH 7.5, 150 mM NaCl, 0.2% Triton X-100, 10% glycerol, 50 mM imidazole, 0.2 mM TCEP, 1 mM PMSF
- Elution buffer: 50 mM Tris pH 7.5, 150 mM NaCl, 0.2% Triton X-100, 10% glycerol, 500 mM imidazole, 0.2 mM TCEP, 1 mM PMSF
- SEC buffer: 50 mM Tris pH 7.5, 150 mM NaCl, 10% glycerol, 0.2 mM TCEP

A colony of *E. coli* BL21 (DE3) AI cells containing the pBAD-NLS-Trap-GFP-6His or pBAD-Trap-GFP-Cys-6His plasmid was inoculated in LB medium containing 50 μg/ml ampicillin. The culture was grown overnight shaking at 37°C and then used at a 1:100 dilution to inoculate an expression culture in LB medium. Cells were incubated at 37°C while shaking. Once the culture had reached OD_{600}=0.7, protein expression was induced by adding 0.02% arabinose. The protein was expressed overnight at 20°C shaking (180 rpm). Cells were then harvested by centrifugation in a Beckmann centrifuge, rotor JLA 8.100, at 4500 rpm for 20 min at 4°C.

For purification, pellets were resuspended in one pellet volume of lysis buffer and lysed by sonication 3x30 seconds or with a microfluidizer for at least 3 rounds. The lysate was spun down in a Beckmann centrifuge, rotor JA 25.50 at 15000 rpm for 1 h at 4°C. The clear lysate was then incubated for 2 h on Ni–beads (1 mL for each L of expression) at 4°C under gentle rotation. Beads were then poured into a PP column, and the FT was collected. Ni–beads were washed with 10 bead volumes of wash buffer 1, and then with 4 bead volumes of wash buffers 2 and 3. The protein was eluted with 2-3 bead volumes of elution buffer. The elution was concentrated in a centrifugal concentrator filter and finally purified via a S200 column. For long–term storage at -80°C, the protein was flash frozen in liquid nitrogen after adding 25% glycerol.

2.2.3 Preparation of cells for transport assay

Cell culture

HeLa Kyoto cells were cultured at 37°C in 5% CO_2 atmosphere in Dulbecco's modified Eagle's medium with 1 g/ml glucose supplemented with 1% penicillin–streptomycin, 1% L-Glutamine and 10% FBS. The cells were passaged every 2-3 days up to maximum of 15-18 passages. For nuclear transport assays, the cells were seeded 1 or 2 days before the experiment at low density (7000-10000 cells per well) in a 8-well Lab-Tek II chambered coverglass (Thermo Scientific Nunc, 155383).

Permeabilized cell assay

Cells for transport assays were stained with 100 nM MitoTracker green (Invitrogen, M7514) in growth medium for 30 min at 37°C in 5% CO_2. For nuclear staining, cells were rinsed once with PBS and incubated for 10 min at room temperature with 20 nM Hoechst 33342 (Sigma, B2261). Cells were then washed once with transport buffer (1XTB: 20 mM Hepes, 110 mM KOAc, 5 mM NaOAc, 2 mM MgOAc, 1 mM EGTA, pH 7.3) and permeabilized by incubation for 10 min at room temperature with digitonin (40 μg/mL). Cells were then washed 3 times with 1XTB supplied with 5 mg/ml PEG 6000 to avoid osmotic shock. The transport mix was then added freshly to the cells to start the experiment.

The transport mix consists of the purified transporters and recycling factors with the addition of a source of energy, in 1XTB with PEG with 1 mM DTT: all components are listed in Table 2.1 below.

impα	1 μM
impβ	1 μM
cargo	0.5 μM
RanGDP	4 μM
NTF2	2 μM
GTP	2 mM

TABLE 2.1: Composition of transport mix.

In order to allow the import complex to form, the cargo was always pre–incubated with impβ and impα on ice for at least 10–15 minutes. Following pre–incubation, the rest of the transport mix was added and the solution was spun down for 10 min at 10.000 rpm to remove any aggregates. When indicated, a energy regenerating system was included, consisting of 0.1 mM ATP, 4 mM creatine phosphate (Roche, CRPHO-RO) and 20 U/ml creatine phosphokinase (Sigma, C3755). In single–particle experiments the cargo concentration was reduced as indicated. As a positive control for nuclear transport functionality, a GFP-traptavidin-NLS cargo was used (see Figure 2.3 for typical images). For negative controls, cargoes without a NLS sequence were used or cells were incubated with transport mix lacking impβ, RanGDP and GTP. Alternatively, cells were incubated for 15 min with the lectin Wheat Germ Agglutinin (WGA, 50 μM/mL) which inhibits nuclear transport. Envelope integrity throughout the experiments could be confirmed by incubating the cells with FITC–labelled 70 kDa Dextran (Sigma 53471), which should not enter the cell nucleus. Imaging was performed on a Zeiss LSM 880 or Olympus FV3000 confocal microscope from the Advanced Light Microscopy Facility at EMBL using a 63x oil objective (NA = 1.4).

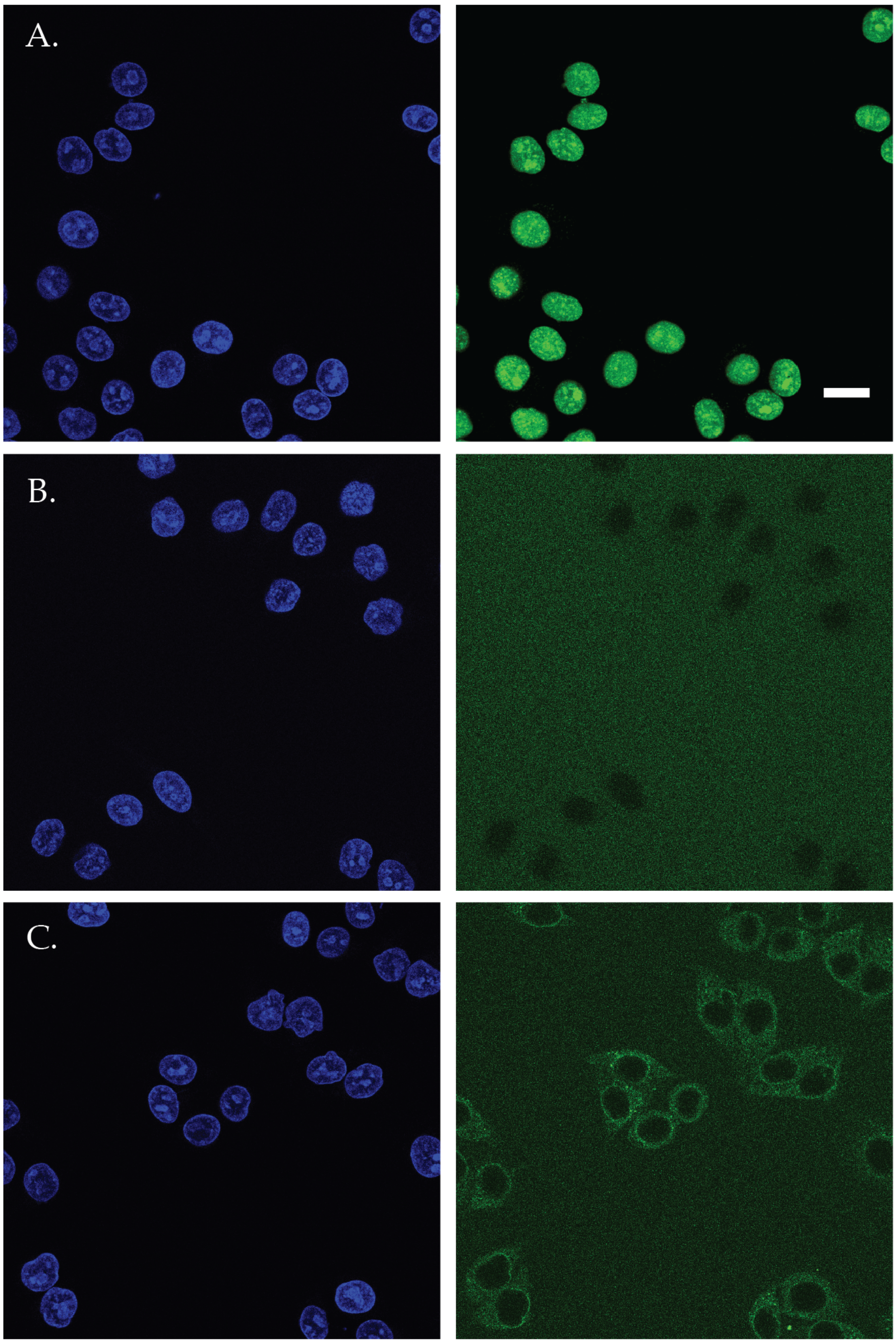

FIGURE 2.3: Nuclear import assay of traptavidin–GFP in permeabilized cells. The Hoechst channel is shown on the left as reference for the nuclear positions and the GFP channel is on the right. (A) Positive control of traptavidin–GFP–NLS. (B) Negative control of traptavidin–GFP lacking a NLS. (C) Negative control of traptavidin–GFP–NLS in transport mix without impβ, RanGDP and GTP. All images have been taken at a confocal microscope (Olympus FV3000) after 30 min of incubation time (average of 5 frames to improve signal–to–noise). The scale bar corresponds to 20 μm.

2.2.4 Preparation of cells for immunostaining

For anti–Nup immunostaining after completion of the transport experiment, the cells were fixed with 2% PFA for 10 minutes at room temperature. The cells were then rinsed once with PBS and permeabilized with 0.5% Triton-x 100 in PBS for 15 minutes at room temperature. After fixation, cells were rinsed twice and blocked with 3% BSA in PBS for 1.5 h at room temperature. The blocking solution was then removed and the cells were incubated overnight at 4°C with the primary antibody. The next morning, cells were rinsed and incubated with the secondary antibody for 1 h at room temperature. After rinsing with PBS the cells were then taken to the microscope for imaging. The primary and secondary antibodies used for different target Nups are listed in the Materials section.

2.2.5 Automated confocal microscopy and analysis

Timelapse confocal imaging of nuclear import was performed on a Olympus FLUOVIEW FV3000 scanning confocal microscope from the Advanced Light Microscopy Facility at EMBL, using a 20x air objective (NA = 0.75). An automated multi–position acquisition was carried out, where 12 different regions (typically containing 10 cells each) were imaged in two different wells. Three channels (Hoechst, Mitotracker and cargo) were recorded at each time step. Images were acquired every 2 minutes for 60-90 minutes, using continuous autofocusing with Z–drift compensation to ensure imaging stability.

Results for the timelapse import experiments were analyzed with a custom–written Fiji script (see pipeline of the analysis in Figure 2.4). Briefly, the Hoechst and Mitotracker channels were used to generate reference masks for the nucleus, nuclear envelope and cytoplasm. The masks were then used to extract the average intensity of cargo signal in the different areas of interest. Final data analysis and plotting was performed in IgorPro (Wavemetrics).

2.2.6 FRAP experiments

FRAP (Fluorescence Recovery After Photobleaching) is a method to interrogate the dynamics of fluorescent molecules in cells. After irreversibly bleaching a pool of molecules with a high intensity laser, the recovery of fluorescent signal arising from the movement of unbleached molecules in the region of interest is monitored. This allows to deduce information regarding the motility of the fluorescent species under study. FRAP experiments were performed on a Olympus FLUOVIEW FV3000 scanning confocal microscope from the Advanced Light Microscopy Facility at EMBL, using a 40x dry objective (NA = 0.95). A small region of interest was selected for imaging (typically containing one or two nuclei), and a custom region was drawn

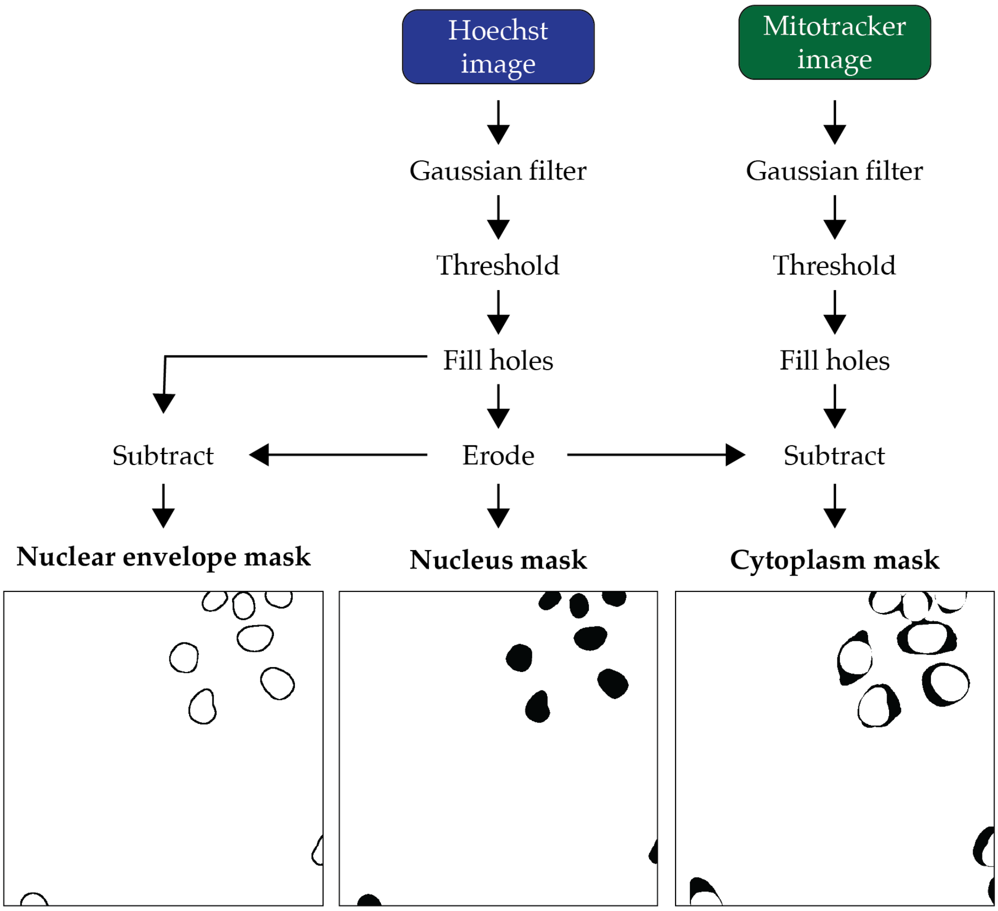

FIGURE 2.4: Pipeline analysis of ensemble nuclear import experiment. Hoechst and Mitotracker images were first blurred with a Gaussian filter for better thresholding results, then thresholded to obtain a binary "mask" image. The masks were then optimized via binary operations (fill holes, erosion) and finally applied to the cargo channel to measure intensity in the regions of interest.

to specify the area to be bleached (whole nucleus or a portion of nuclear envelope). The area of interest was then bleached to approximately half of its intensity by using maximum power of the laser. Recovery of the fluorescence was monitored by acquiring images of the region every 10 s for 15 min. Continuous autofocusing was employed to make sure that the z position was maintained throughout the whole experiment.

2.3 Experimental TIRF/HILO setup

In this section, I will describe the custom–built microscopy setup I used for single–particle tracking and super–resolution experiments.

The microscopy setup was designed to enable TIRF and HILO illumination of the sample, in addition to standard epi–illumination. Both of these methods allow better optical sectioning and higher signal–to–noise ratios by reducing background fluorescence of out–of–focus particles, which is critical for single–particle detection in cells. The principle behind the two illumination schemes is illustrated in Figure 2.5. TIRF exploits the phenomenon of total internal reflection: a light beam reaching an interface between mediums with two different refractive indexes (n) will be partially reflected and refracted, following Snell's law:

$$n_1(sin\theta_1) = n_2(sin\theta_2) \tag{2.3}$$

For $n_2 > n_1$ and incident angles higher than the critical angle ($\theta_c = sin^{-1}(n_2/n_1)$), the light beam is completely reflected back into the first medium. In these conditions, an evanescent field is produced at the interface which is characterized by an exponentially decaying intensity. The fields penetrates approximately 100 nm into the sample and can be used as an excitation source for samples localized close to the coverslip (for example the plasma membrane). HILO (highly inclined and laminated optical sheet) illumination is based on a similar principle as TIRF: it has been shown that at angles slightly below the critical angle an inclined light sheet is generated which allows to selective excite a thin layer of the sample [109]. The main advantage of this illumination method is that it is not limited to samples close to coverslip surface.

The TIRF/HILO setup is schematically represented in Figure 2.6 and details of the optical components are listed in the Materials section (2.5). The microscope is equipped with four lasers, to allow flexibility in the choice of fluorophores: Omicron 405 nm, Omicron 488 nm, Sapphire 568 nm and Omicron 660 nm. Three lasers are equipped with clean–up filters: 475/23 for the 488, 572/15 for the 568 and 661/11 for the 660. In the excitation path, the lasers are expanded with 10x beam expanders (Qioptiq) for the 660, 594 and 488 lasers and a 7x beam expander (Qioptiq) for the 405 laser. The lasers are then combined using dichroic mirrors 458 for the 405 nm laser, 495 for the 488 laser, 605 for the 568 nm laser and a mirror for the 660 nm laser. The lasers polarization is then set to circular using a quarterwave plate (G362021491, Qioptiq). In order to switch between epi–illumination, TIRF and HILO modes, a mirror mounted on a linear stage (PI, M505) is used to shift the beam respect to the objective (100X high NA objective UAPON 100X TIRF, NA 1.49, Olympus GmbH). The beam is then focused through a 300 mm focal distance lens and reflected by a quad band beam splitter into the objective. The emission path consists of a system

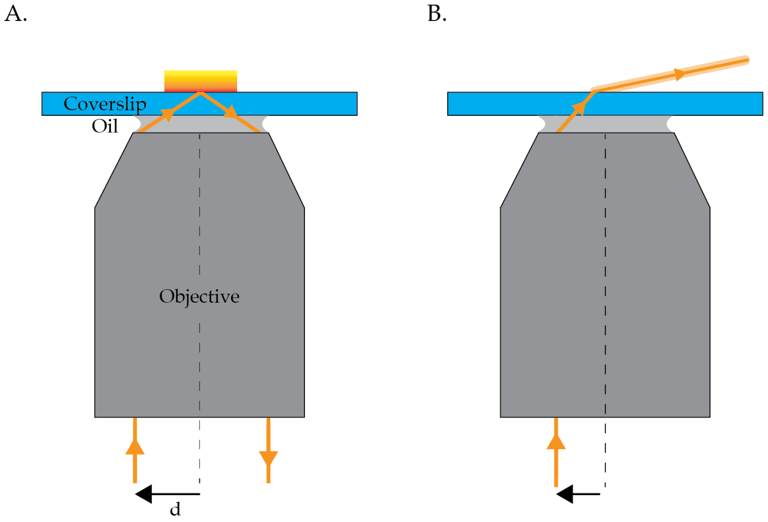

FIGURE 2.5: Principle of TIRF (A) and HILO (B) illumination schemes. The main difference is the incidence distance d of the laser in the back focal plane of the objective, which results in different incidence angles.

of three consecutive lenses (two 180 mm and one 120 mm focal length), optimized to minimize aberrations. Notch filters (568/647 and 658) are used in the emission path to filter out any residual excitation light. Imaging is performed with two EMCCD cameras (Andor Technology, DU-897 and DU-897D, iXon X3 EMCCD). For dual–color imaging, the emission is split by a dichroic mirror and filtered by emission filters suitable for the fluorophore of choice (see Table 2.2 for the pairs employed in this thesis).

Fluorophores	**Dichroic mirror**	**Emission filter 1**	**Emission filter 2**
A488, A647	Chroma F43-T08 643	525/50 Chroma	700/100 Chroma
A647, CF680	AHF 690	700/100 Chroma	700/100 Chroma

TABLE 2.2: Dichroic mirrors and filter settings used for different fluorophore pairs.

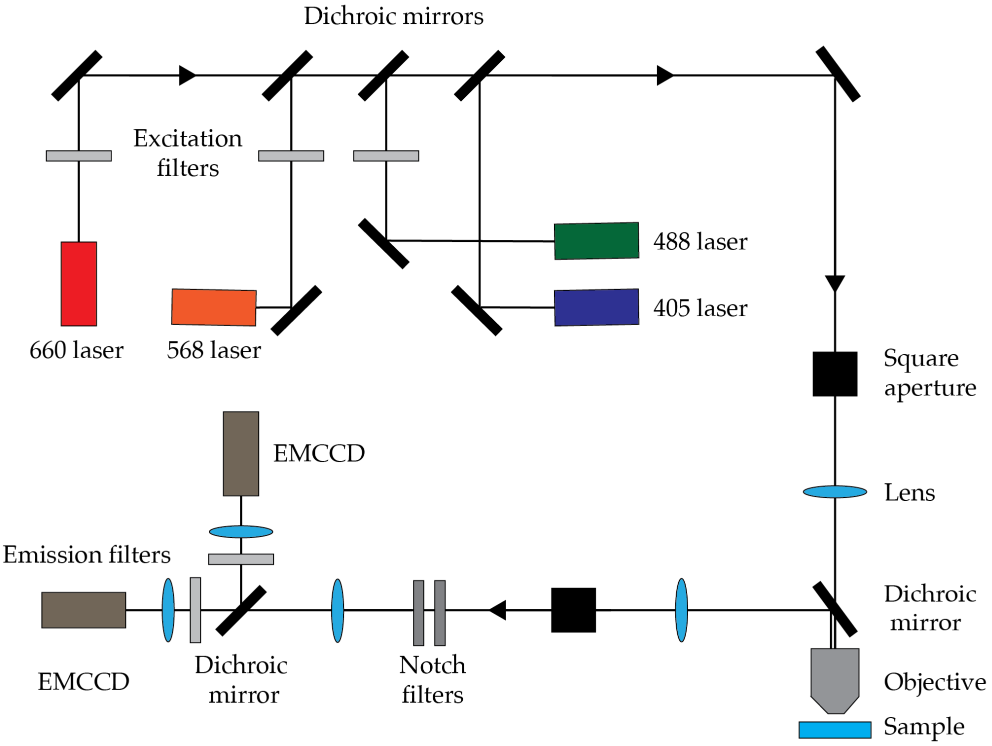

FIGURE 2.6: Beampath of the self–built TIRF/HILO setup used for super–resolution imaging and single–particle tracking. On the top, lasers are combined to a single collimated beam in the excitation path, which then travels down to the 100x objective. On the bottom of the scheme, the light emitted from the sample is filtered and collected on two EMCCD cameras.

2.4 Super–resolution imaging and single–particle tracking

Localization–based super–resolution imaging and single–particle tracking are both based on the same principle: a diffraction–limited spot is fitted with a mathematical function to recover its position at a higher resolution. The key requisite is that the emitters are sparse enough to be individually resolved: in single–particle tracking this can be achieved by decreasing the concentration of the molecule of interest. In super–resolution imaging, a densely labelled sample presents many fluorophores which can overlap: it is thus necessary to "switch on" only few of them at a time and do many repeated cycles of switching and imaging. The switching on/off of fluorophores can be achieved in different ways: in direct stochastic optical reconstruction microscopy dSTORM, the photo-physical properties of small organic fluorophores are exploited. These dyes spontaneously and reversibly switch between a fluorescence emitting state and a long lived dark state, and the switching behaviour can be tuned by laser power and buffer composition [110].

For both super–resolution imaging and single–particle tracking, the microscopy setup was aligned prior to each experiment, and correct alignment of the excitation and emission beam was confirmed using a fluorescent solution of mixed dyes and fluorescent beads (TetraSpeck, Thermofisher T7280). Images of the fluorescent beads were acquired in the two channels as a reference to build a correction map and align the two images at sub–pixel precision. The correction map was constructed by fitting the shifts of the emitters in the x and y directions with a global polynomial function.

2.4.1 Dual–color super–resolution imaging

For dual–color super–resolution imaging, a spectral demixing approach was adopted [111]: the spectrally similar dyes CF680 and AF647 were excited by a single 660 laser and imaged using the dichroic/filters specified in Table 2.2. Cross-talk between the two channels resulted in localization of the dyes in both cameras, with a ratiometric distribution.

The composition of the GLOX-MEA blinking buffer was: 50 mM Tris (pH 8.0), 10 mM sodium chloride, 0.5 mg/ml glucose oxidase (Sigma, G0543), 40 μg/ml catalase (Sigma, C3155), 10% glucose (Sigma, D9559) and 10 mM β-Mercaptoethylamine (MEA) (Sigma, M9768), stored in aliquots of 100 mM in PBS and adjusted to pH 7.4 with hydrochloric acid. For imaging, fluorophores were first brought to the dark state by illuminating the cells with maximum power of 660 nm laser ($\approx$ 1 kW/cm2) for approximately 10 seconds. Once spontaneous blinking was initiated, the laser power was decreased to 0.3-0.5 kW/cm^2 and 20.000-30.000 frames were acquired with a 30 ms exposure time. In case of a decreased blinking after some time, back–pumping was performed by switching on the 405 nm laser and gradually increasing its power to maintain the blinking events constant in time.

Data analysis and image reconstruction were performed in IgorPro (see Figure 2.7 for a scheme of the analysis pipeline). First, fluorophores were localized in the two channels using the Localizer package [112] by fitting with a symmetrical 2D Gaussian function and aligned using the correction map obtained from the fluorescent beads images. Then, a self–written function was used to perform spectral demixing (assign the localization events to one of the two fluorophores). Briefly, emitters were matched between the two channels and the intensity ratio was computed:

$$r = \frac{I_l - I_s}{I_l + I_s} \tag{2.4}$$

Where I_l is the fluorophore's intensity in the long wavelength channel and I_s is the intensity in the short wavelength channel. The intensity ratio histogram (see Figure 2.8) displayed two clear peaks corresponding to the two dyes: thresholds were then defined to separate the two peaks and the emitters were thus assigned to one of the two channels. Finally, super–resolved images were reconstructed by convolving each set of localizations with a Gaussian function.

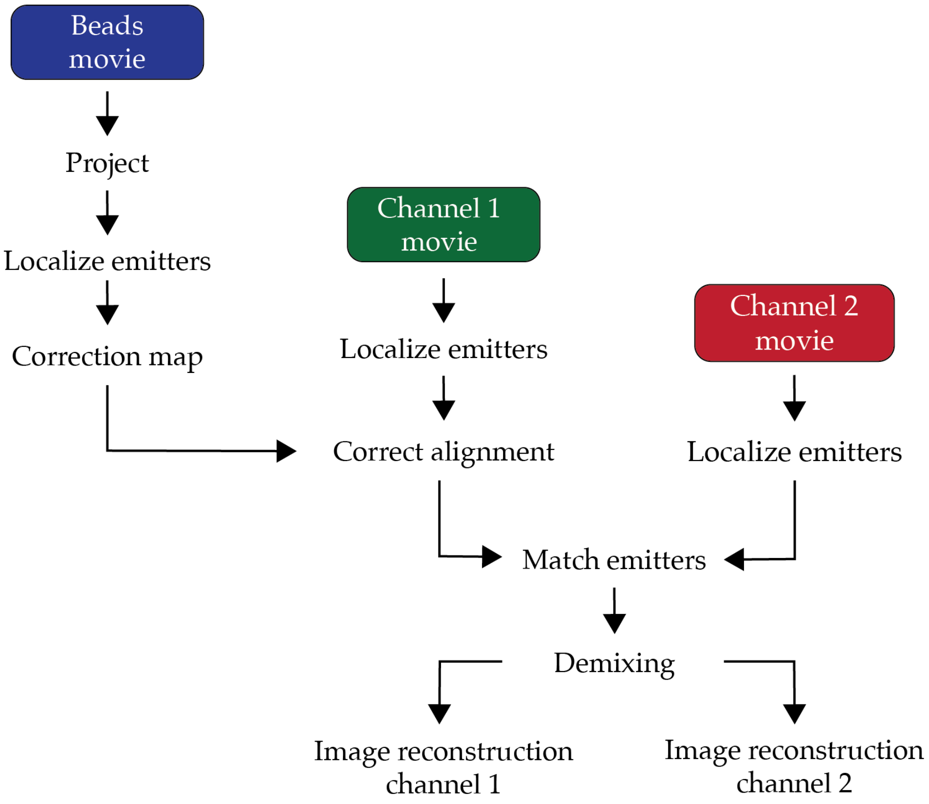

FIGURE 2.7: Pipeline of dual–color super–resolution analysis. First, a correction map is created from reference images of fluorescent beads to align the two channels. Emitters are then localized in both channels, aligned and matched. After demixing, two sets of localizations assigned to the two channels are obtained and used to reconstruct super–resolved images.

2.4.2 Single–particle tracking

For single–particle tracking, dichroic and filter settings for 488/647 dye pair were employed (see Table 2.2). After permeabilization, cells were pre–incubated for 10-15 min with with 1xTB+PEG containing 150 nM impβ labelled with A488 to stain the nuclear envelope. Then, the transport mix containing 2 nM labelled capsid sample was added to the cells and they were immediately taken to the microscope for imaging. For imaging, HILO illumination was employed in order to image the cross-section of the nuclear envelope, and the focus was adjusted according to the impβ channel. At the onset of the experiment, an ensemble reference image of the impβ channel was acquired with an exposure of 30 ms (typically 1.000-2.000 frames were recorded). Then, a single–particle tracking movie of $\approx$ 200.000 frames was acquired in the capsid channel with an exposure of 2 ms and kinetic cycle of 20 ms. At the end of the acquisition, another reference impβ movie was recorded in order to confirm that no substantial drift occurred in the time of the experiment.

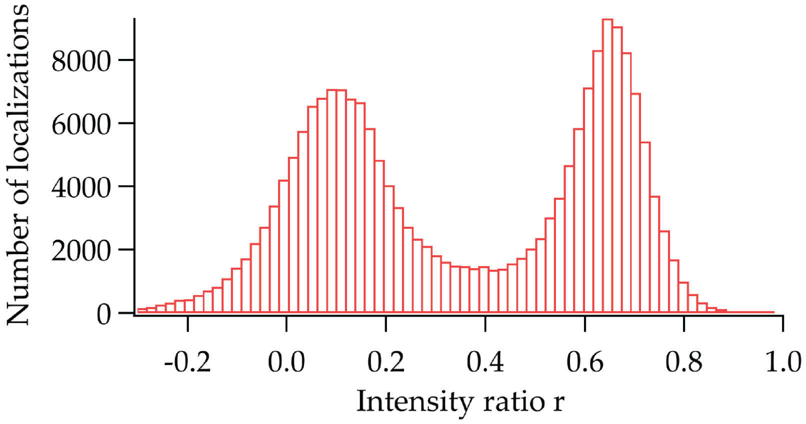

FIGURE 2.8: Histogram of the intensity ratio from a dual–color imaging experiment with spectral demixing: note the two distinct peaks corresponding to the two different fluorophores.

In order to achieve fast acquisition rates, a specialized "crop" mode was employed, available on the EMCCD iXon Ultra camera. In this mode, a small area of the chip (64 x 64 pixels) is used for imaging and the remaining part as a hardware buffer for the recorded signal (see Figure 2.9 for an illustration). In order to use this fast imaging mode it was necessary to mask the chip part that will not be used for imaging. An adjustable aperture was employed in the emission pathway to constrain the collection area to the desired image size and avoid light from falling on the remaining part of the chip, which could contaminate the image and degrade its quality.

Data analysis was performed in IgorPro (see Figure 2.10 for an outline of the analysis pipeline). In order to reconstruct tracks, cargo positions were first localized using the Localizer package, with thresholding based on the Maximum Likelihood Ratio and localization via 2D Gaussian fitting. The next step was the construction of the tracks by connecting successive localizations belonging to the same molecule. Due to the low concentration of the cargo, a nearest neighbor algorithm could be employed for this step: two localizations within a distance of less than 3 pixels and 2 frames were connected into a trajectory. Tracks shorter than three points were discarded.

After reconstructions, tracks were filtered to isolate the NPC crossing events. In order to localize the position of the nuclear envelope, the ensemble impβ image was used (after projection of the average intensity over 1.000 frames to improve image quality). NPC positions could be detected from the reference image with a similar localization procedure as used for tracking, and the positions were then fitted with a spline to obtain the nuclear envelope shape. Using this reference spline, tracks were filtered with a custom–written analysis routine based on their position relative to the nuclear envelope. The tracks were classified in 10 different categories, depending on their proximity to the nuclear envelope and whether they were crossing the reference curve (both from inside to outside and the other way around).

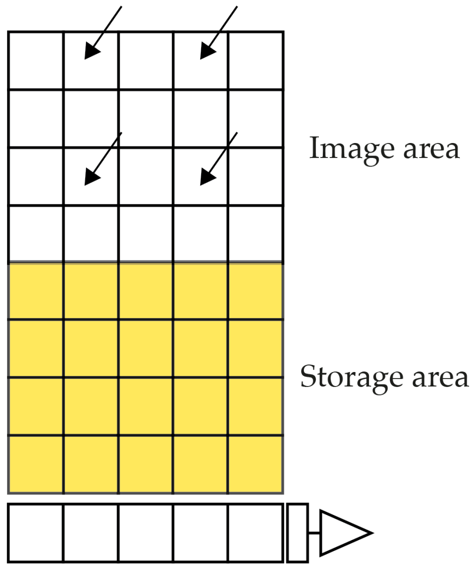

FIGURE 2.9: Principle of frame transfer in crop mode. During exposure, the image (photoelectric charge) is built up on the top part of the chip. The charge is then rapidly shifted into the storage area, and a second round of exposure can immediately start. From the storage area the image is finally read out by the shift register. The scheme is adapted from the Andor iXon Ultra EMCCD manual.

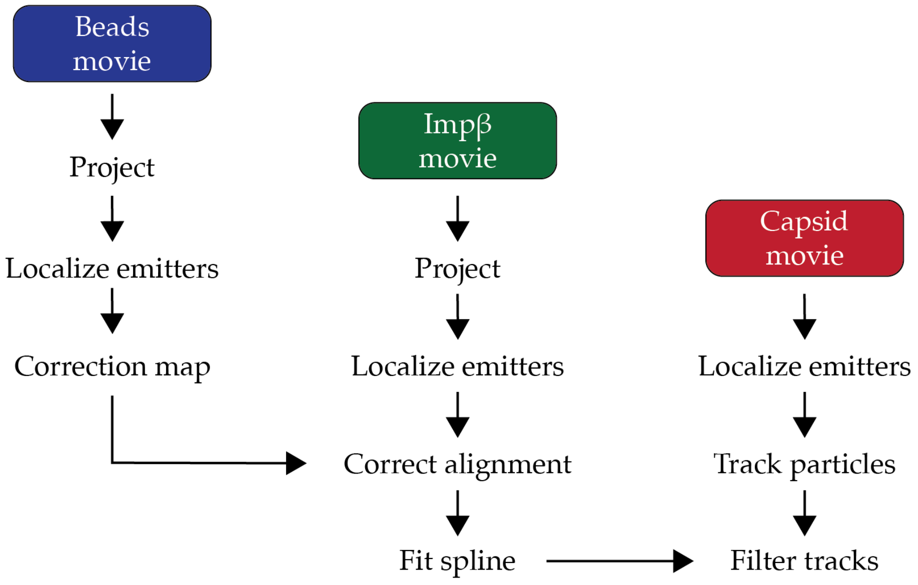

FIGURE 2.10: Analysis pipeline for single–particle tracking. First, a correction map is created from reference images of fluorescent beads to align the two channels. A reference *impβ* image is generated by projecting the movie acquired, and emitters are localized and corrected in order to obtain a spline representing the reference position of the nuclear envelope. In the capsid movie, emitters are localized and the positions are then used to reconstruct tracks of the particles. Finally, the tracks are filtered based on the envelope reference spline to obtain import events.

2.5 Materials used in this study

List of plasmids for bacterial expression:

Plasmid	Internal no.
pBAD_MS2_Coat_Protein–(1–393)	1791
pBAD_MS2_Coat_Protein–(1–393)_S37P	1923
pBAD-NLS-Trap-GFP-6His	1510
pBAD-Trap-GFP-Cys-6His	395
pET29b(+)_I53–47A.1–B.3_D43C	2196
pTXB3-12His-Importin beta WT	694
pBAD-Importα1-FL-InteinCBD-12His	720
pTXB3-NTF2-intein-6His	397
pTXB3-Ran Human FL-Intein-CBD-12His	448
pET28a2-SCSG-GB1-coreN-GFPβ1-10//NLS-GFPβ11-coreC149H6	534
pBAD-MCS-CoreN-cys-loop-CoreC-TEV-12His	1589
pET28a2-HBc14SH6_S81C	381

List of frequently used reagents:

Name	Company / cat.no.
CHAPS	AppliChem A1099.0010
DDT	Biomol 04010
Dulbecco's Eagle medium (low glucose)	Gibco 31885–023
EDTA	Ambion AM9261
FBS	Sigma F7524
GDP	Sigma G7127
GTP	Sigma G8877
His-Pur Ni-NTA Resin	ThermoScientific 88223
Imidazole	Sigma I5513
L-Glutamine	Sigma G7513
2-Mercaptoethanol	Aldrich M6250
Penicillin-streptomycin	Sigma F7524
PFA	Sigma 158127
Sucrose	Alfa Aesar 21938

List of antibodies:

Target	Type	Source	Label	Company / cat. no.
mAB414	primary	mouse	-	Biolegend 902901
Nup153	primary	rabbit	-	Novus NB100-93329
Nup358	primary	rabbit	-	Sigma HPA018437
ELYS	primary	rabbit	-	Sigma HPA031658
mouse	secondary	goat	A647	ThermoFisher A32728
rabbit	secondary	goat	A647	ThermoFisher A21246
mouse	secondary	goat	CF680	Biotium 20065-1
rabbit	secondary	goat	CF680	Biotium 20067-1

List of peptides:

Peptide	Label	Reactivity
GGGGKTGRLESTPPKKKRKVEDSAS	-	6-Maleimido-hexanoyl
GGGGKTGRLESTPPKKKRKVEDSASGGGGK	TAMRA	6-Maleimido-hexanoyl
GGGGKTGRLESTPPKKKRKVEDSASGGGGK	TAMRA	Malemidopropyl

All peptides were synthesized by PSL Peptide Specialty Laboratories GmbH.

List of synthetic dyes:

Name	Reactivity	Company / cat.no.
Alexa Fluor 647	Maleimide	Invitrogen A20347
CF680	Maleimide	Biotium 92029
Cy3B	Maleimide	GE Healthcare PA63131

List of TIRF/HILO microscope components:

Lasers:

Name	Wavelength	Company
Omicron LuxX 405-60	405 nm	Omicron
Omicron LuxX 488-200	488 nm	Omicron
Sapphire 568-100	568 nm	Coherent Inc.
Omicron LuxX 660	660 nm	Omicron

Filters:

Type	Name	Company / cat.no.
Clean–up	Brightline HC 475/23	Semrock FF01-475/23
Clean–up	Brightline HC 572/15	Semrock FF01-572/15
Clean–up	Brightline HC 661/11	Semrock FF01-661/11
Emission	525/50	Semrock FF01-525250-25
Emission	700/75	Chroma ET 700/75 M
Emission	700/100	AHF ET700/100
Notch	StopLine 568/647	Semrock NF01-568/647
Notch	Single notch 658	Semrock NF03-658E

Dichroic mirrors:

Name	Company / cat.no.
Single Band Dichroic Filter 458	Semrock FF458-Di02
Single Band Dichroic Filter 495	Semrock FF495-Di03
Single Band Dichroic Filter 605	Semrock FF605-Di02
Multi band dichroic	Chroma ZT405-488/568/660 RPC
Single Band Dichroic Filter 643	Chroma F43-T08 643 RDCXT
Single Band Dichroic Filter 690	AHF 690 DCXR

Lenses:

Focal length	Company / cat.no.
300 mm	Thorlabs AC508-300-A-ML
180 mm	Linos G322-246-000
120 mm	Linos G322-388-000

3 Results

Nuclear transport of large cargoes such as viral capsids is a highly relevant biological process, as it represents a key step in the life cycle of many viruses, however it is still poorly understood. The aim of my thesis is to quantitatively characterize nuclear import of large cargoes in cells, specifically looking at the effect of cargo size and exposed number of NLSs. In section 3.1, I will describe the "toolkit" of different large cargoes I developed based on capsid–like particles. In section 3.2, I will present the semi–automatic import kinetics experiments and analysis pipeline I implemented to quantitatively characterize bulk cargo import in relation to size and number of NLSs in cells and the results of these experiments. I will further discuss results of single–particle tracking experiments to investigate the steps of single cargo entry into the nucleus. Finally, in section 3.3 I will present results regarding a study of large cargo localization at the NPC employing super–resolution microscopy.

3.1 Development of a large cargo "toolkit" for nuclear transport studies

In order to gain a quantitative understanding of large cargo import through the NPC, a suitable model system to probe transport in response to different number of NLSs and to different size is necessary, however it has been so far lacking. Viral capsids are an appealing choice as they self–assemble from few proteins and can often be expressed and purified from bacterial cells. These virus–like particles are devoid of any viral genetic material and thus completely non-infectious: they cannot reproduce the physiological infection pathway, however they are well–suited as model systems. I started developing a large cargo model based on the HBV capsid, which is the largest cargo observed to cross the NPC intact (see Introduction). I then sought to expand the "toolkit" with cargoes of smaller diameter, and turned to the bacteriophage MS2 capsid to create two additional model cargoes. Finally I added a fourth cargo based on a *de novo* designed, two–component, capsid.

3.1.1 Design of a large cargo based on the HBV capsid

The HBV core protein contains a NLS sequence in its C terminus, which is typically buried inside the capsid. Its exposure (and therefore its accessibility to bind the transport machinery) is phosphorylation–dependent and not well characterized: this is not ideal if one wishes quantitative control over the system. I therefore sought to develop a new construct which would allow exact knowledge and control of the

NLSs available for binding to importins. As the basic C–terminal sequence of the core protein (amino acids 150-183) has been shown to be unnecessary for capsid assembly [113], I based the constructs on an assembly–competent truncated version of the core protein (1-149). This truncation leads to higher levels of bacterial expression and to a predominance of the T=4 capsid with no obvious change in capsid morphology [114]. The core protein thus assembles into 36–nm capsids from 12 pentameric and 30 hexameric units, for a total of 240 copies. In addition, the truncation also results in the removal of the native capsid NLSs, enabling a complete control over number of exposed NLSs via surface engineering.

In order to develop a HBV capsid variant suitable for nuclear import experiments, I started from a version of the capsid generated by a former PhD student in the group on the basis of the SplitCore concept [106] (see Figure 3.1A). In this construct, the core protein of HBV is split in two halves (coreN and coreC), which self–assemble together before forming the capsid. This enables the fusion of additional proteins to the termini which will be exposed at the capsid surface after assembly. The construct included a split–GFP to allow for visualization of the sample and the core protein was additionally fused to a canonical NLS sequence, giving a 1:1 correspondence between number of core proteins in the capsid and NLSs. Unfortunately, this sample was quite aggregation–prone and one issue was also that the GFP protein is in itself almost as large as the capsid protein, therefore the fusion resulted in a larger capsid compared to the wild type HBV (more than 40 nm in diameter), which might be beyond the physiological transport capabilities of the NPC. In addition, the GFP does not have ideal photophysical properties for high–resolution applications such as single–particle tracking (rapid photobleaching).

I then devised a strategy based on a direct insertion of the NLS sequence into the HBV coat protein. This would result in capsids of comparable size to the wild–type ones, and the lack of an intermediate assembly step between the two split core proteins could result in improved sample stability. In order to identify a suitable site for the insertion which did not impair capsid assembly, I turned to the exposed loop in the c/e1 epitope (between residues D83 and D78), which has been previously shown to tolerate insertions as large as a GFP [115] (see Figure 3.1B). I also mutated a single residue in this exposed loop to a cysteine to allow coupling to a fluorescent dye via maleimide reaction. As each core protein can potentially be labelled, this would result in very bright particles with up to 240 fluorescent dyes and 240 exposed NLSs. After optimizing the purification protocol to remove contamination of *E. coli* membrane proteins by adding a detergent to the buffers (see Methods), I could purify capsids from this construct. I tested the capability of these capsid to bind impα and impβ with an *in vitro* FRET assay, monitoring the energy transfer between the dye on the capsid and labelled impβ with increasing concentrations of impα. I could detect some binding in these assays, but I also observed competition of the dye site and binding of importins to the NLS (likely due to sterics).

Lastly, I designed a construct based on a minimal modification of the HBV core protein: a single cysteine mutation in the exposed loop is used to attach tags of choice to the capsid via maleimide labelling (see Figure 3.1C). I reasoned that this minimal modification could result in improved sample stability, and the attachment of a NLS peptide via a short flexible linker would ensure better binding to importins.

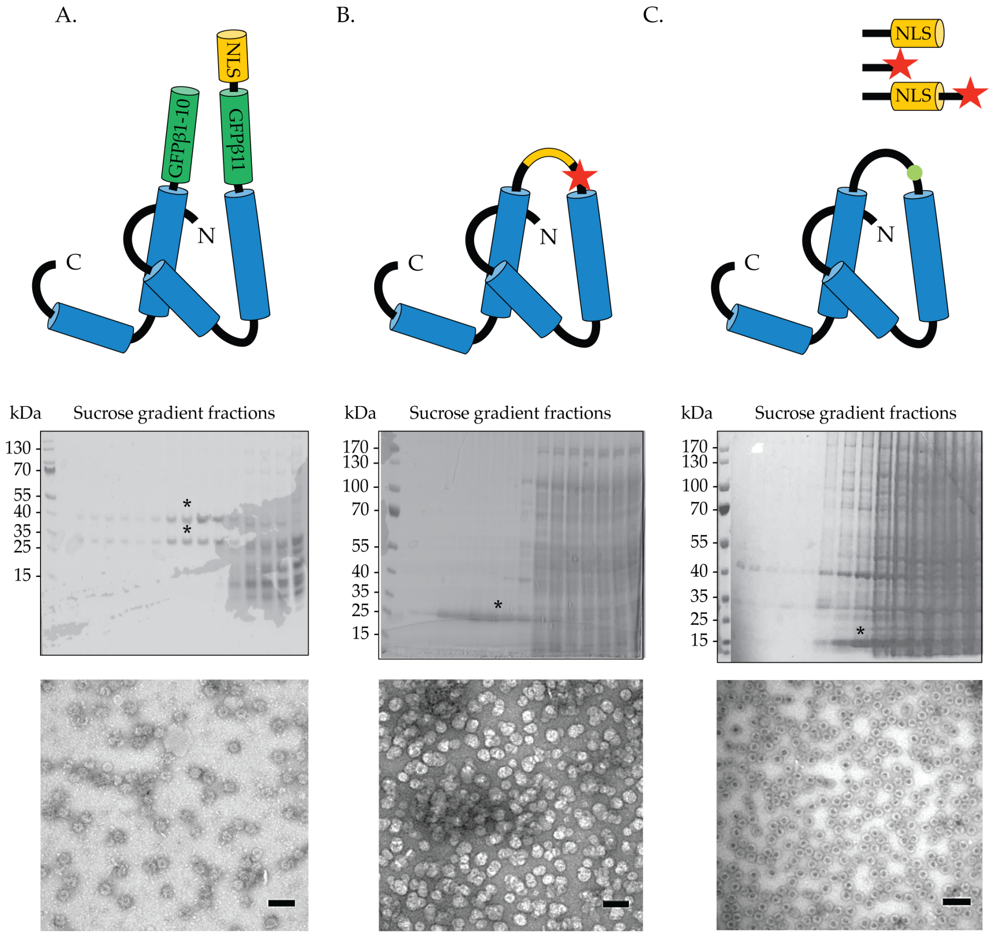

FIGURE 3.1: Constructs for a large cargo derived from HBV capsid. The top row depicts schematic representations of the constructs, the middle row SDS-PAGE gels of the sucrose gradient purification with Coomassie staining (protein of interest indicated by an asterisk) and the bottom row negative staining EM images of the samples (the scale bar is 100 nm). Panel A corresponds to the SplitCore construct with a SplitGFP–NLS fusion (note that the two bands on the gel correspond to the CoreN and CoreC proteins). Panel B displays the construct with insertion of the NLS sequence in the core protein sequence (in orange), and additional cysteine for labelling with a dye (red star). Panel C shows the final construct based on a single cysteine mutation of the core protein (green dot), used to couple different tags. Note that this capsid can appear as monomer or dimer on the gel in a concentration–dependent way.

Labelling strategy

The cysteine mutant capsids offers up to 240 labelling sites which can be coupled to a maleimide–reactive tag of choice. Initially I tagged the capsids with synthetic NLS peptides containing a dye (see Materials and Methods for a list of all peptides used). The labelling was successful and the peptides were functional, however I observed substantial precipitation of the capsid–peptide mixture during labelling. Another issue was that we observed a residual contamination of free peptide even after size–exclusion purification: as it contained both a NLS and a dye, this resulted in nuclear background from the free peptide which interfered with the interpretation of the transport experiments. I then tested NLS peptides without a dye, which resulted in much less precipitation and thus allowed reaching higher labelling ratios. In this case, I incubated capsids with a mixture of unlabelled NLS peptide and a maleimide–reactive dye of choice to obtain samples with both tags (see Figure 3.2B). Despite some minor dye sticking, I was able to purify capsids tagged with both labels (see Figure 3.2C), and the sample suffered from less aggregation problems. One key advantage of this labelling strategy is that the NLS content can be tuned by changing the conditions of the labelling reaction, whereas the previous approaches were limited to a single fixed number of NLSs. This construct therefore represents an ideal platform to study transport of a large cargo with minimal modification and complete control over the surface tagging procedure.

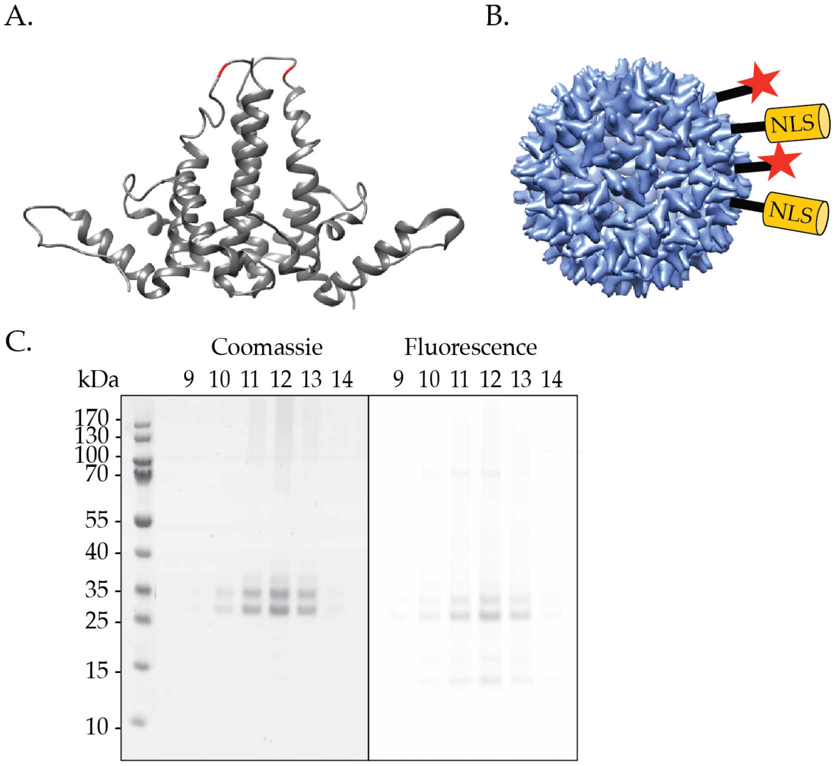

FIGURE 3.2: Dual labelling strategy for a large cargo derived from the HBV capsid. (A) Structure of the HBV core protein dimer (structural unit of the capsid), with the sites of surface cysteine mutations highlighted in red (PDB: 1QGT). (B) Schematic representation of the mixed NLS/dye labelling of the capsid (PDB: 1QGT, the capsid structure was rendered in Chimera). (C) SDS-PAGE gel of Sephacryl fractions after the labelling reaction. The left panel corresponds to Coomassie staining and the right one to fluorescence scan of the gel. The top band in the gel corresponds to core protein tagged with NLS, and the bottom one to unlabelled protein or protein tagged with the dye. In this sample, some unspecific sticking of the dye to the protein was also observed (fluorescence in the top gel band).

3.1.2 MS2 and MS2_S37P capsids

As discussed in the Introduction, one of the main aims of this thesis is to study large cargo import into the nucleus, with particular focus on the effect of exposed NLSs and size. In order to explore the role of size, I sought to expand the large cargo "toolkit" with capsid–like particles of different diameter which could be compared with the HBV–derived cargoes. As HBV likely represent the upper limit of the NPC transport capabilities, it would be very informative to explore and compare large cargoes of smaller sizes. I applied a strategy based on the one presented above for HBV to develop two additional cargoes based on the bacteriophage MS2 capsid. This virus is characterized by a 28 nm wide capsid formed by a single protein (coat protein), which assembles into dimers and then into a icosahedron with 12 pentameric and 20 hexameric faces. The MS2 capsid has been studied as a potential drug delivery agent [116], and it has previously been shown to tolerate point mutations for surface labelling [117]. Additionally, a single point–mutation (S37P) was shown to alter the capsid assembly, causing smaller particles of 18 nm in diameter (consisting of 12 pentamers) to form [118].

I designed cysteine–mutant versions of both wild type and S37P mutant MS2 capsids, exploiting the threonine 15 site which had been shown in literature not to interfere with capsid assembly and stability (see Figure 3.3A). The mutations result in 180 accessible sites for the MS2 capsid and 60 for the MS2–S37P capsid. I could purify both capsids and tag them with NLS peptide and dye as previously described (see Figures 3.3B-C). As the coat protein tagged with NLS peptide presents a clear shift on SDS-PAGE gels due to its increased molecular weight, this enables a robust quantification of the #NLSs bound to the samples. The two additional capsids allowed me to expand the large cargo toolkit, now spanning a range of sizes from 18 to 36 nm.

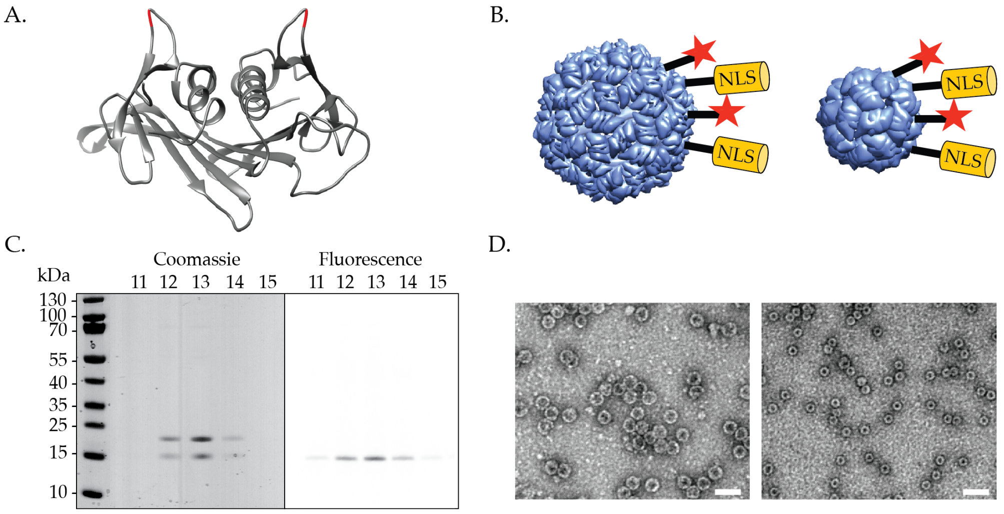

FIGURE 3.3: Large cargoes derived from the bacteriophage MS2 capsid. (A) structure of the MS2 coat protein dimer (structural unit of the capsid), with the sites of surface cysteine mutations highlighted in red (PDB: 2MS2). (B) Schematic representation of the mixed NLS/dye labelling of MS2 and MS2-S37P capsids (PDB: 2MS2 and 4ZOR, the capsid structures were rendered in Chimera). (C) SDS-PAGE gel of Sephracryl fractions after the labelling reaction. The left panel corresponds to Coomassie staining and the right one to fluorescence scan of the gel. The top band corresponds to the coat protein tagged with NLS peptide, and the bottom band corresponds to unlabelled protein or protein tagged with the dye. (D) EM images of MS2 and MS2-S37P capsid samples (scale bar corresponds to 50 nm).

3.1.3 I53-47 capsid

As I found a dramatic difference in the behaviour of the previous samples in cellular nuclear transport assays (which I will present in the next section), I sought to include an additional capsid which could bridge the sizes of the two MS2 variants (18 and 28 nm). I turned to *de novo* designed capsids from David Baker's group [105]. These capsids have been developed via computational design and they are formed by two different proteins which self–assemble in particles of predetermined size. I focused on the I53-47 variant which - with a diameter of 23 nm - represents an ideal intermediate cargo between the two MS2 variants. This capsid is formed by 12 pentamers of the chain A protein and 20 trimers of the chain B aligned along the fivefold and threefold icosahedral symmetry axes, respectively.

In order to achieve surface–tagging of the I53-47 capsid, I applied a similar strategy as the one outlined above. As the capsid did not present any exposed cysteines, the first step was to identify a suitable site to introduce a surface cysteine mutation which would not interfere with capsid assembly and stability. To do so, I turned to a recent work from the Baker's lab [119] where different exterior mutations were tested on the I53-50 capsid. As the chain B with the mutated site closely resembles chain B in I53-47 capsids, I reasoned that these sites might ensure capsid stability upon their mutation. I tested two of these residues (D43 and E67) to introduce a surface cysteine on the I53-47 capsid. Both versions could be successfully purified as intact capsids, however the samples presented a higher amount of unassembled proteins, which is undesirable as they could also react with the peptide/dye during labelling. I therefore optimized the purification procedure to remove the majority of unassembled proteins, with an additional size–exclusion step via tangential flow filtration (see Materials and Methods for details).

I then proceeded with the D43 variant for labelling with NLS peptide and dye using the previously developed strategy (see Figure 3.4). The reaction was successful and resulted in capsids tagged with a mixture of NLS and dye, albeit one limitation of this construct is that the maximum number of exposed sites is 60 (as only one chain contains the cysteine mutation). Nevertheless, the construct based on the I53-47 capsid allowed me expand the large cargo size range to be investigated in transport experiments.

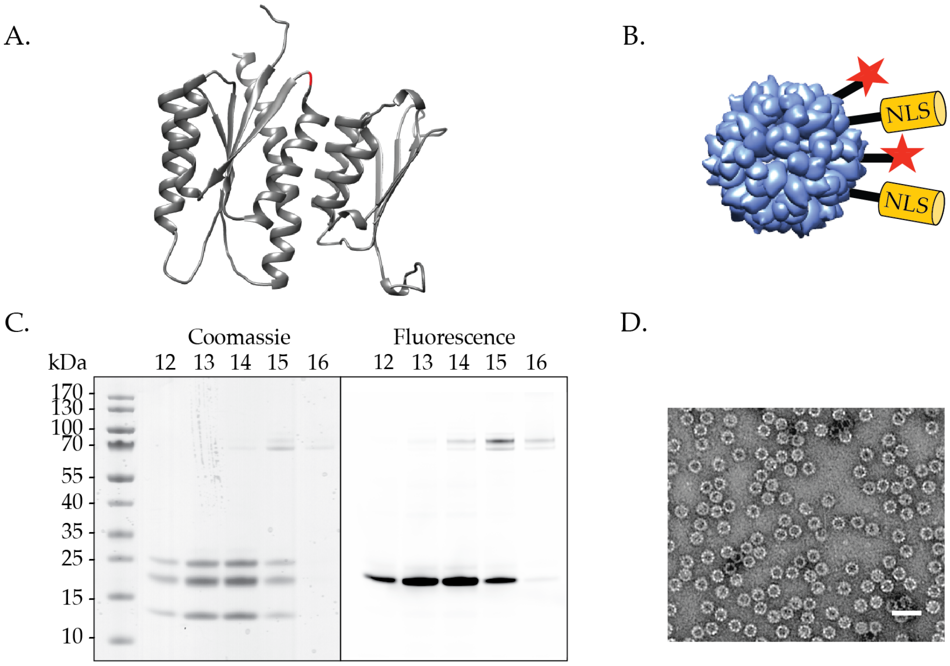

FIGURE 3.4: Large cargo derived from the I53-47 capsid. (A) structure of the two protein chains of the I53-47 capsid, with the site of surface cysteine mutation D43C highlighted in red. (B) Schematic representation of the mixed NLS/dye labelling of I53-47 capsids (the capsid structure was rendered in Chimera). (C) SDS-PAGE gel of Sephracryl fractions after the labelling reaction. The left panel corresponds to Coomassie staining and the right one to fluorescence scan of the gel. The bottom band corresponds to chain A without cysteine mutation, the top two bands to the protein chain B with cysteine mutation coupled to NLS peptide (top) and dye (bottom). (D) EM image of the I53-47 capsid samples (scale bar corresponds to 50 nm).

3.1.4 Overview of the large cargo "toolkit"

The strategy presented here allowed me to obtain four differently–sized capsids in a diameter range of 18-38 nm (see Figure 3.5 for an overview of sizes, validated by DLS measurements), suitable for nuclear import studies. A major advantage of the double–labelling approach I developed is that it enabled the purification of capsids characterized by a wide range of exposed NLSs (see Table 3.1 for a comprehensive overview of all samples employed in this thesis).

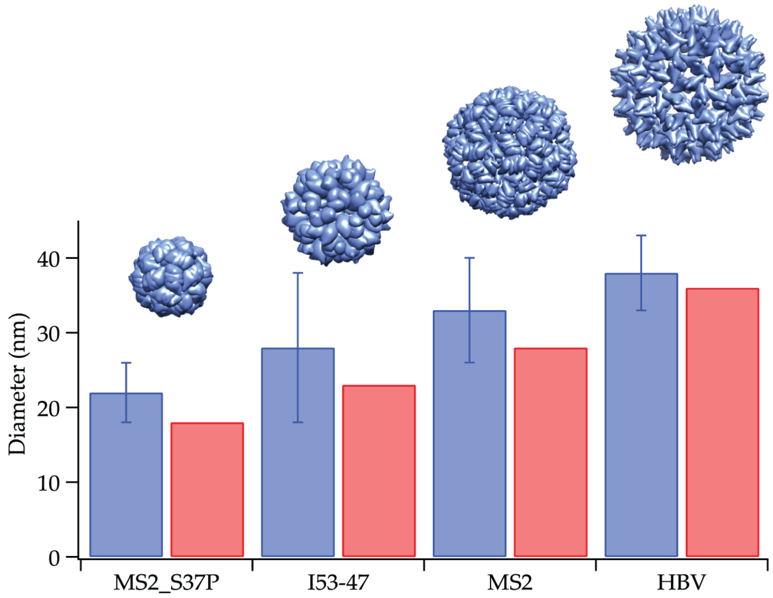

FIGURE 3.5: Overview of the large cargo "toolkit". The plot displays the cargo diameters as measured with DLS (blue bars) compared with reference values from literature and structural information (red bars). The corresponding capsid structures, rendered in Chimera, are overlaid on the top.

Capsid	**Label**	**#NLSs**
HBV	Cy3B	0
HBV	NLS, A647	120
HBV_NLS insert	CF680	240
MS2	Cy5	0
MS2	NLS, A647	60
MS2	NLS, A647	100
MS2_S37P	A647	0
MS2_S37P	NLS, A647	14
MS2_S37P	NLS, A647	18
MS2_S37P	NLS, A647	20
MS2_S37P	NLS, A647	23
MS2_S37P	NLS, A647	29
MS2_S37P	NLS, A647	38
I53_47	A647	0
I53_47	NLS, A647	18
I53_47	NLS, A647	22
I53_47	NLS, A647	25
I53_47	NLS, A647	29
I53_47	NLS, A647	32
I53_47	NLS, A647	44

TABLE 3.1: List of capsid samples employed in this study. The tags used for labelling and the resulting #NLSs are indicated.

3.2 Effect of multiple NLSs and size on the nuclear import of large cargoes

3.2.1 Determination of minimum #NLSs for bulk import of large cargoes

Equipped with the newly developed cargo "toolkit", I then sought to investigate the nuclear transport properties of the different large cargoes. I carried out bulk nuclear import assays in permeabilized cells, as outlined in the Materials and Methods section, and imaged the cargo localization to different cellular compartments on a confocal microscope. The results for the four different capsids are outlined below, from the smallest to the largest cargo.

MS2_S37P capsids

I tested MS2_S37P capsid samples tagged with different numbers of NLSs, ranging from 0 to approximately 40 NLSs. Images for representative samples (after 1h of incubation) are presented in Figure 3.6. In these experiments I observed a striking dependence of MS2_S37P capsid localization on the number of NLSs. Samples without NLSs were not targeted to the nuclear envelope at all, as would be expected. Increasing the #NLSs resulted in clear targeting of the MS2_S37P capsids to the nuclear envelope, however samples with 14 NLSs still did not show any significant bulk accumulation into the nucleus. Further increasing the #NLSs resulted in a progressively more efficient nuclear accumulation of the capsids. Typically, samples which were more efficiently imported into the nucleus displayed less accumulation at the envelope (see for instance the images of capsids with 18 NLSs versus 29 NLSs). These results indicate that a large cargo such as the 18 nm MS2_S37P capsid requires a minimum #NLSs (and therefore bound impα/impβ) in order to cross the NPC permeability barrier and enter the nucleus. Comparison of all MS2_S37P samples (see Table 3.1 for a complete list) enabled me to determine this minimum cutoff to be approximately equal to 15 NLSs for this capsid.

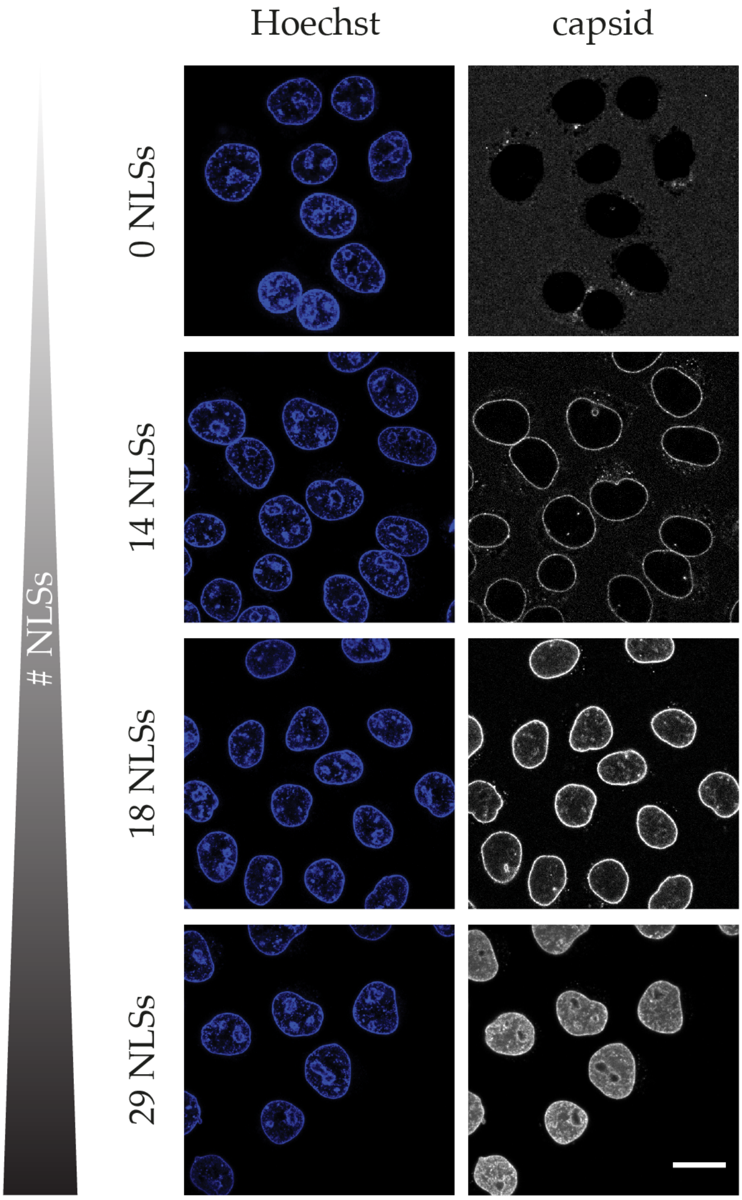

FIGURE 3.6: Confocal microscopy images of nuclear import of MS2_S37P capsids. Permeabilized cells were incubated for 1 h with capsid samples tagged with different numbers of NLS peptides. Here some representative samples are depicted which display different behaviour in response to the #NLSs. As the samples have different brightness, contrast has been adjusted individually for optimal visualization. The scale bar corresponds to 20 μm.

I53-47 capsids

For the I53-47 capsid, I tested samples with a #NLSs ranging from 0 up to approximately 44 NLSs. Results for representative samples are presented in Figure 3.7. The main features of the NLS–dependent behaviour found for the MS2_S37P capsid appeared to be conserved. Without NLSs, the capsid was not targeted to the nuclear envelope and its signal was mostly cytoplasmic. Increasing the #NLSs resulted in strong nuclear envelope targeting. Lastly, higher #NLSs corresponded to bulk accumulation of the capsids in the nucleus. The I53-47 capsid thus closely matched what had been observed for the smaller MS2_S37P capsid, with some minor differences. The I53–47 had a dotty rather than diffuse pattern inside the nucleus, and the samples with lower #NLSs were characterized by higher cytoplasmic background. The minimum #NLS for this capsid was also around 15-18 nm, despite some dim residual nuclear signal, which could arise from a contamination of capsid fragments.

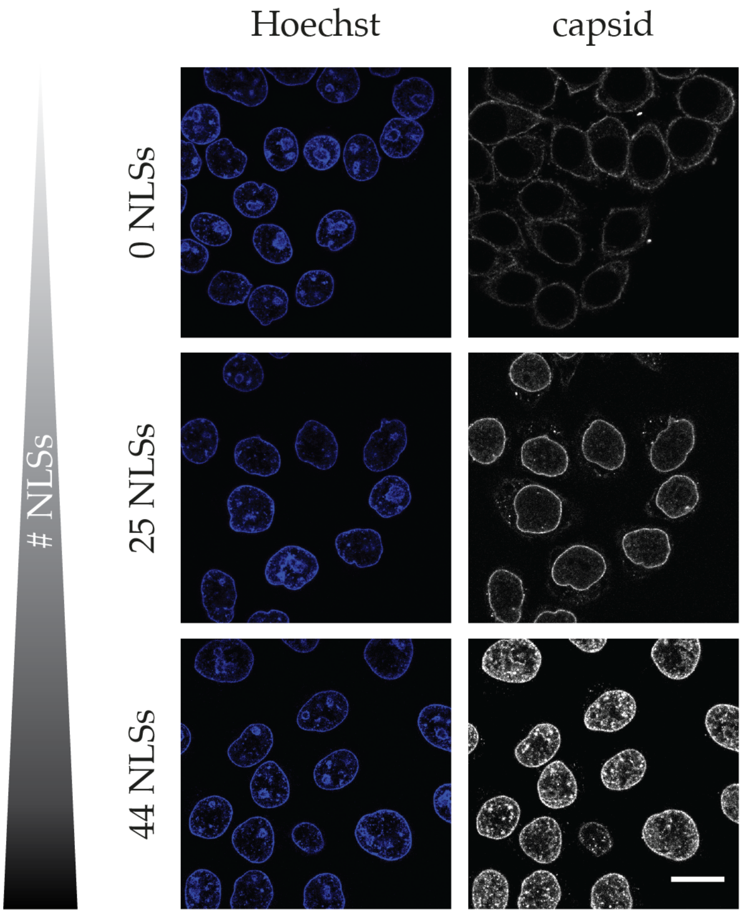

FIGURE 3.7: Confocal microscopy images of nuclear import of I53_47 capsids. Permeabilized cells were incubated for 1 h with capsid samples tagged with different numbers of NLS peptides. Here some representative samples are depicted which display different behaviour in response to the #NLSs. As the samples have different brightness, contrast has been adjusted individually for optimal visualization. The scale bar corresponds to 20 μm.

MS2 capsids

Results for representative MS2 capsid samples are presented in Figure 3.8. The nuclear import of this 28 nm large capsid is overall much less efficient than the two smaller ones previously presented. Even in samples with as many as 60 NLSs I did not observe any bulk signal in the nucleus, despite a strong targeting to the nuclear envelope. I reasoned that these larger particles might require an even higher #NLSs for successful barrier crossing. Indeed I found that increasing the #NLSs up to 100 resulted in a distinct bulk accumulation in the nucleus (albeit still much less efficient than the smaller capsids). The NLS–dependent nuclear targeting and import behaviour thus can be found consistently in large cargoes across the size range of 18-28 nm, and larger cargoes appear to require higher #NLSs, with a drastic increase for the MS2 capsid.

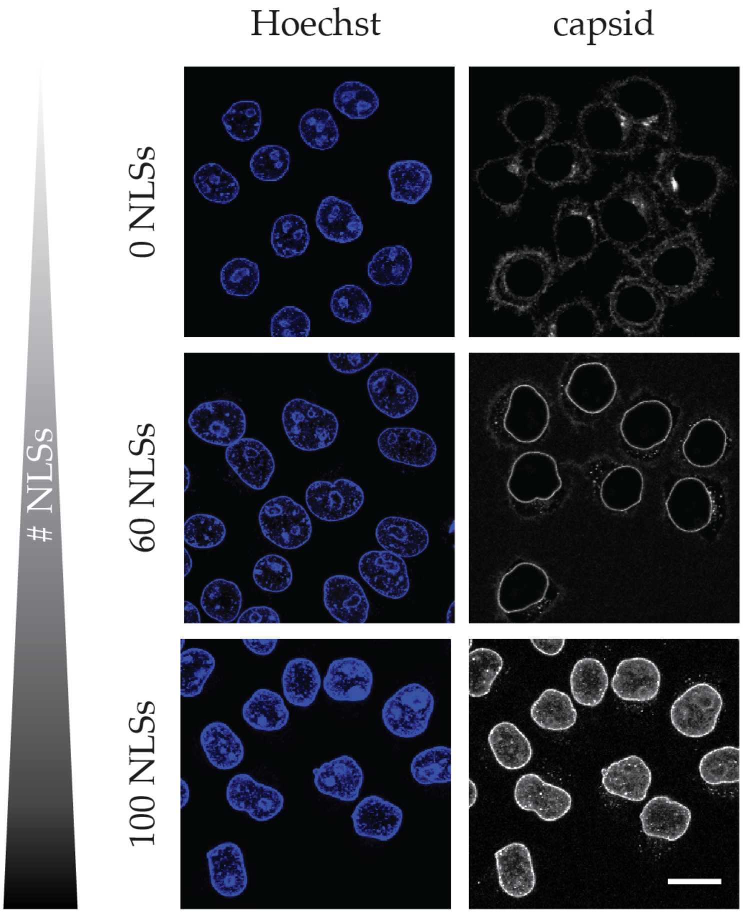

FIGURE 3.8: Confocal microscopy images of nuclear import of MS2 capsids. Permeabilized cells were incubated for 1 h with capsid samples tagged with different numbers of NLS peptides. Here some representative samples are depicted which display drastically different behaviour in response to the #NLSs. The scale bar corresponds to 20 μm.

HBV capsids

HBV capsids are the largest cargo I tested, with a diameter of 36 nm. Results for representative samples are presented in Figure 3.9. Similarly to the MS2 capsid, HBV import is highly inefficient: tagging with NLS peptides conferred a stronger nuclear envelope targeting compared to the samples without NLSs, however no bulk accumulation was observed in the nucleus for samples with up to 120 NLSs. It is possible that this very large cargo would require an even higher NLS content, which has been challenging to achieve via the labelling reaction. However, similar results were also observed with SplitCore capsids and samples based on a direct NLS fusion (resulting in up to 240 NLSs). Therefore, another possibility is that the minimal modification introduced into the core protein has an influence on the capsid which prevents its efficient import into the nucleus. This motivated me to investigate the precise localization of HBV capsids at the pore, in order to test whether a specific interaction with the NPC was present. I will outline and discuss these results in Section 3.3.

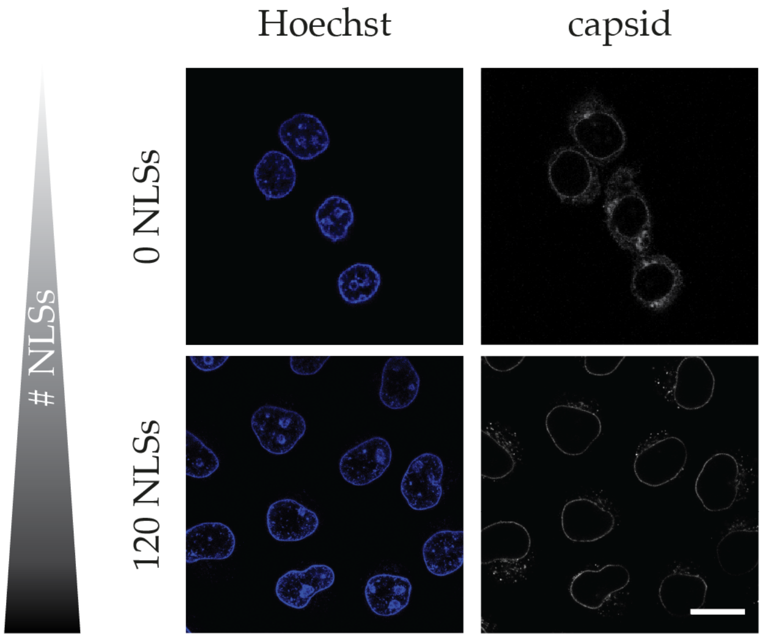

FIGURE 3.9: Confocal microscopy images of nuclear import of HBV capsids. Permeabilized cells were incubated for 1 h with capsid samples tagged with different numbers of NLS peptides. The scale bar corresponds to 20 μm.

Overview of NLS and size–dependent import

Figure 3.10 summarizes the findings of the ensemble nuclear import assays presented in this section, which enabled the determination of the minimum #NLSs for the import of different large cargoes. Each point represents a different sample, and the markers are color–coded according to whether the sample was observed to accumulate inside the nucleus during import assays over the course of 1-1.5 h. Interestingly, the NLS requirement appears to increase non–linearly with cargo diameter, with a relatively drastic increase between the 23 nm and 28 nm capsids.

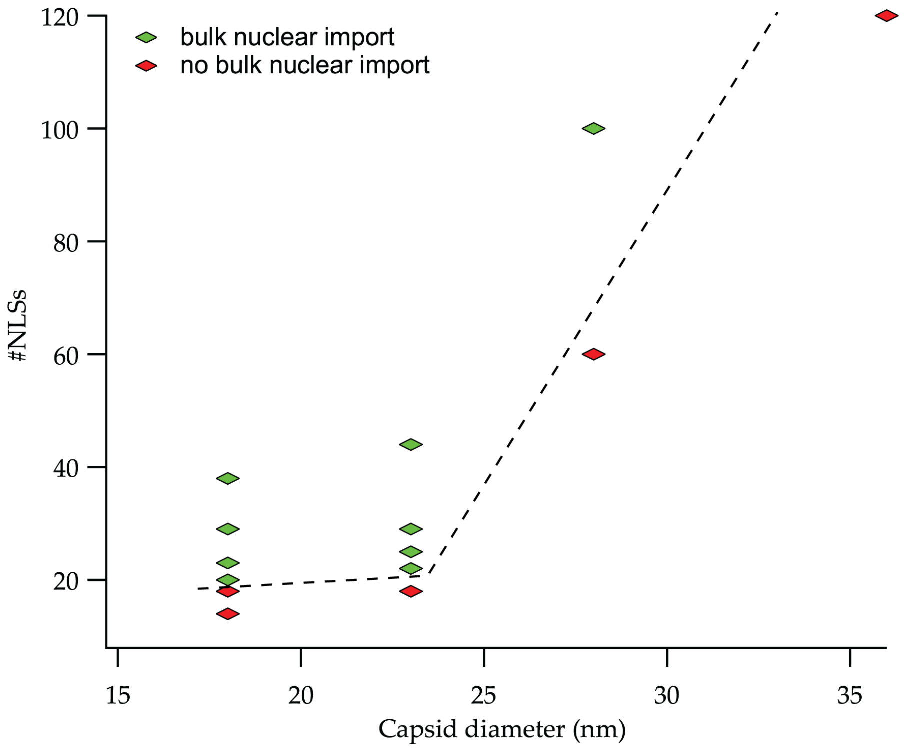

FIGURE 3.10: Overview of the minimum #NLSs required for bulk nuclear import of the four different capsids: MS2_S37P, I53-47, MS2 and HBV. Each point corresponds to a sample which was tested in import assays, color–coded according to whether bulk nuclear accumulation was observed over the course of 1h. The dashed line illustrates schematically the non–linear increase of minimum #NLSs with cargo size.

3.2.2 Kinetics of the nuclear import of large cargoes

Once I had characterized the nuclear import properties of different large cargoes by comparing their localization according to their size and #NLSs, I sought to obtain a more quantitative understanding of their import efficiencies. In order to do so, I developed an automated confocal microscopy pipeline to acquire nuclear import signal over a large number of cells and automatically process the data. I performed multi–position time–lapse imaging of the different samples, monitoring the transport every 2 minutes for 1.5 h. I acquired the signal from the capsid fluorescence, as well as two reference stains (Hoechst and Mitotracker) to perform segmentation and analysis of different areas of interest (nucleus, nuclear envelope, cytoplasm – see Materials and Methods for details and Figure 3.12 for a brief overview). This enabled me to monitor the fluorescence intensity from the capsids in the different regions over time, for a large pool of cells.

First, I established the kinetic measurement on a standard small cargo (traptavidin–GFP). Figure 3.11 depicts the average nuclear intensity quantified over time. For the positive control, the intensity increases initially very rapidly and then more slowly until saturation will be reached. I compared these results with two negative controls: traptavidin–GFP–NLS in absence of key transport mix components and the same cargo without NLS. The quantification of the latter two shows no increase of nuclear signal over time.

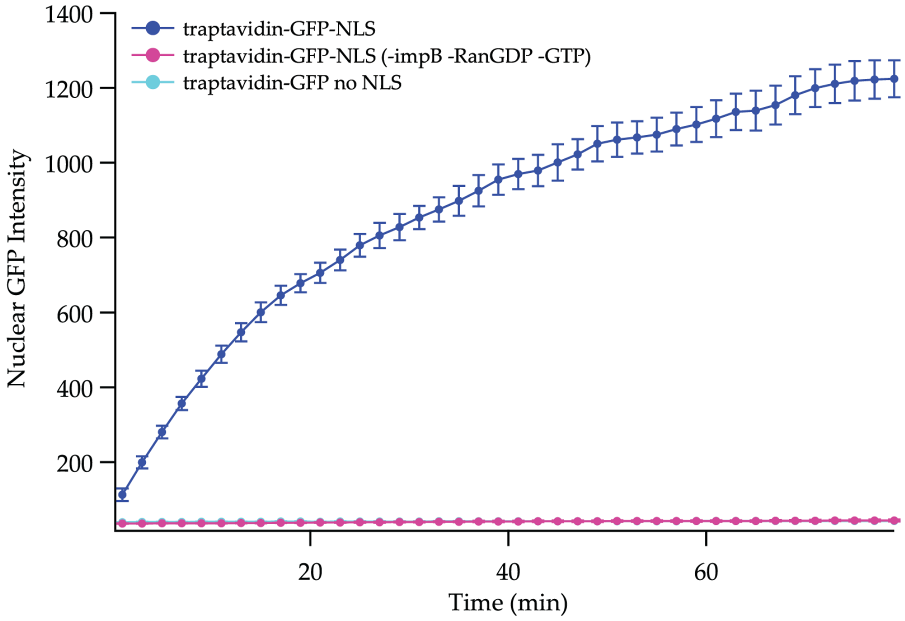

FIGURE 3.11: Nuclear import kinetics for a standard cargo. Curves depict the average fluorescence in the area of interest, measured in 12 different areas (the error bars correspond to the standard deviation).

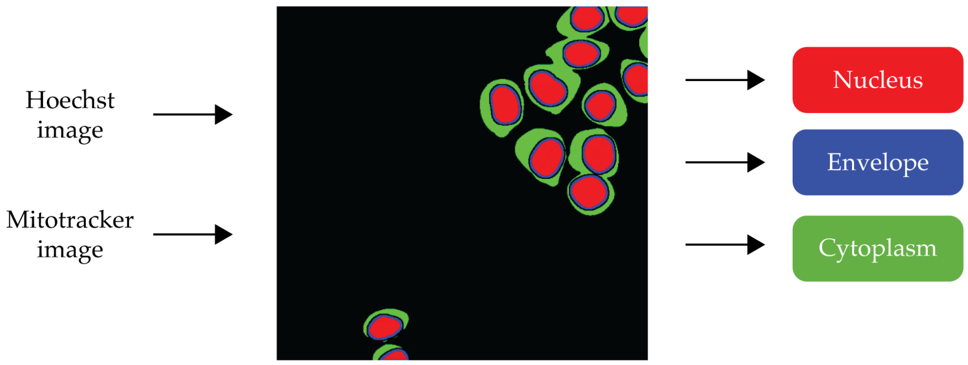

FIGURE 3.12: Overview of analysis pipeline for ensemble kinetics experiments. Reference images of the Hoechst and Mitotracker stains are used at each frame to create three masks and isolate the regions of interest: nucleus, nuclear envelope and cytoplasm. The masks are then applied to the images acquired in the capsid channel to measure the intensity in the different areas.

Raw import kinetics of capsid samples

Once I had tested the automated microscopy approach for quantifying the nuclear import kinetics of a standard fluorescent cargo, I then proceeded to characterize the large cargo samples. Representative raw curves showing the capsid signal in the three regions of interest (nucleus, nuclear envelope and cytoplasm) are shown in Figure 3.13 for MS2_S37P capsid samples with a #NLSs ranging from 14 to 38.

A few general trends can immediately be observed by comparing the signal in the different areas of interest: samples which have little or no nuclear import have low nuclear intensity - sometimes comparable to the cytoplasmic signal - and most of the intensity is localized at the nuclear envelope. Samples with higher #NLSs have a nuclear intensity which reaches and then surpasses the envelope signal, and both are substantially higher than the cytoplasmic fluorescence. These features of the kinetic curves recapitulate what was previously qualitatively observed in the confocal snapshots (Figure 3.6). For all MS2_S37P samples I confirmed with three independent biological replicates that the results could be obtained robustly.

I then followed the same approach to quantify the import kinetics of the I53-47 and MS2 capsids: I excluded the HBV capsids from these experiments as they did not show bulk nuclear signal under any of the conditions tested. Representative raw curves for the import kinetics of the I53-47 capsids are depicted in Figure 3.14 for samples ranging from 18 to 44 NLSs and Figure 3.15 displays typical curves for MS2 samples ranging from 60 to 100 NLSs. The overall features of the kinetic curves are conserved for these two larger capsids. Note that for these more inefficient samples the nuclear signal at most equals, but never surpasses, the nuclear envelope signal. For the 28 nm MS2, as was also noted in the previous confocal images (Figure 3.8), the envelope is especially bright. This complicates the exact quantification of the nuclear signal, as it is contaminated by some "bleed–through" of the envelope signal into the nuclear ROI. It is probably for this reason that the MS2 with 60 NLSs appears here to have some nuclear signal increase, despite my earlier observations of this #NLSs being insufficient for nuclear import.

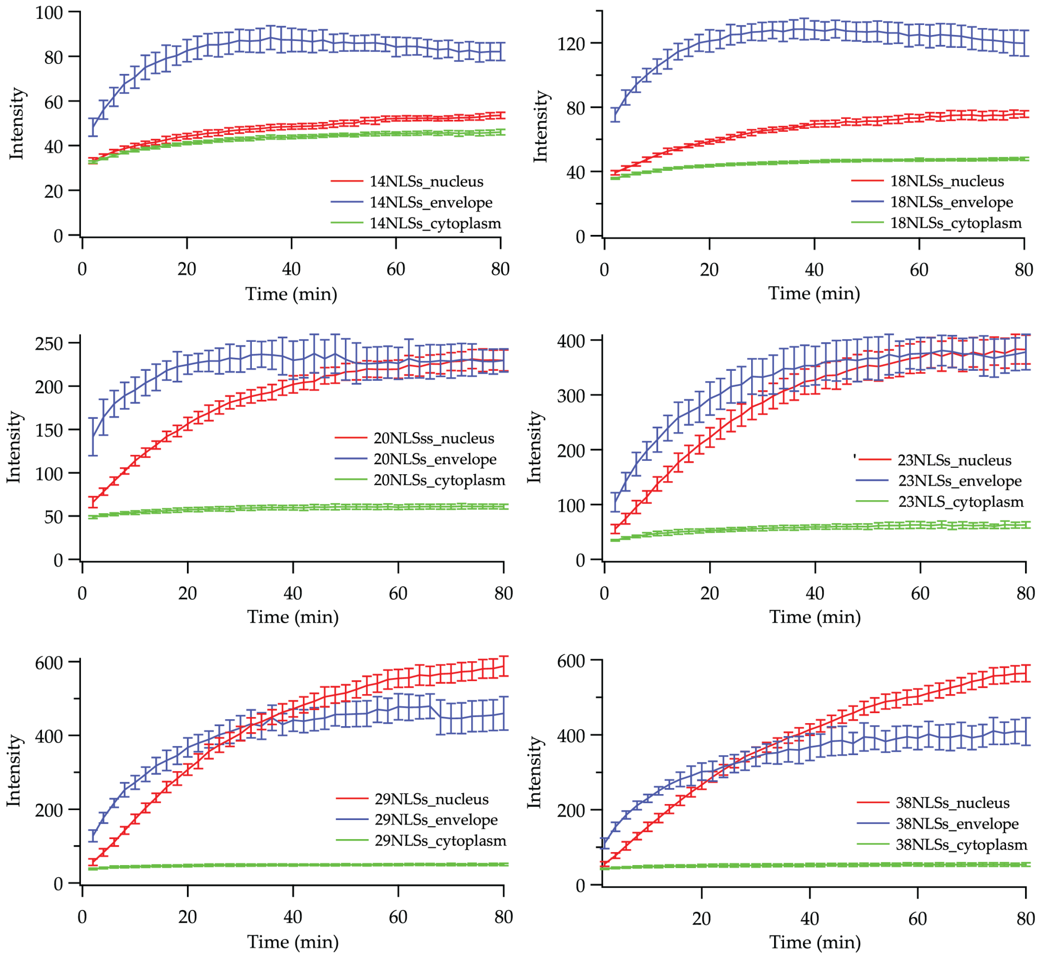

FIGURE 3.13: Raw intensity kinetics of MS2_S37P signal in different cellular compartments. The fluorescence intensity of the capsids was measured from confocal images using a mask to isolate the signal from the nucleus, nuclear envelope and cytoplasm (see Materials and Methods for more details on the analysis). Curves depict the average fluorescence in the regions of interest, measured in 12 different areas (each typically containing around 10 cells). The error bars correspond to the standard deviation.

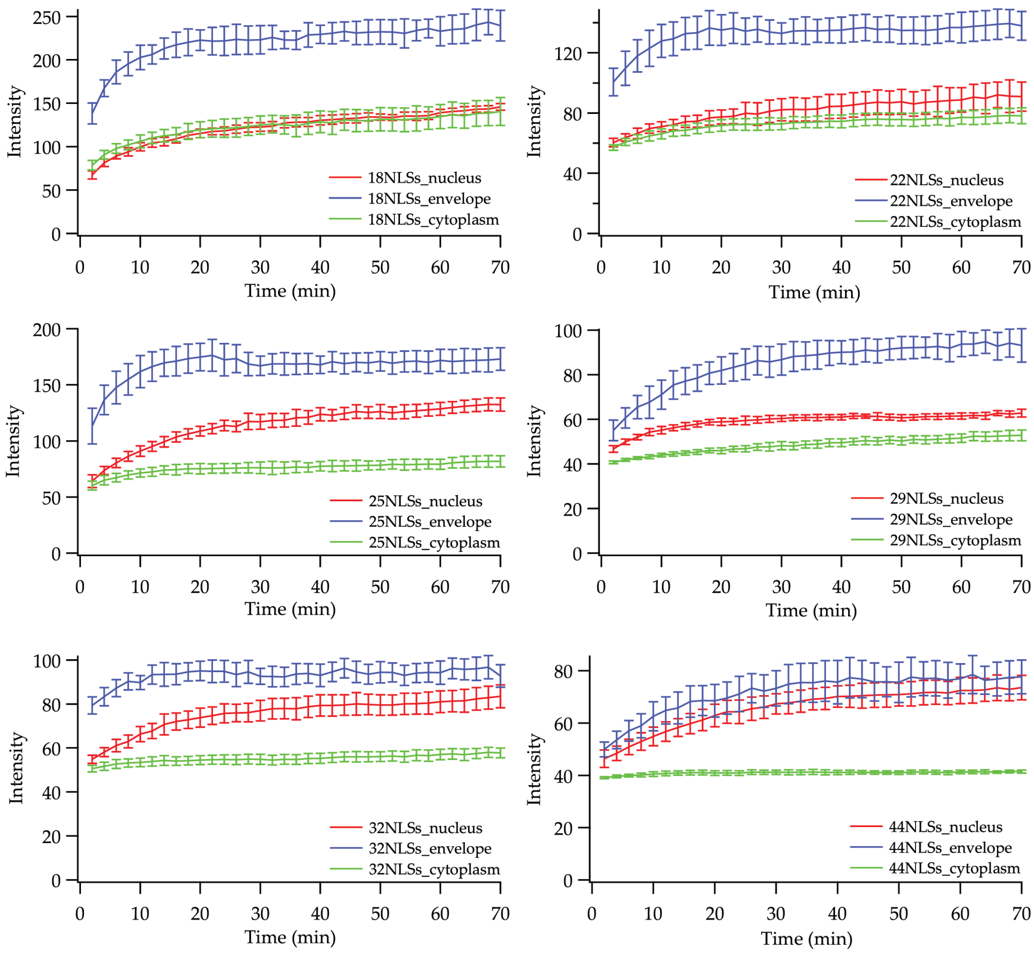

FIGURE 3.14: Raw intensity kinetics of I53-47 signal in different cellular compartments. The fluorescence intensity of the capsids was measured from confocal images using a mask to isolate the signal from the nucleus, nuclear envelope and cytoplasm (see Materials and Methods for more details on the analysis). Curves depict the average fluorescence in the regions of interest, measured in 12 different areas (the error bars correspond to the standard deviation).

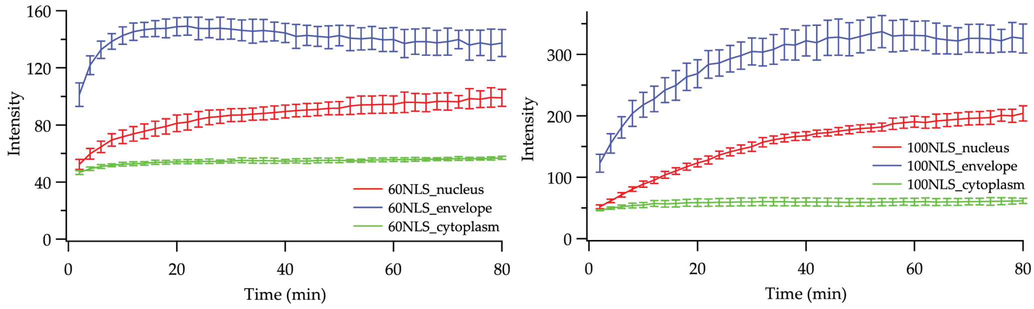

FIGURE 3.15: Raw intensity kinetics of MS2 signal in different cellular compartments. The fluorescence intensity of the capsids was measured from confocal images using a mask to isolate the signal from the nucleus, nuclear envelope and cytoplasm (see Materials and Methods for more details on the analysis). Curves depict the average fluorescence in the regions of interest, measured in 12 different areas (the error bars correspond to the standard deviation).

Precise determination of capsid concentration and brightness

I then focused on the nuclear intensities in order to compare the import efficiencies of the different capsids. As the samples have different labelling ratios (number of dyes per particle), it was necessary to devise a correction for the raw intensities in order to compare them quantitatively. The concentration of the capsid samples is typically quite low (< 50 mM), thus precise protein quantification with colorimetric assays was biochemically challenging. Quantification via absorbance measurements at 280 nm were also impaired due to scattering caused by the large capsids and absorbance at 260 nm from to the *E. coli* nucleic acids encapsidated in the particles. In order to address this issue I sought to identify a suitable technique to quantify the number of capsid particles and fluorescent dyes present in each sample. FCS (Fluorescence Correlation Spectroscopy) is a method that can be used to precisely measure the number, brightness, and diffusional properties of labelled particles in solution. Due to its sensitivity and precision, I reasoned that this method could be ideal to exactly quantify the concentration and labelling ratio of the different capsid samples.

I measured > 10 autocorrelation curves for each sample on a custom–built confocal spectroscopy setup (see the Methods chapter for more details). Representative curves are shown in Figures 3.16 and 3.17 for the MS2_S37P and I53-47 capsids. In order to extract the number of particles and their diffusion time, the FCS curves have to be fitted according to an appropriate theoretical model. Often, a two–component fit is employed to account for photophysical processes such as transition to a triplet state or cis/trans isomerization of the fluorophore. In the case of the capsid FCS traces, a single component fit (see Equation 2.2) was sufficient to obtain consistent results and allowed to me to calculate the number of particles and their diffusion time. By dividing the measured brightness by the number of particles and accounting for the brightness of a single Alexa647 dye, I could obtain a quantification of the number of dyes per capsid (see Table 3.2 for all parameters).

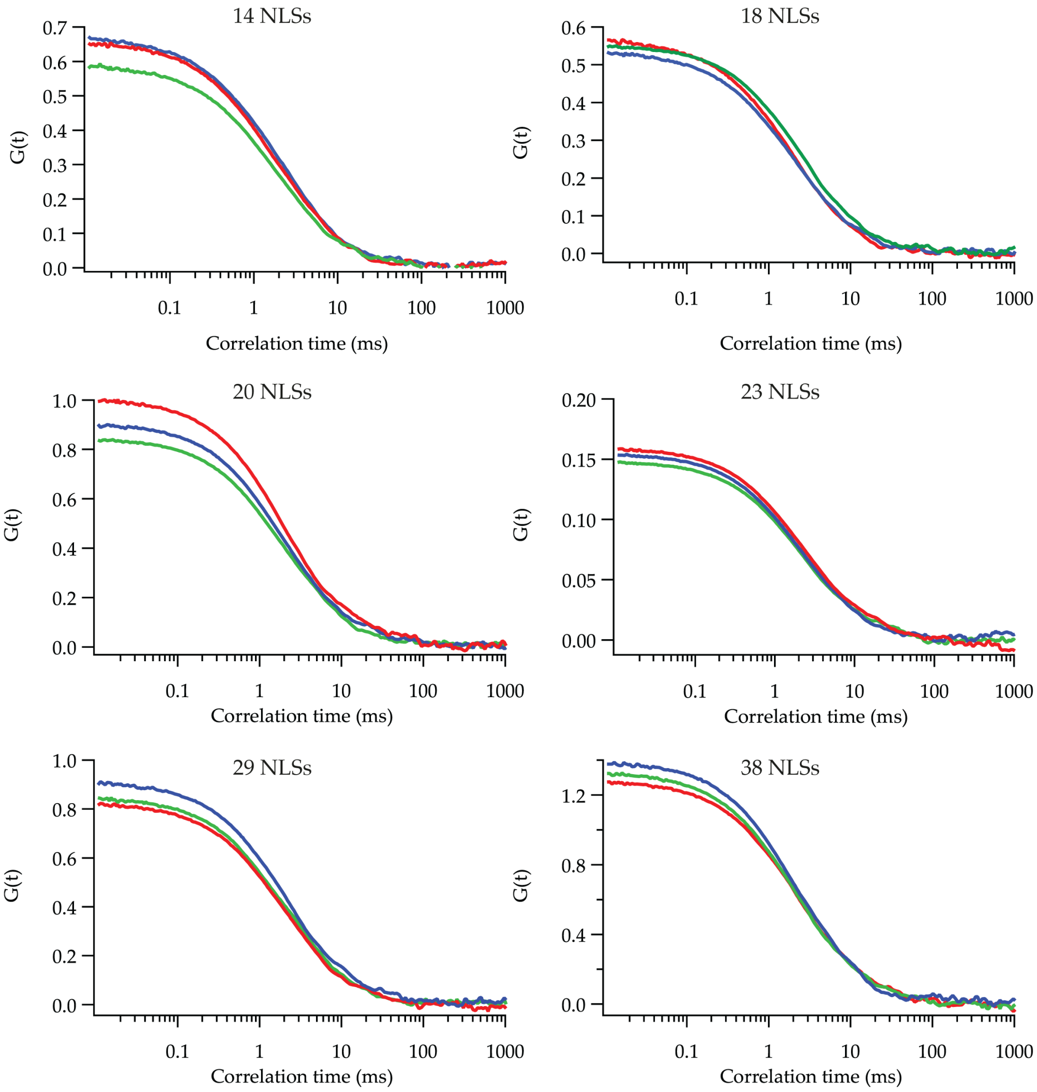

FIGURE 3.16: Representative FCS curves for MS2_S37P capsids. For each sample, at least 10 measurements of 30s were acquired and analyzed. The autocorrelation of the fluorescence intensity was calculated for lag times between 0.0001 and 1000 ms and fitted between 0.01 and 1000 (displayed on the plot) using the software Symphotime.

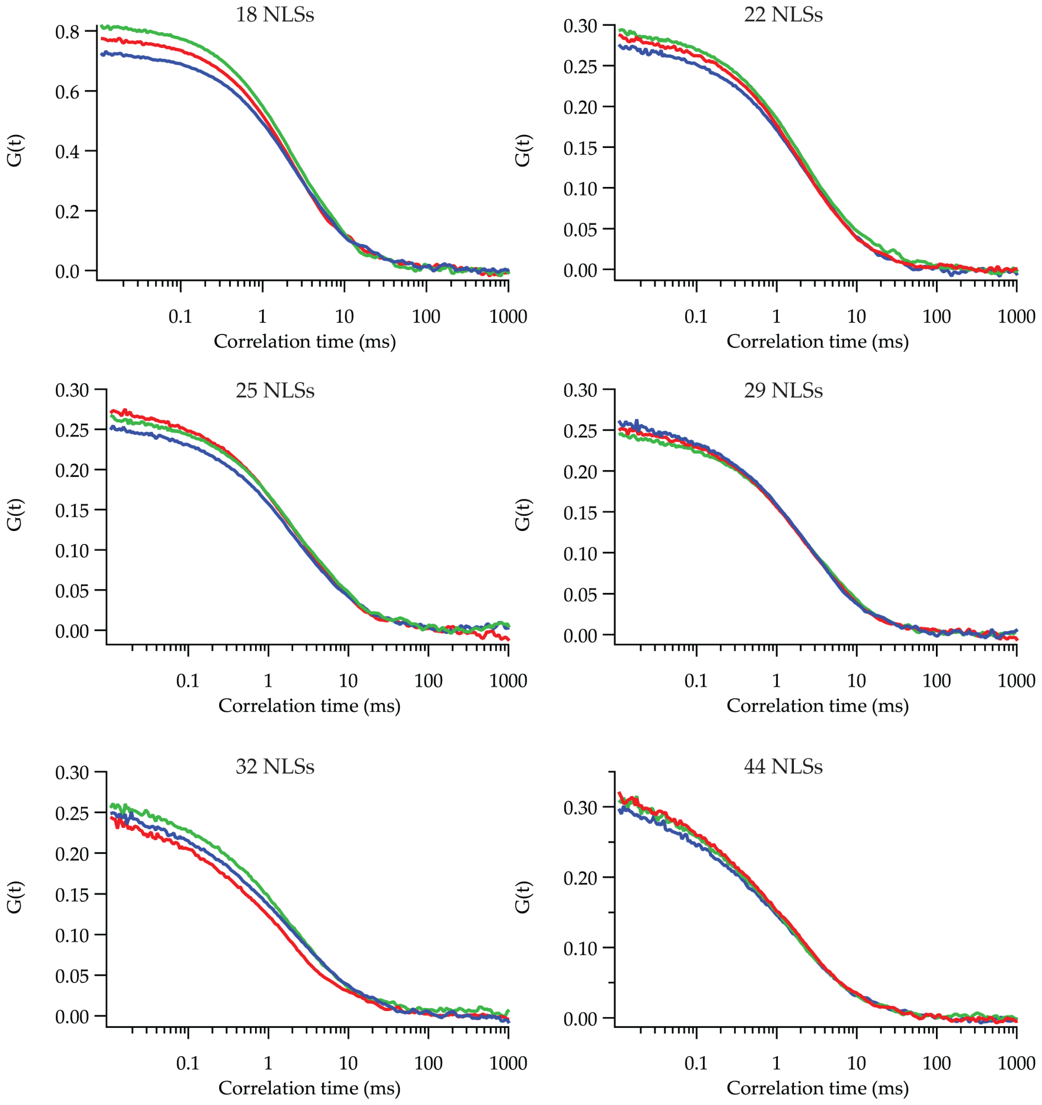

FIGURE 3.17: Representative FCS curves for I53-47 capsids. For each sample, at least 10 measurements of 30s were acquired and analyzed. The autocorrelation of the fluorescence intensity was calculated for lag times between 0.0001 and 1000 ms and fitted between 0.01 and 1000 (displayed on the plot) using the software Symphotime.

Sample	τ_{diff} (ms)	N	counts	dyes/capsid
MS2_S37P 14 NLSs	2.13	1.6	66	8
MS2_S37P 18 NLSs	2.18	2.0	82	8
MS2_S37P 20 NLSs	2.41	1.0	68	14
MS2_S37P 23 NLSs	2.61	6.8	473	14
MS2_S37P 29 NLSs	2.61	1.2	66	11
MS2_S37P 38 NLSs	2.65	0.7	53	14
I53-47 18 NLSs	2.56	1.3	77	12
I53-47 22 NLSs	2.29	3.5	92	5
I53-47 25 NLSs	2.39	3.9	99	5
I53-47 29 NLSs	2.38	3.8	83	4
I53-47 32 NLSs	1.96	4.2	69	3
I53-47 44 NLSs	1.62	3.4	44	3
MS2 100 NLSs	14	0.1	3.5	10

TABLE 3.2: Parameters obtained from fitting capsids FCS curves. The autocorrelation curves were fitted according to a diffusion model (see Methods for more detail). In order to calculate the number of dyes per capsid, the counts were divided by the number of particles and by a factor accounting for the brightness of a single Alexa647 dye (previously calibrated).

Corrected import kinetics of capsid samples

Once I had quantified the brightness of each capsid sample with FCS, I could use it to correct the nuclear intensities measured in the automated confocal imaging experiments. The corrected kinetic plots obtained are shown in Figure 3.18, focusing on the MS2_S37P and I53-47 capsids for which we can compare several samples that are bulk imported into the nucleus. All import curves could be fitted with an inverse exponential function:

$$I(t) = I_{max} * (1 - e^{-kt}) \tag{3.1}$$

The two key parameters are the plateau value I_{max}, which is proportional to the amount of imported capsids (import efficiency) and k, which relates to how fast saturation of import is reached. From k, one can also calculate the half–life $T_{1/2}$ required to reach 1/2 of the final nuclear intensity. In order to extract the initial import rate, I fitted the first 4 data points with a linear function, as in this time frame saturation does not yet play a substantial role. The parameters obtained from the fits are listed in Table 3.3 and plotted in Figure 3.18 (I focused only on comparing samples which previously showed some detectable bulk import).

For the 18 nm MS2_S37P capsid, I found that with increasing #NLSs, nuclear import reached saturation more slowly, which is reflected in a longer half–life. This increase was linear with #NLSs (see Figure 3.18 A and C). The number of particles imported into the nucleus A (import efficiency) also increased linearly with higher #NLSs, apart from a single outlier. This trend was also observed for the initial import rate, which reports on the influx of capsids into the nucleus at the onset of the experiment.

Sample	I_{max}	k (1/min)	$T_{1/2}$ (min)	Init rate (#/min)
MS2_S37P 18 NLSs	5	0.040	17	0.16
MS2_S37P 20 NLSs	14	0.042	16.5	0.43
MS2_S37P 23 NLSs	28	0.040	17	0.73
MS2_S37P 29 NLSs	60	0.034	20	1.39
MS2_S37P 38 NLSs	44	0.025	28	0.87
I53-47 18 NLSs	6	0.038	18	0.4
I53-47 22 NLSs	6	0.036	19	0.35
I53-47 25 NLSs	14	0.057	12	0.87
I53-47 29 NLSs	4	0.095	7	0.35
I53-47 32 NLSs	10	0.059	12	0.45
I53-47 44 NLSs	12	0.050	14	0.5
MS2 100 NLSs	14	0.026	27	0.06

TABLE 3.3: Parameters obtained from fits of nuclear import kinetics. The average corrected nuclear fluorescence was fitted with an inverse exponential and the two parameters I_{max} and k were extracted. $T_{1/2}$ is the half–life of the saturation process, calculated from k. The initial rate was extracted by fitting the first 4 data points to a linear function.

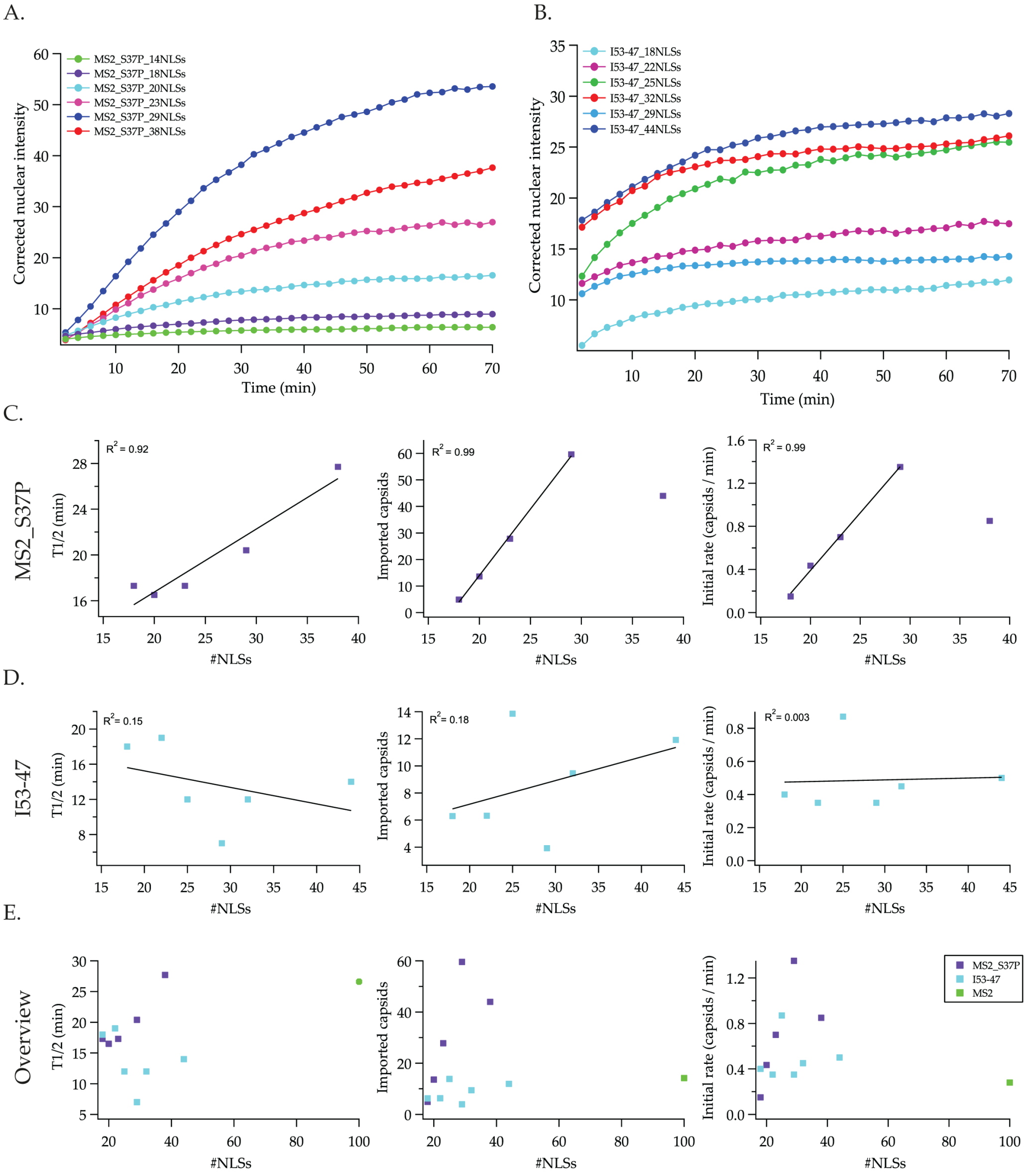

FIGURE 3.18: Corrected nuclear import kinetics of MS2_S37P (A) and I53-47 (B) capsid samples, for different #NLSs present on the cargo surface. (C) Fitting parameters for the MS2_S37P capsid samples. Half–life of nuclear import (left) and saturation value (center) for the nuclear intensity obtained from fitting the kinetic curves with an inverse exponential. Initial rate extracted from a linear fit of the first 4 data points (right). (D) Fitting parameters for the I53-47 capsid samples. (E) Overview of all kinetic parameters for the 3 differently sized capsids (MS2_S37P, I53-47, MS2).

For the 23 nm I53-47 capsid, I observed a much weaker trend of the import efficiency with different #NLSs (see Figure 3.18 B and D). The results suggests a very weak dependence of the import kinetics on NLSs for this larger cargo, as exemplified by the poor R^2 values of the linear fits in Figure 3.18D. In addition, the I53-47 capsids were much less efficient compared to the MS2_S37P ones, as can be seen by comparing the number of imported capsids for the two cargoes in Figure 3.18E (middle panel). In order to further characterize the nuclear import efficiency of the

I53-47 capsids, I calculated the nucleocytoplasmic ratio, which quantifies the degree of signal enrichment into the nucleus compared to the cytoplasm. As can be seen in Figure 3.19, I53-47 capsids reach at most a 2–fold enrichment (plot on the left), whereas MS2_S37P samples can surpass a 10–fold enrichment (plot on the right). The results thus show an overall less efficient import for the larger I53-47 capsids, which results in the import of 5 times less cargoes for a similar #NLSs.

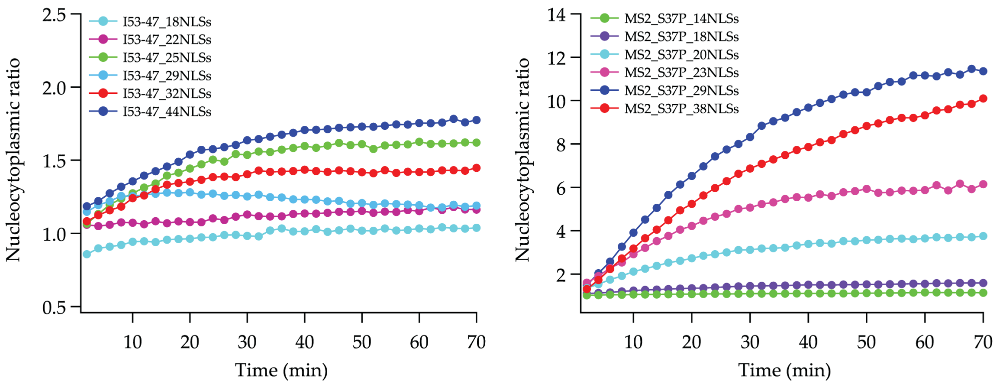

FIGURE 3.19: Nucleocytoplasmic ratio of I53-47 (left) and MS2_S37P (right) capsid samples. The average ratio of nuclear and cytoplasmic capsid signal was computed for each sample at every time step using the segmentation masks for the regions of interest.

For the 28 nm MS2 capsid I could not characterize a set of NLS–dependent import kinetics, as only the sample with 100 NLSs showed detectable bulk nuclear signal. Nevertheless, I could quantify the kinetics of this single import–competent capsid and compare them with the smaller ones (see Figure 3.18E) and Table 3.3. From this comparison, MS2 import appears to be very inefficient, as exemplified by its low nuclear intensity (comparable to the I53-47 and 1/5 lower than MS2_S37P samples) and import rates (an order of magnitude slower than most of all other capsids).

The ensemble kinetics experiments, coupled with a custom image analysis pipeline and precise characterization of the samples via FCS measurements, allowed me to quantitatively compare for the first time import properties of large cargoes spanning a size range of 18–28 nm. I found that MS2_S37P capsids have nuclear import kinetics which are very sensitive to #NLSs, increasing linearly in efficiency with the number of signals coupled on the cargo. I also observed that the samples which were more efficiently imported required longer time to reach saturation of import. The larger I53-47 capsids were overall less efficient and also insensitive to changes in the #NLSs, perhaps due to changes in the import mechanism (see Discussion). Lastly, the very large MS2 capsid was highly inefficient even with 100 NLSs on its surface. Overall, NLSs seem to play a crucial role in regulating the number of cargoes that can be imported through the NPC for capsid sizes < 20 nm. In the case of larger cargoes, the effect of the increased size causes a drastic drop in efficiency, largely insensitive to #NLSs.

Saturation behaviour of the kinetic curves

In all previous ensemble kinetic experiments I observed saturation of the nuclear signal over time, which was dependent on import efficiency. MS2_S37P capsids with a high #NLSs and efficient accumulation into the nucleus required longer time to reach saturation compared to less efficient ones (see kinetic plots in Figure 3.18). I then sought to investigate the possible mechanism behind these different behaviours. The observed saturation of the nuclear intensities indicates that a condition is reached where no more cargoes appear to be imported. This could arise as a result of different mechanisms: for instance, nuclear import could become arrested as a consequence of some transport component becoming depleted. Additionally, an equilibrium between cargo influx and "leaking out" could be achieved, or the capsids might "clog" the pores. First, I tested the possibility that some components of the transport mix could run out during the experiment. Kinetic curves measured in presence of excess impα or with an energy regenerating system (to regenerate ATP levels) did not show substantial differences (see supporting data in Appendix A).

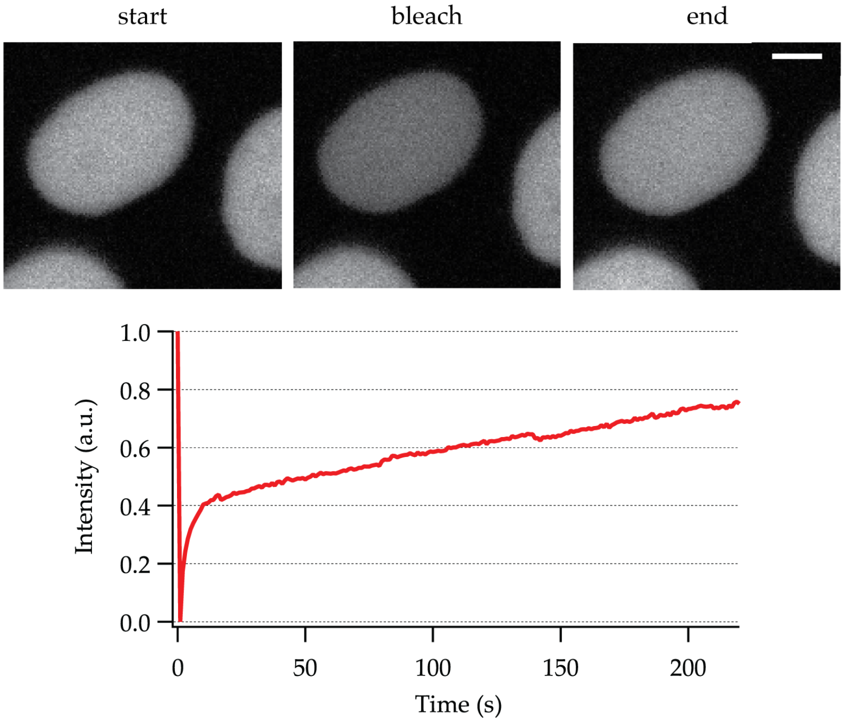

FIGURE 3.20: Whole nucleus FRAP of MBP–IBB. The top part shows confocal images of the cells right before and after bleaching, and at the end of the FRAP experiment. The bottom part shows the normalized plot of fluorescence recovery in the nucleus. The scale bar corresponds to 5 μm.

In order to test whether the transport process was arrested or rather had reached equilibrium through a balance of import and "leak–out" of cargoes, I performed FRAP (Fluorescence Recovery After Photobleaching) in cells incubated with a small model cargo IBB–MBP (Maltose Binding Protein). If transport would be completely halted, then even for this small cargo no recovery of fluorescent signal would be observed. The results shown in Figure 3.20 demonstrate how, after 50 minutes of incubation with the cargo (at which point saturation has been reached), transport is still active. In fact, even after bleaching the entire nucleus, a relatively fast recovery of the nuclear signal is observed.

However, in similar whole–nucleus bleaching experiments with the MS2_S37P capsids, I did not observe recovery after 50 min of transport time (monitoring the signal for up to 15 min). I reasoned that the large cargoes might induce a gradual "clogging" of the NPCs, as capsids with an insufficient #NLSs to cross the permeability barrier would still be strongly targeted to the nuclear envelope. These cargoes might accumulate at the NPCs with high affinity and gradually block passage of other molecules. This could also explain why the saturation occurs at a faster timescale for samples with lower #NLSs, as these could contain a higher fractions of capsids unable to effectively cross the permeability barrier.

To test this hypothesis, I performed FRAP of nuclear envelope regions in cells incubated with MS2_S37P capsids to measure whether the cargo would still be dynamic. In case of "clogging", the population of capsids stably bound at the nuclear envelope would be bleached and no recovery of the signal should be observed. I compared two samples, with 38 and 20 NLSs, which had shown a different saturation behaviour in the ensemble kinetics experiments (the lower NLS one saturated earlier). At different time points, I bleached a small nuclear envelope region and recorded the recovery of fluorescence for 15 min. I had to constrain bleaching and imaging to a very small region, in order to minimize fluorescence recovery arising from nuclear redistribution of the sample. Due to this constraint, the FRAP curves were relatively noisy however I observed that they were reproducible. The results are shown in Figure 3.21: for both samples a minor recovery was observed after 10 min of incubation. After 30 or 50 min, the capsid with 20 NLSs did not show any recovery, indicating that no "unbleached" capsids could bind to the nuclear envelope. For the 38 NLS sample, some recovery was still be observed. These preliminary experiments thus indicate that NPC "clogging" could at least partially contribute to the saturation of cargo nuclear intensity. As a higher #NLSs correlates with more efficient import, this would explain why "clogging" is not as severe for these samples compared to the ones with lower #NLSs.

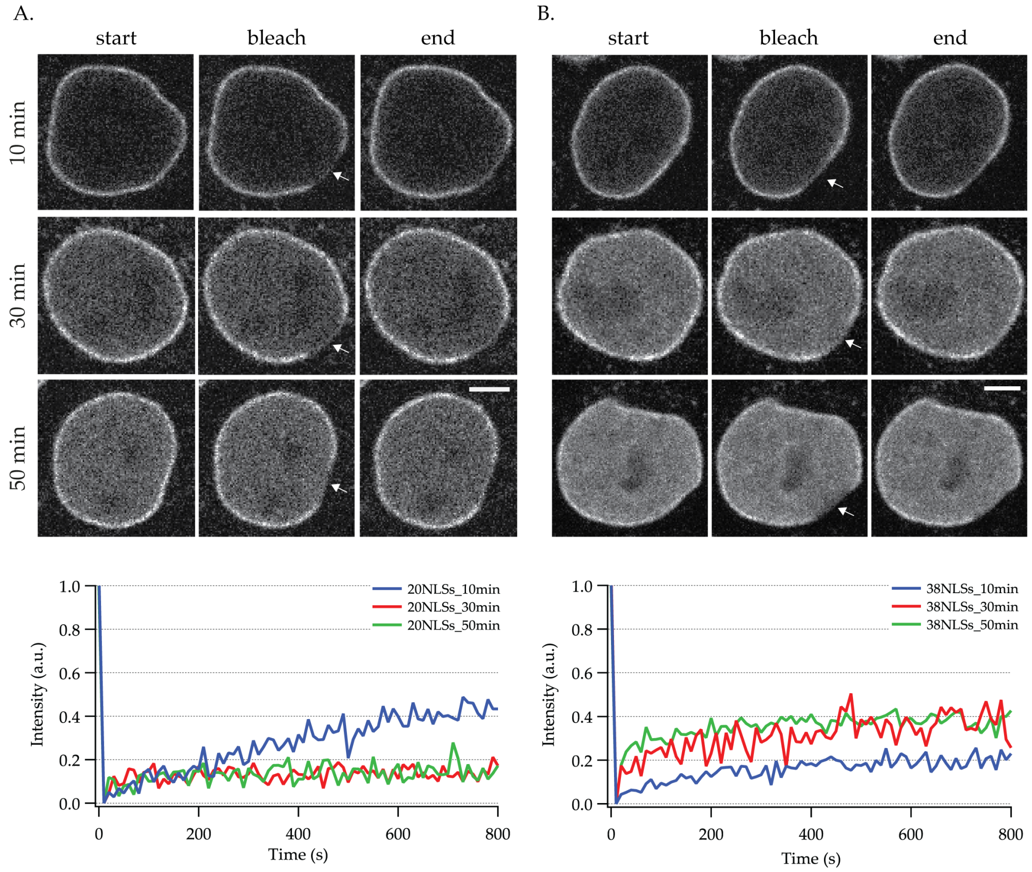

FIGURE 3.21: FRAP of MS2_S37P capsids at the nuclear envelope. Cells were incubated with MS2_S37P capsids with 20 NLSs (A) or 38 NLSs (B) and a small region of the nuclear envelope was bleached at different time points. The recovery of the fluorescence was then recorded for 15 min. The top part shows confocal images of the cells before and after bleaching, and at the end of the experiment. The bottom part shows normalized plot of fluorescence recovery in the bleached region for all samples. The scale bar corresponds to 5 μm.

3.2.3 Single–particle tracking

Ensemble nuclear import kinetics allowed me to achieve novel insights into large cargo import through the NPC, however knowledge of global import rates cannot report on the details of the import process steps on the molecular level. Single–particle tracking is a powerful technique that allows following dynamic processes with high spatio–temporal resolution. I optimized a custom TIRF/HILO microscopy setup and developed a specialized LabVIEW control software in order to perform high–resolution studies of nuclear import in cells.

A modular microscope control software for high–resolution imaging

For high–resolution imaging experiments, I optimized a custom–built TIRF/HILO microscopy setup (see Method chapter for more details). As the microscope was self–built, no control software was readily available. In order to achieve optimal operation of the microscope, all its parts have to be robustly coordinated: from

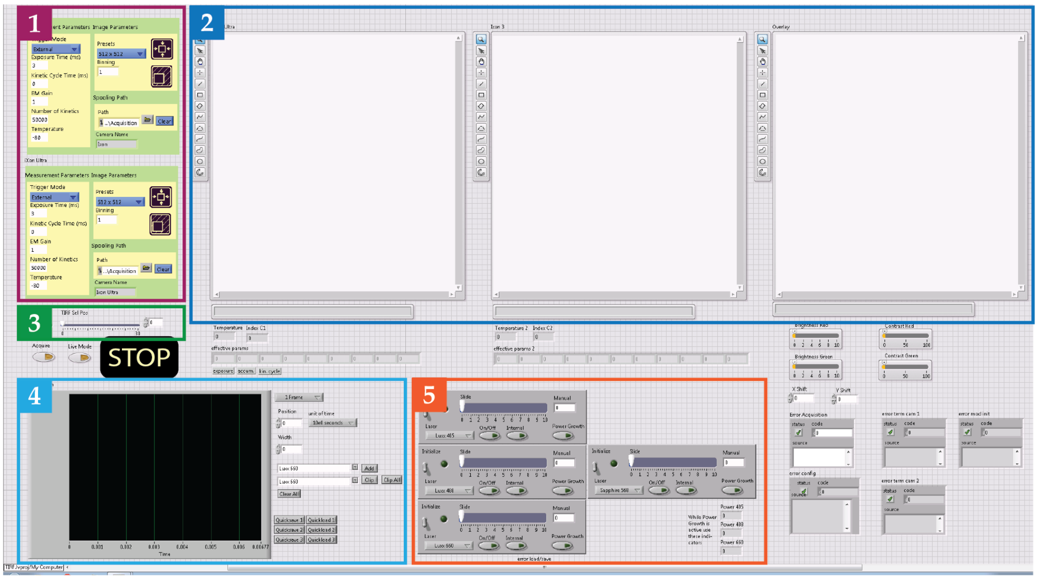

FIGURE 3.22: User interface of the microscope control software. Its main parts are the camera configuration module (1), the acquisition display (2), the TIRF/HILO angle control (3), the modulation module (4) and the laser control module (5).

the lasers to the cameras and the TIRF/HILO stage. In collaboration with an intern in the Lemke group (Kai Karius), I developed a LabVIEW software to control the self–built setup. The main feature of the software design is its modularity: different "modules" are dedicated to controlling specific parts of the microscope, and this allows the software to be easily expanded or adapted to other setups. This is very appealing, as most self–built microscopes are typically under continuous development/improvement. I achieved this modularity by implementing a class–based structure, where each component of the microscope is described by a corresponding class. The most important classes of the microscope control software are:

- Camera class
- Camera configuration class
- Laser class
- Modulation class
- Stage class

Each class contains a group of attributes, which correspond to important properties of the object, and a group of functions which describe operations that can be performed on the object. For example, the laser class has attributes such as the laser ID, laser type (Omicron vs Sapphire), the maximum power and the current power. Some important functions in the laser class are initialization and termination functions to start/end communication with the lasers, function to read/write the status of the laser (power), and functions to change the status of the laser (increase/decrease power).

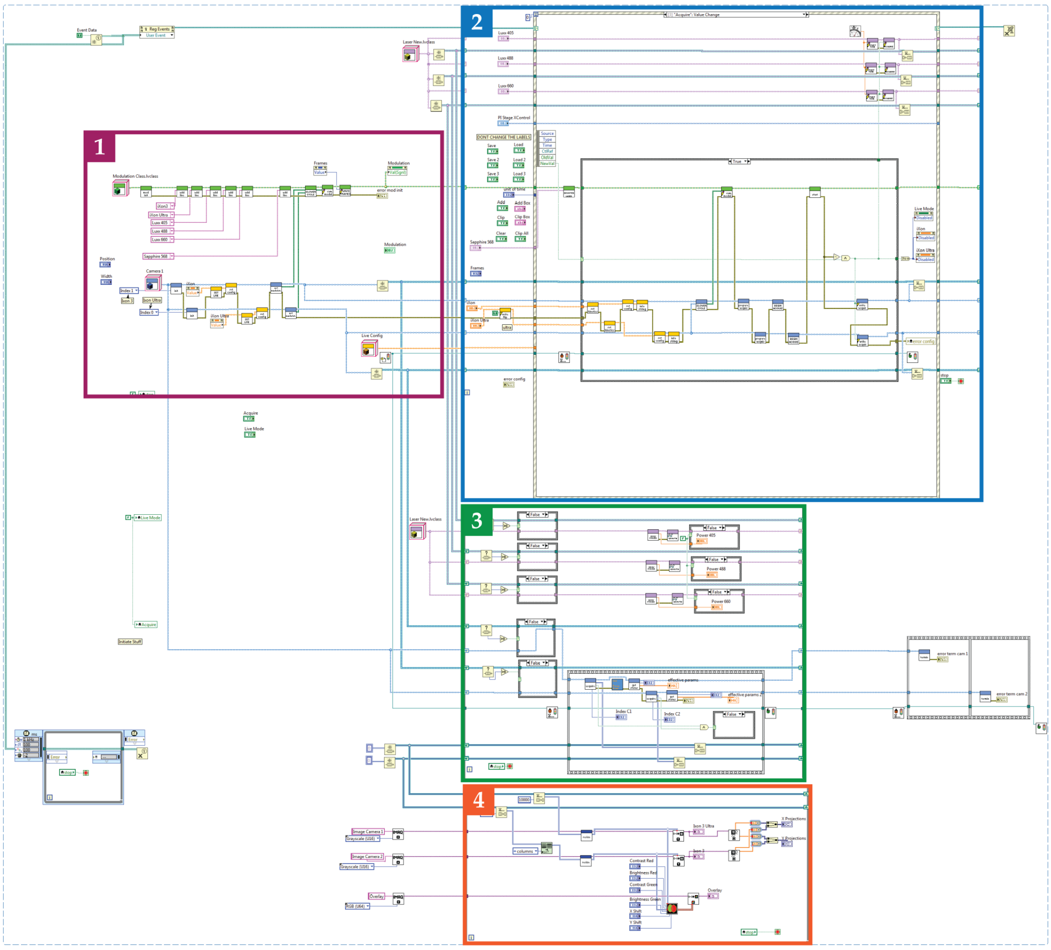

FIGURE 3.23: Block diagram showing the structure of the LabVIEW microscope control software. Its main parts are the initialization module (1), the loop to handle user interaction and set the configuration parameters (2), the main acquisition loop (3), and the loop to display the cameras overlay on the screen (4).

I then introduced Xcontrols based on the previously described class structure to provide a graphical user interface: for example each individual laser control in panel 5 of Figure 3.22 corresponds to an individual Xcontrol. I then linked together all program "modules" in a final control software which runs based on three main parallel loops: a loop for handling user interaction and set the configuration, a data acquisition loop and a loop to display the overlay of the two cameras onto the screen. An overview of the user interface of the final software is depicted in Figure 3.22, and the corresponding block diagram showing the main software modules is shown in Figure 3.23.

The most important functionalities offered by the software are the ability to control the TIRF/HILO angle, laser power, and imaging settings for the two cameras. Additionally, it enables the creation of custom modulation patterns for the lasers and cameras (panel 4 in Figure 3.22). This option is especially useful for applications where alternated laser excitation is needed, such as FRET measurements. Two key acquisition parameters for single–particle tracking are the exposure time (when the lasers are on and an image is being recorded) and the kinetic cycle (which includes the time required to transfer the data). By default, I programmed the lasers to be modulated in such a way that their emission is disabled during the data transfer time, to minimize unnecessary sample illumination and subsequent bleaching. It is also possible to set arbitrarily longer kinetic cycle times, for instance to introduce a "delay" in the image acquisition. Overall, the modular microscope control software I developed provides an ideal platform to perform high–resolution microscopy experiments with self–built setups.

Single–particle tracking of MS2_S37P capsids

Once I had developed a suitable TIRF/HILO setup and microscope control software, I could employ them to study large cargo transport at high spatiotemporal resolution. I performed single–particle tracking of permeabilised cells incubated with 2-3 nM MS2_S37P capsids and transport protein mix. I focused on the capsid sample with 29 NLSs as it had an optimal balance of high nuclear import and brightness. Imaging was carried out in a small area of 64x64 pixel to allow reaching fast acquisition rates. A reference image of the nuclear envelope from fluorescently labelled impβ was recorded at the beginning and at the end of each tracking experiment, to confirm absence of substantial drift. Tracking settings had to be tested and optimized, as I had no prior knowledge of the timescale of single capsid interaction with the NPCs: the kinetics data could be compatible with dwell times of the order of ms or s, and large cargoes characterized in literature also span this wide range of dwell times.

Initially I tested a fast acquisition with 2 ms exposure time and 3 ms kinetic cycle, however the tracks I obtained were very short and I could not detect any crossing events or interactions at the NPCs. The settings which I ultimately chose to adopt were an exposure time of 2 ms and kinetic cycle of 20 ms, to minimize sample bleaching and be able to capture longer interaction events. A representative cell with tracks acquired over a 15 min experiment is shown in Figure 3.24 A (tracks are overlaid in red on the impβ reference). I analyzed the tracks with a self–written routine in IgorPro (see Methods for more details). Briefly, I fitted the nuclear envelope position from the impβ image with a spline. I then classified the tracks according to their proximity to the envelope reference and whether they crossed it.

The analysis revealed the presence of a population of tracks interacting with the nuclear envelope (highlighted in blue in the right panel of Figure 3.24 A). I computed the mean squared displacement of this class of tracks and compared it with the one corresponding to tracks not interacting with the nuclear envelope. As can be seen in Figure 3.24 B, the interacting tracks are characterized by a much more confined diffusive motion compared to the non–interacting ones. The average dwell time (track length) of the interacting tracks was slightly longer than the ones further away from the nuclear envelope, on the order of 100 ms (see right panel in Figure 3.24 B). I also performed a jump distance analysis, which informs on the probability that a particle starting in position 0 is found within a shell of radius r and a width dr after a time Δt. For all tracks in each class, I computed the distance between each successive pair of positions and analyzed the distribution of such jump lengths. The results are shown in Figure 3.24 C: the interacting tracks are characterized by low jump distances (< 1 pixel), whereas for the non–interacting ones a second population of more motile particles (jump distance $\approx$ 4 pixels) is also found. This is reflected in the two–component Gaussian fit of the histogram on the right.

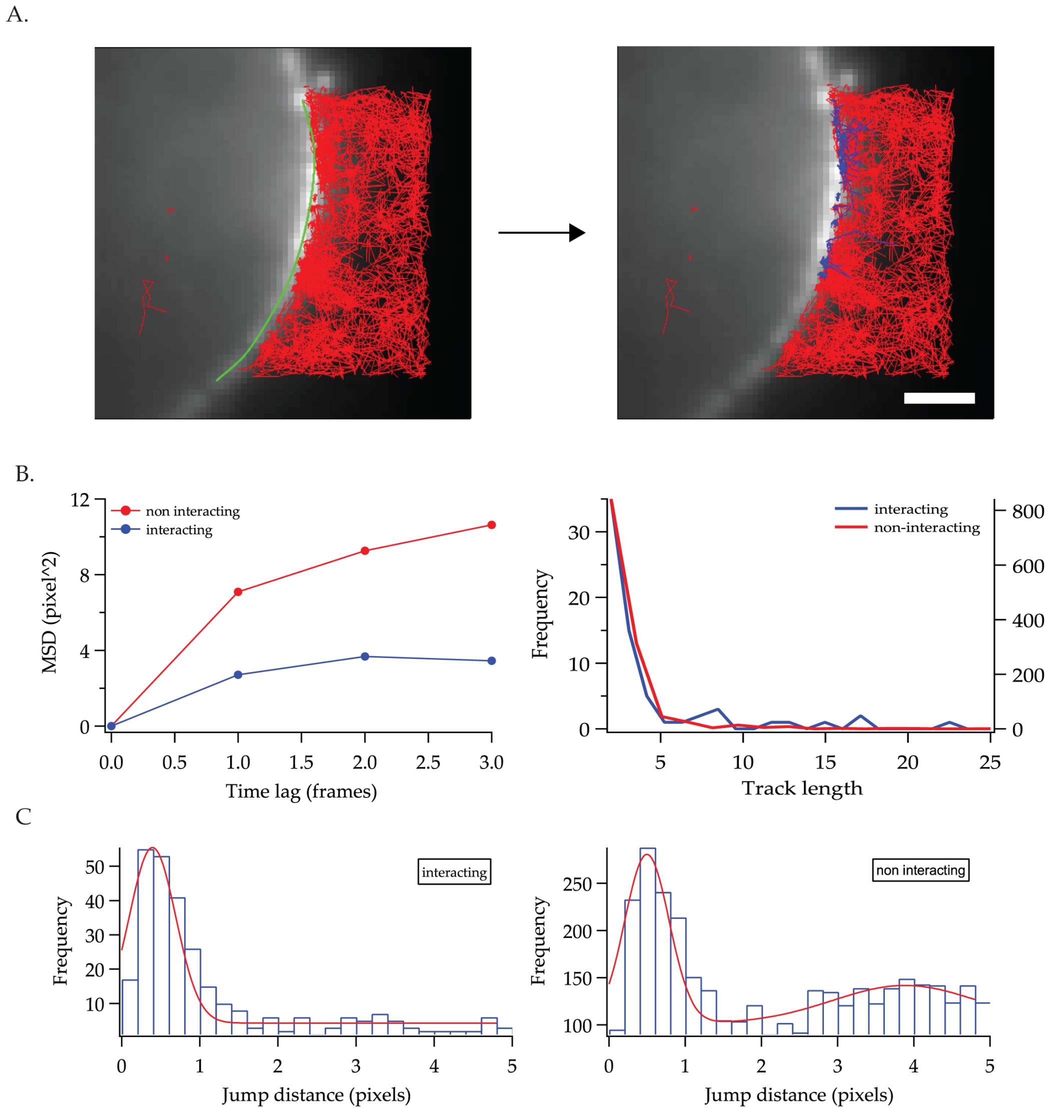

FIGURE 3.24: Single–particle tracking of MS2_S37P capsids. (A) Grayscale image of the reference impβ envelope image. The fitted envelope is highlighted in green and all reconstructed tracks are overlaid in red. On the right, filtered tracks which interact at the nuclear envelope are highlighted in blue. The scale bar corresponds to 500 nm. (B) Mean squared displacement (left) and dwell time (right) for tracks interacting or non–interacting with the NPCs. (C) Jump distance distribution for the two classes of tracks.

Due to the low throughput of the single–particle experiments (where a very low concentration of capsids are used), I could so far only analyze ≈ 80 interacting tracks out of thousands total tracks, therefore these analyses will benefit from more statistical validation. Nevertheless, I could identify a population of capsid tracks interacting with NPCs and characterized by extremely confined diffusive motion and an average dwell time of ≈ 100 ms. As it is extremely challenging to capture the undocking events at the pore (once undocked, the cargoes can rapidly diffuse out of focus), I currently cannot assign these long–lived events to import events with absolute certainty. A larger dataset or a more precise method of assigning import events (i.e. via a specific reporter – see Discussion) will make the interpretation of tracking experiments stronger. Nevertheless, the measured dwell time can likely be taken as a representative average duration of the transport events. In fact, faster acquisition rates down to 3 ms did not result in the observation of crossing or docking events. If, on the other hand, the crossing events were to occur on a much longer timescale, the current settings should have allowed their detection. In fact, each cell was observed for at least 15 min and I checked that substantial bleaching (to 10% of the initial intensity) only occurred over the course of hundreds of seconds.

3.3 Large cargo localization at the NPC

The ensemble transport experiment results highlighted that for samples which did not display detectable bulk nuclear import, strong nuclear envelope targeting was still observed. It was thus crucial to investigate whether this targeting arose from a biological interaction of the cargo with the NPC, or rather from a non–specific sticking to the nuclear envelope. A better description of this phenomenon could also help in understanding the reasons behind the incapacity of some large cargoes to efficiently enter the nucleus. In order address this question, I sought to achieve a more detailed understanding on the capsid localisation at the nuclear envelope. As both the capsid and the NPC are below the diffraction limit size, it was necessary to employ a super–resolved approach. I focused on the HBV capsid, which was the most extreme case as it did not present bulk nuclear import under any of the transport conditions tested.

I performed dual-color super-resolution imaging of cells incubated with HBV capsids and then stained with antibodies against a Nup of interest. Conveniently, specific antibodies are available for several Nups of known location at the NPC, providing an ideal reference. I used STORM imaging with spectral demixing of capsids labelled with CF680 and secondary antibody–AF647 to obtain simultaneous imaging of the two dyes using a single excitation laser (see Methods for more details). Images acquired in TIRF mode allowed me to visualize the bottom of the nucleus, where the capsids appear to be specifically docked at the centre of the NPCs stained with anti–Nup153 antibodies (see Figure 3.25).

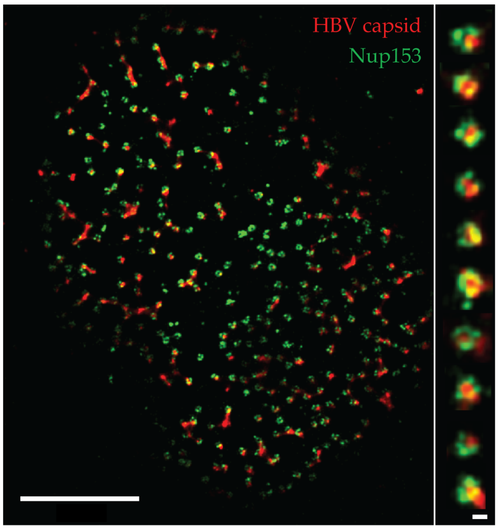

FIGURE 3.25: Dual–color SRM of HBV capsid and Nup153 localization in TIRF mode. After the transport experiment with HBV capsids, cells were fixed and Nup153 was labelled with immunostaining. Dual–color images were taken in TIRF mode to visualize the bottom footprint of the nuclear envelope. The scale bar corresponds to 2 μm. Panels on the right side show zoom–in pictures of single NPCs (scale bar corresponds to 50 nm).

I then carried out super–resolution imaging with HILO illumination to visualize the cross section of the nuclear envelope and obtain the relative localisation of the HBV capsid and a Nup of interest along the transport axis. Performing this experiment with different anti–Nup antibodies, I extracted an average profile calculated from the nuclear envelope (see Figure 3.26) for 4 target Nups. HBV capsids largely colocalized with Nup358 on the cytoplasmic side of the NPC and with mAB414, which stains FG-Nups in the permeability barrier. Compared to the localization of anti–ELYS (in the nuclear ring) and Nup153 (part of the nuclear basket) immunostainings, the capsid localization was shifted towards the cytoplasm. I could thus determine from the relative localizations that the HBV capsids were approximately located between the cytoplasmic filaments and the FG–Nup barrier.

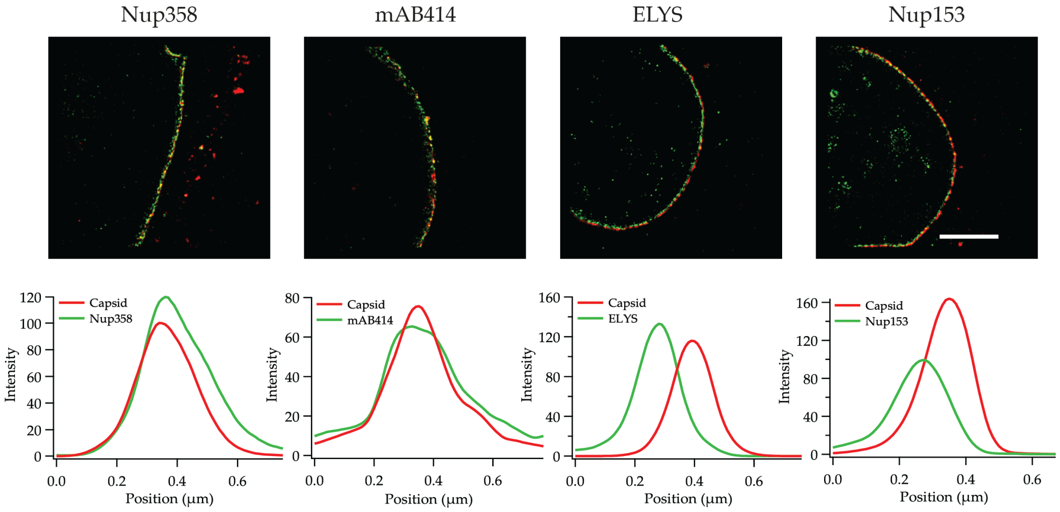

FIGURE 3.26: Dual–color SRM of HBV capsid and Nups localization. After the transport experiment with HBV capsids, cells were fixed and a Nup of interest was labelled with immunostaining. Dual–color images were taken in HILO mode to visualize the envelope cross section. The scale bar corresponds to 5 μm.

The super–resolution microscopy results indicated that the HBV capsids, despite being unable to productively enter the nucleus, are specifically docked on NPCs. Furthermore, I determined that the capsids were located between the cytoplasmic filaments and the central FG–barrier: an intriguing hypothesis is that the large cargoes interact with the permeability barrier in virtue of the many imp molecules bound to them. These findings support the biological relevance of the capsid samples: even in absence of observed bulk import (where one of many transport steps could fail, such as barrier crossing) there is clearly a specific interaction with the pore, indicating that the docking step is successful.

4 Discussion

Among the thousands of molecules which continuously shuttle between the cytoplasm and the nucleus through NPCs, one important class is represented by large cargoes. Transport of particles > 15 nm occurs for instance in mRNPs export (an essential step for gene expression in eukaryotes), in the export of large pre–ribosomal subunits during maturation and in the infection pathway of several viruses. One striking example is the HBV, which exploits the impα–impβ mediated import pathway and has been found to cross the NPC with its 36 nm capsid intact. Despite their importance, the properties and requirements for the transport of such large particles through the NPC permeability barrier are still poorly understood. In particular, it is likely that these cargoes require multivalent binding of several NTRs to interact with the FG–Nups in the central NPC channel and be efficiently transported. However, the dual role of size and multivalent NTR binding on the cargo surface have so far not been investigated systematically. Given these open questions, the main aim of this thesis was to quantitatively characterize the nuclear import kinetics of large cargoes according to their size and number of exposed NLSs. In order to do so, a suitable system was required where these key properties could be tuned and controlled quantitatively.

My first aim was to develop large model cargoes to study the interplay of size and #NLSs on nuclear transport of large cargoes. I decided to focus on capsid–like particles: in section (4.1) I will discuss the advantages of this system compared to alternative methods and the final strategy I employed to develop a large cargo "toolkit". Once I had established an adequate large cargo model, I then employed it to study the import properties in permeabilized cell assays. This allowed me to characterize the effect of size and #NLSs on the cargo localization and nuclear import kinetics. Furthermore, to go beyond the global kinetics, I developed a microscopy setup and control software suitable for dual–color high–resolution imaging. I used it to perform single–particle tracking and study import events of individual cargoes: I will discuss the outcome and implications of these experiments in section 4.2. During the transport experiments with the different large cargoes, I observed very strong targeting to the nuclear envelope, especially for samples which were unable to accumulate efficiently into the nucleus. In order to better understand this behaviour, I sought to analyze the cargo localization at the NPC at a high resolution. I will discuss the results of these experiments in section 4.3. Lastly, in section 4.4 I will discuss the outlook of this research, focusing on some remaining open questions which would be important to address in the future.

4.1 A large cargo "toolkit" for nuclear transport studies

One key issue which has so far prevented a quantitative understanding of large cargo import into the nucleus is the unavailability of a suitable system to study the effect of size and #NLSs on nuclear transport. Multimeric proteins such as the pentameric nucleoplasmin or the tetrameric β–galactosidase have been employed to address this question [98, 104], however the number of NLSs that can be titrated is typically quite low (< 5), and the size of these cargoes is relatively small (β–gal is only 9 nm on its narrow side). In addition, these systems cannot be easily built up to achieve cargoes of different sizes in the range of biologically relevant large cargoes. Functionalized QDs or gold particles have also been used as model systems [103, 93], however it can be very challenging to obtain particles homogeneous in size [120], and extensive functionalization (often including a protein coating) are typically required. For instance, QDs 18 nm in size and functionalized with IBBs did not display any bulk nuclear import (accumulation of capsids in the nucleus, as for example detectable with confocal microscopy), and only few rare events could be characterized with single–particle tracking [103].

In order to address these limitations I sought to develop a "toolkit" of large cargoes with tunable NLS exposure, based on virus–like particles. Many viral capsids can be purified in high amounts from bacterial, yeast or insect cells, thanks to the ability of viral coat proteins to spontaneously self-assemble. These particles are devoid of any viral genome and can be engineered to expose signals on their surface or encapsidate different materials. They have been studied as possible biocompatible delivery agents since the 1990s [121] for applications such as the delivery of nanoparticles, chemotherapeutic drugs, siRNAs, and protein toxins to cells [122] (see [123] for a review) and also as vaccines [124] (for example, several licensed HPV and HBV vaccines are based on recombinant expression of viral–like particles).

I therefore reasoned that viral capsids could also represent an ideal platform to develop "tunable" large cargoes for nuclear transport studies. I started from the 36 nm HBV capsid, one the largest cargo ever found to be able to cross the NPC [93] which exploits exposure of NLS sequences in its core protein to hijack the nuclear transport machinery and be imported [92]. As my main goal was to quantitatively characterize nuclear import of large model cargoes, I used a truncated version of the HBV core protein lacking its native NLS and engineered classical NLSs on the capsid surface using different strategies (see Figure 3.1). This allowed me to establish a protocol for capsid functionalization based on a minimal modification of the core protein: I used a single cysteine mutation to couple a dye or NLS peptide to the core proteins, obtaining capsids with a mixture of both tags on their surface (Figure 3.2) This construct presents several improved features compared to a previous HBV–derived capsid (Splitcore–NLS) developed by Niccolò Banterle in the Lemke group [125]. Its size is similar to the wild–type HBV (the Splitcore–NLS size was substantially enlarged by a GFP fusion), the capsid can be labelled with small and bright photostable dyes (ideal for high–resolution studies) and the number of NLS peptides on the cargo surface can be tuned.

As one key interest of my work is the interplay of size and exposed #NLSs, I then aimed to expand the large cargo toolkit with smaller capsids to be compared with HBV. This was also motivated by the fact that HBV import was extremely inefficient and therefore challenging to characterize. I turned to the MS2 bacteriophage, which has a 28 nm diameter capsid assembled from a single protein, and had previously been shown to tolerate surface mutations [117]. An additional advantage of this system is that a single point mutation was previously found which alters capsid assembly and results in the formation of 18 nm particles [118]. I could apply the surface functionalization pipeline I developed for HBV also to the MS2 capsids, obtaining samples with a wide range of NLS exposure (Figure 3.3). As the two MS2 capsid variants displayed dramatically different nuclear import properties, I sought to investigate a cargo that could bridge their sizes. I turned to *de novo* designed capsids developed in the Baker's group [105], and focused on the I53–47 capsid variant which is 23 nm in diameter. This capsid could also be successfully functionalized with NLSs following the double–labelling protocol (Figure 3.4). The final "toolkit" I developed thus consisted of more than 20 capsid–derived cargoes of different sizes, spanning a range from 18 to 36 nm (see Figure 3.5 for an overview) and with a number of NLSs from 0 to 120 (Table 3.1).

Even though the labelling procedure required a certain degree of optimization, it was typically possible to obtain a #NLSs in the desired range, with the exception of very high values that require an almost total saturation of the labelling sites and are therefore harder to achieve. One specific issue I had to face was that the NLS peptides and the dyes compete for the same labelling sites, which makes it hard to strike an ideal balance of the two (high NLS samples will often turn out to be quite dim). Using a direct fusion of NLS–dye peptide resulted in precipitation/aggregation issues during labelling and even trace contaminations of the fluorescent free peptide strongly accumulated to the nucleus, interfering with the interpretation of the fluorescence signal measured in the experiments. Increasing the number of surface mutation could potentially alleviate this problem and allow coupling of even more surface tags, however it could be challenging to find additional mutations that maintain capsid stability. Additionally, the presence of unassembled capsid protein contaminations labelled with both NLS and dye could cause background nuclear fluorescence (the same issue which was observed for the NLS–dye peptide). On the contrary, the labelling approach where NLS peptide and dye are reacted independently with capsid proteins containing a single labelling site ("mixed" labelling) is robust against the presence of unassembled capsid protein contaminations.

As size plays an crucial role in the efficiency of nuclear import, it is important to stress that the cargo sizes refer always to the "naked" capsid, but the effective size of the capsid–impα–impβ complex will be larger. For example, QDs functionalized with IBB and bound to ≈ 40 impβ had an average diameter increase of 12 nm [103] and incorporation of impα and impβ onto nucleoplasmin–coated gold particles resulted in an average 1.9–3.3 nm protein coat [93]. In preliminary DLS measurements performed on capsids pre–incubated with impα and impβ, I observed a shift in the average diameter of approximately 10 nm (not shown). It is likely that the bound importins form a "shell" surrounding the capsid: it would be interesting to achieve a more precise measurement of complex size and also image its structure via EM. In addition, it would be informative to estimate and confirm the number of bound impα and impβ molecules per capsid: as they have a high affinity ($K_d \approx 20nM$) [126] and are always pre–incubated in experiments, the NLSs should be completely saturated, however it could be that the importin coverage is limited by steric issues. The precise conformation of the trimeric transport complex is not very well characterized, especially for multimeric cargoes, but it was found to have substantial conformation flexibility by small–angle X–ray scattering [127]. It is thus likely that such flexibility enables multiple importins to be accommodated on the capsid surface. Furthermore, the large cargoes I employed do not have a saturating #NLSs (typically they are less than half of the total sites available) and in this range the number of bound NTRs clearly correlates with the #NLSs.

Finally, a point which would merit further investigation is a characterization of the capsids beyond their #NLSs. In this work, I focused on two specific parameters (size and #NLSs), but it is becoming more and more clear that many factors affect the nuclear import properties of cargoes. For instance, the residues present on the cargo surface can highly influence its hydrophobicity and charge, altering the transport behaviour dramatically (as has been recently shown for a simple GFP–based cargo [41]). As the capsids have a complex surface composition profile, displaying patches of both positively and negatively charged, hydrophobic and hydrophilic amino acids, it might be hard to link their surface landscape to their nuclear import properties. An alternative strategy would be to utilize the labelling strategy presented here to tag the capsids to differently modified peptides (i.e. strongly charged, or hydrophobic) and study the influence of these on their transport behaviour. However, the effect of these modification might not be very prominent for the capsid cargoes. In fact, samples with a sufficiently high #NLS are likely going to be covered by an importin "shell", which would substantially shield the effect of other surface properties.

4.2 Effect on multiple NLSs on large cargo import

Once I had established a suitable large cargo "toolkit", I employed it to study the nuclear import properties of the different capsids in permeabilized cells. The choice of this type of assay is ideal if one wishes to have as much control as possible on the system, as all the components necessary for nuclear transport are separately purified and then added to the cells at known concentrations.

Minimum #NLSs required for bulk nuclear import

Initially, I tested the different capsid samples and focused on characterizing their nuclear targeting and bulk import with confocal microscopy. In absence of NLSs on their surface, the cargoes did not bind to the nuclear envelope. When tagged with NLSs, the capsids were targeted to the nuclear envelope and displayed different degrees of accumulation into the nucleus (Figures 3.6, 3.7, 3.8 and 3.9). I found that a minimal number of surface NLSs was required in order to achieve bulk import of the cargoes into the nucleus. Capsids with lower #NLSs could bind to NPCs (as observed by their strong accumulation at the nuclear envelope), however they were unable to cross the permeability barrier and enter the nucleoplasm. This result is consistent with observations made for the tetrameric β–gal cargo, where a single transportin molecule was found to be sufficient for binding, but not for barrier crossing [104]. The minimum #NLSs which I found to be required for bulk import into the nucleus is summarized in Figure 3.10. Strikingly, this threshold value increased non–linearly with cargo size: from a minimum of approximately 15 NLSs in the case of the 18 nm capsid to 90-100 NLSs for a 10 nm larger cargo. For the 36 nm HBV, I could test capsids with only up to 120 NLSs and these did not show any bulk nuclear accumulation: it is possible that an even higher number is required for this cargo, or perhaps even the small modification on the HBV core protein rendered this capsid less efficient than the wild–type counterpart. HBV constructs based on the Splitcore concept (Figure 3.1 A) or with a direct NLS insertion in the core protein (Figure 3.1 B) did not show any nuclear import, despite having a total number of 240 NLSs. However, the Splitcore is larger in size compared to the wild–type HBV and the NLS inserted in the core protein might not be able to efficiently bind impα due to steric limitations. An alternative scenario, supported by findings from coarse–grained simulations of cargo transport [100], is that an optimal "sweet spot" of #NLSs exists for different cargo sizes, as too many NLSs might result in cargo entrapment at the NPC. Nevertheless, the observation that large cargoes might require such an high number of NLSs is unprecedented and gives important insight on what might be expected in the case of other physiologically relevant large cargoes.

An intriguing interpretation of the different transport behaviour observed in the cellular experiments can be drawn in terms of energetic requirements of the process. A larger cargo will have to pay a higher entropic cost in order to displace

FG–Nups in the central channel, and will subsequently require more bound impβ to interact with the permeability barrier and compensate the entropic cost via enthalpy. The energy barrier "felt" by cargoes of different sizes due to this entropic effect has been investigated by coarse–grained simulations: one study looked at spherical cargoes up to 20 nm in diameter and found that the free energy "penalty" scaled with cargo surface area $G \approx D^2$ [100]. Another study [128] looked at the interactions between nanoparticles and a surface-grafted polymeric substrate and also obtained a power–law increase in free energy with cargo diameter. The experimental dataset I presented in this thesis offers an unprecedented opportunity to test the prediction of these models in a previously unexplored size range: to this end, we have initiated a collaboration with the theoretical group of Prof. Zilman. Additionally, integrating the experimental data with a quantitative model as the ones described above would allow us to extrapolate the results obtained to any spherical cargo of sizes 18-28 nm.

Efficiency of import in relation to cargo size and #NLSs

In order to quantify the effect of size and different #NLSs on the capsid import kinetics, I developed an automated time–lapse confocal imaging pipeline to monitor nuclear accumulation over time. I analyzed the images with a self–written routine to segment different regions of interest (nucleus, nuclear envelope and cytoplasm – see Figure 3.12) and quantify the average capsid signal present in them over time (Figures 3.13,3.14 and 3.15). Due to the different sample brightnesses, it was necessary to devise a correction strategy in order enable quantitative comparison of the nuclear intensities. Precise protein and dye quantification were impaired due to the biochemical challenges posed by the capsid samples (low concentration, low absorbance at 280 nm, presence of scattering in absorbance measurements). To address these issue, I employed FCS (a spectroscopy technique) to directly measure the number of capsids present in solution and their brightness. I performed FCS measurements on a custom–built confocal setup (Figures 3.16 and 3.17) and analyzed them to calculate the precise capsid concentration and number of dyes present in each sample (Table 3.2). This ultimately allowed me to correct and quantitatively compare the nuclear intensities of the different samples (Figures 3.18 A and B).

All import curves could be fitted by an inverse exponential function, representing a saturation process which eventually reaches a final nuclear intensity I_{max}:

$$I(t) = I_{max} * (1 - e^{-kt})$$

For the 18 nm MS2_S37P capsid I found that higher #NLSs correlated with both higher number of total imported particles and slower saturation kinetics (Figure 3.18 C). Specifically, the efficiency of import increased linearly with #NLSs ($R^2 = 0.99$), resulting in an up to 10–fold enrichment of signal in the nucleus compared to the cytoplasm (Figure 3.19). For the 23 nm I53-47 capsid, transport was overall less efficient (only up to a 2–fold nuclear enrichment) and largely insensitive to different

#NLSs, as exemplified by the poor R^2 values of the linear fits (Figure 3.18 D). Finally, comparing the 28 nm MS2 capsid sample that was bulk imported (100 NLSs) with the smaller cargoes (Figure 3.18 E) I found that its import was extremely inefficient. Its nuclear enrichment was comparable to the I53-47 capsids and its initial import rate were an order of magnitude slower than most other samples.
The rapid increase in the #NLSs required for bulk import, as well as the drastic drop in efficiency, might indicate the presence of a previously uncharacterized "second gate" mechanism at the NPC. Above a certain size threshold, the import process could become highly unproductive due to a drastic increase in the energetic cost of crossing. It is also possible that additional factors, such as dilation of the NPC scaffold, might play a role. The presence of a second transport "gate" could result in a "shielding" of the role of exposed #NLSs for cargoes above a certain size (see cartoon in Figure 4.1). All in all, the work presented in this thesis constitutes the most complete experimental study of the influence of size and #NLSs on large cargo transport to date.

Saturation of the import curves

The saturation behaviour of the nuclear import curves observed for the different large cargoes was also found in previous studies with smaller cargoes, where it was shown to arise from a balance of import and passive leak [38]. In the case of the capsids tested here, several hypotheses could explain the saturation behaviour and how it varied in relation to the #NLSs. One possibility is that one or more components of the transport mix would get depleted and result in an arrest of the active import process. Alternatively, an equilibrium could be reached between capsid import and back–leakage into the nucleus: a capsid fully decorated by impα–impβ molecules, once in the nuclear basket, could travel back into the cytoplasm if the bound importins are not immediately released by RanGTP. Lastly, capsids bound to the NPCs but unable to cross the permeability barrier due to an insufficient number of bound importins could build up and result in a gradual "clogging" of the pores.

In order to evaluate the likelihood of these different explanations for the saturation behaviour, I carried out several experiments. Control import assays performed with excess of different transport mix components did not present substantial differences (see supporting data in A), ruling out concerns regarding depletion issues. I then investigated the possibility that saturation arose from an equilibrium between cargo import and cargo "leak out". To do so, I tested whether saturation correlated with a more or less dynamic capsid localization by performing FRAP of the nuclear envelope signal at different time points (Figure 3.21). The population of capsids at the nuclear envelope appeared to be highly static, with little or no recovery occurring after the first 10 minutes of experiment. This lack of dynamics was most severe for samples that had an earlier saturation point, suggesting the existence of at least a partial "clogging" of the pores. Nevertheless, additional factors may also play a role: further experiments addressing the alternative hypotheses, as well as the integration of the experimental data with a theoretical model, could help shed light on the factors involved in the saturation of the import kinetics.

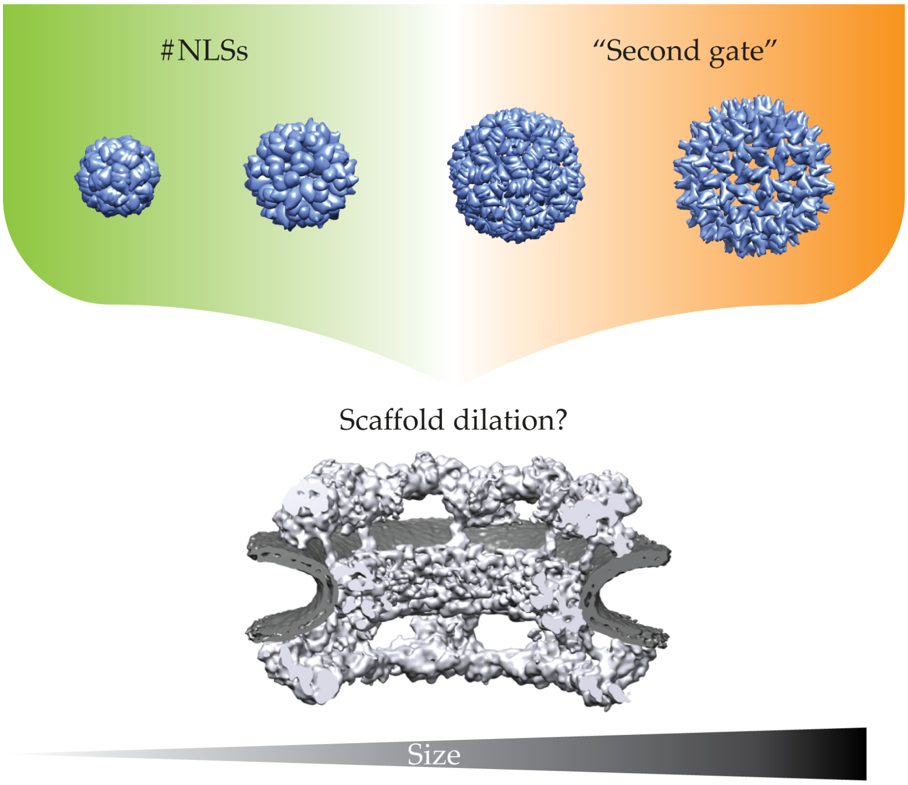

FIGURE 4.1: Cartoon of large cargo transport model. The interplay of two mechanisms regulates the nuclear import of large cargoes (> 15 nm). At the lower end of cargo sizes, the #NLSs dominates nuclear import efficiency. For increasing cargo sizes (≈ 25 nm), a "second gate" mechanism results in a rapid decrease of import efficiency, largely overtaking the effect of the #NLSs. This "second gate" might be due to an increased entropic cost of inserting the cargoes in the dense FG–barrier, or rely on structural changes in the NPC such as dilation of the scaffold.

Single–particle tracking of large cargoes

Key features of large cargo entry through the NPC cannot be studied by looking solely at bulk import kinetics. For instance, one cannot differentiate between the multiple steps of the import process (docking on the cytoplasmic side, barrier crossing and release). Additionally, it is challenging to correlate bulk import kinetics to the actual crossing time each capsid requires to enter the nucleus.

To address these open questions, I developed a dual–color TIRF/HILO microscopy setup and a specialized control software suitable for performing single–particle tracking experiments (Figure 3.23). I designed the software on the basis of a highly modular class structure, in order for it to be easily modified and expanded in the future according to improvements on the microscope. I used the self–built setup to track MS2_S37P capsids in cellular transport experiments with high spatiotemporal resolution. By using an exposure time of 2 ms and kinetic cycle of 20 ms I identified a population of capsids interacting at the nuclear envelope. These tracks were characterized by a much more confined diffusion compared to the non–interacting ones, as exemplified by their different mean squared displacement (see Figure 3.24 B). The capsids interacting at the envelope had an average dwell time at the pores of $\approx$ 100 ms. Even though I could not detect any undocking events, the measured dwell time is likely representative of the average transport events duration. In fact, when I acquired tracks at a much faster rate (down to a kinetic cycle of 3 ms), I could not observe crossing or docking events. If – on the contrary – transport would occur on a much longer timescale, the current settings should allow its detection, as substantial bleaching only occurred over the course of hundreds of seconds (as further discussed in Section 3.2.3).

Comparing the results of the MS2_S37P tracking with other cargoes characterized in literature, I found that the capsid dwell time is an order of magnitude longer than the one reported for a β–gal cargo (100 ms compared to 8 ms) [104]. However, this might not be surprising, given that β–gal is an elongated molecule only 9 nm wide on its narrow side. It could thus likely enter the NPC in a preferred orientation and its narrower side would be the effective dimension relevant for nuclear transport. In fact, it was already reported that elongated cargoes were transported faster than spherical ones for passive diffusion through the NPC [129]. When comparing the MS2_S37P results with the 18 nm QD, the dwell time appears an order of magnitude shorter [103]. As the two cargoes are close in size and in number of bound imp molecules, the discrepancy might be due to the different nature of the two samples. The QD, in fact, did not display bulk import even with 40 bound impβ (the authors could not show any ensemble import image), whereas bulk import of MS2_S37P capsids is highly efficient. It is possible that the extensive surface functionalization performed on the QD cargo rendered it less transport–competent.

As cargoes can rapidly diffuse out of focus once released in the nucleoplasm, it is extremely challenging to capture undocking events in single–particle tracking experiments. Due to this, I could not unequivocally assign the interacting tracks to successful import events. To address this issue and identify nuclear import events with higher confidence, I started to develop a FRET–based reporter of successful import. I first tested a strategy based on biotin–streptavidin binding: I pre–loaded the nucleus with fluorescently labelled streptavidin, and then added capsids tagged with a NLS–biotin peptide to the cells. Upon successful import, biotin and streptavidin should bind, bringing the fluorophores on the two proteins in close proximity and causing a FRET signal to be detected. However, this strategy was unsuccessful

as the streptavidin accumulated unevenly in the nucleus, with most signal localizing into bright spots. This likely prevented the availability of a pool of streptavidin molecules right at the site of cargo release (nuclear basket), and additionally the bright nuclear signal complicated the extraction of a clear FRET signal.
The second reporter approach I developed was based on exploiting the transport machinery itself, inspired by previous work where single–molecule FRET was used to detect the disassembly of impα from a small model cargo [80]. In this strategy, FRET between labelled capsid and impβ or impα and impβ bound on the capsid would undergo a sudden change upon barrier crossing and release of impβ in the nuclear basket. I successfully benchmarked both versions of this approach with *in vitro* FRET assays, however I could not reliably detect a FRET signal at the single–molecule level *in vivo*. Increasing the labelling on both binding partners and employing a capsid with a high #NLSs might improve the signal and allow the precise determination of import events via FRET.

4.3 Large cargo localization at the NPC

In the transport experiments I observed that samples which did not have substantial bulk import still displayed a strong targeting to the nuclear envelope. In order to understand the biological origin of this signal and whether it arose from a specific interaction with the NPC, I studied the precise capsid localization at the pore by performing dual–color super–resolution imaging of the cargo and different Nups of interest. Using STORM with spectral demixing, I simultaneously acquired super–resolved images of the two channels of interest in either TIRF or HILO mode (to observe the bottom or the cross section of the nuclear envelope, respectively). I focused on the HBV capsid, which was the most extreme cargo, as it did not display bulk nuclear import under any of the conditions tested despite having strong nuclear envelope targeting. Firstly, I imaged the bottom of the nucleus in order to observe the capsid localization compared to Nup153 (see Figure 3.25). Nup153 labelled via immunostaining displayed a clear ring–like pattern, and the capsids were distinctly localized at the centre of the NPCs, suggesting a specific interaction.

In order to visualize the capsid position along the transport axis, I imaged the nuclear envelope cross–section in HILO mode. I compared the capsid localization with 4 different target Nups, for which specific antibodies were available and the position at the NPC was previously characterized (see Figure 3.26). The HBV capsids largely co–localized with Nup358 (in the cytoplasmic side of the NPC) and mAB414 (an antibody that targets FG–Nups, enriched in the NPC permeability barrier). When compared with ELYS (part of the NPC nuclear ring) and Nup153 (part of the nuclear basket), the capsid localization was shifted towards the cytoplasm. I quantified the shift to be approximately 80–100 nm: this could likely be an overestimation due to the uncertainty of labelling the Nups via large primary and secondary antibodies.

Nevertheless, I could compare the relative localizations of HBV capsids and Nups, which were consistent and reproducible. The results indicated that the HBV capsids, despite being unable to productively enter the nucleus, are able to specifically "dock" on NPCs. Additionally, the capsids appeared to be located between the cytoplasmic filaments and the central FG—barrier: an intriguing hypothesis is that the large cargoes interact with the permeability barrier through the imp molecules bound to them. Overall these findings support the biological relevance of the capsid samples: even in absence of observed bulk import (where one of many transport steps could fail, such as barrier crossing) there is clearly a specific interaction with the pore, indicating that the docking step is successful. A better estimate of the absolute distances between cargo and Nups could be achieved by employing a more direct labelling method, such as labelled primary antibodies, nanobodies or ideally incorporation of an unnatural amino acid and labelling with small organic dyes via Amber suppression technology. The latter method however typically requires substantial testing to identify suitable mutation sites for labelling and only has a limited efficiency of 20%, resulting in incomplete labelling of the structure of interest.

Phosphorylated recombinant HBV capsids had previously been reported by EM to localize at the nuclear basket [93] and be "arrested" there, unable to disassemble. Similar results were also found for immature HBV capsids [94], and a model for capsids disassembly at the basket involving a direct interaction with Nup153 was proposed [95]. The discrepancy between my results, which locate the capsid on the cytoplasmic side, could be due to the different techniques employed. My super–resolution approach provides an average localization of the capsids across several pores, and few capsids localized at the basket would most likely be averaged out. On the other hand, in EM images, single particles can be localized and pinpointed. A more sophisticated pore–by–pore analysis routine could allow the extraction of even rare events from my imaging approach.

4.4 Outlook

In this work I have aimed at studying the nuclear import properties of large model cargoes, in a systematic and quantitative way. I developed a "toolkit" of capsid–like particles with tunable surface properties (# exposed NLSs) and characterized their behaviour in cells. The results obtained allowed me to determine the minimal requirement for bulk import of these large cargoes, as well as to quantify and extrapolate the import efficiencies in relation to the cargo size and #NLSs. This work has shed light for the first time on the basic requirements and features of large cargo transport through the NPC, however many aspects of this complex process still remain under–characterized.

A crucial open question when considering nuclear entry of large cargoes is what structural changes need to take place in the NPC itself in order to accommodate them. For the 28 nm MS2 bacteriophage, which is highly inefficient but still displays bulk nuclear import, clearly a substantial volume of FG–Nups will have to be displaced in order to fit the cargo–impα–impβ complex. This might explain why such a high number of NLSs (100) is required for successful nuclear import: only through multivalent binding of NTRs to FG–Nups can the entropic cost be compensated. It has been suggested that dilation of the NPC scaffold itself might also play a role in the transport of large cargoes such as the HBV. Even though dilated conformation of NPCs have been found in intact mammalian cells [12], most observations of scaffold plasticity were made in systems quite far from the physiological cellular state (i.e. spread–out nuclear envelope from *Xenopus* oocytes) [11, 10, 130]. Employing labelling techniques based on Amber suppression technology would allow tagging a Nup of interest with a minimal modification and with single amino acid precision [131]. The evidence for cargo docking at the NPC, even in absence of bulk nuclear import, opens the door for studying changes induced at the NPC also from cargoes which might not cross the barrier (as for example is one hypothesis for the intact HIV capsid [87]). Thanks to continuous development in super–resolution technologies, such as deconvolution-based algorithms for faster imaging [132, 133], it might soon be possible to perform imaging on live cell and capture the cargo crossing and NPC plasticity at the same time.

A key aspect of nuclear transport which I started to address is its multi–step nature. Knowledge of bulk import rates is very informative but cannot be easily related to the molecular steps of the import process. Dwell times of large cargoes at the NPC have been reported in a wide range, from few milliseconds to seconds, and how these depend on cargo size and properties is still largely an open question. In the future, it will be crucial to build on the newly developed microscopy and software platform and the preliminary single–particle tracking experiments presented in this thesis in order to dissect the different transport steps, from the initial interaction on the cytoplasmic side to release into the nucleoplasm. One especially intriguing direction will be to investigate the impact of the #NLSs on the permeability barrier crossing time: in fact, it could be envisioned that higher #NLSs allow more efficient import (number of successful crossing events), however the permeability barrier crossing step might be slower due to more interaction between NTRs bound to the capsid and FG-Nups. Knowledge of the detailed interaction steps, ideally in integration with theoretical models, will allow a better understanding of the complex multi–step import process.

4.5 Perspective: complementary *in vitro* study of a novel NPC permeability barrier model

The results outlined in this thesis highlight how the nuclear import of large cargoes in cells consists of several complex steps, from docking at the cytoplasmic face of the NPC, to crossing of the permeability barrier and finally release into the nucleus. In order to better dissect the contribution of these steps to large cargo import into the nucleus, a controllable *in vitro* system would be an ideal choice to complement the *in vivo* experiments. Therefore, I am currently seeking to dissect the specifics of cargo interaction with the FG–Nups in the NPC permeability barrier in a novel *in vitro* model. I am carrying out this project together with a postdoc in the Lemke group, Giorgia Celetti.

Our approach to the *in vitro* reconstitution of the NPC permeability barrier is based on the phase–separation properties of FG–Nups. As was discussed in the Introduction, several FG–Nups have been found to undergo phase transition into tough gels containing interlinked amyloid–like fibers and capable of displaying permeability barrier properties [19, 20, 21, 22, 23], which led to the formulation of the hydrogel model of the permeability barrier. According to this model, small molecules can freely diffuse through the meshwork of the hydrogel, whereas larger cargoes need to transiently dissolve the FG-FG network in order to cross the NPC. Recent studies into phase separation of biological systems have highlighted how this process often proceeds through intermediate steps, starting from liquid–liquid phase separation (LLPS) and then transitioning to more solid states due to "aging". We therefore reasoned that FG–Nups could also have an intermediate LLPS state, which has so far been elusive due to its transient nature (rapid aging into tough hydrogels).

Microfluidics is a powerful technology which allows the controlled processing of very small quantities of liquids. We sought to develop a microfluidic system to allow the study of early phases of FG–Nups phase separation. To do so, we optimized a microfluidic system for rapid buffer exchange of the protein solution, so that such proteins can phase separate into liquid droplets ready to be instantly interrogated about their permselectivity properties. An overview of the device is shown in Figure 4.2 A. The Nup solution flows from the sample inlet on the left, and rapid buffer exchange in the mixer region triggers its phase separation (a zoom–in image of the mixer is shown in Figure 4.2 B, top panel). Once FG–Nups have undergone phase–separation, the cargo flows from the cargo inlets and the interaction can be monitored in the snake–like observation channel by epi–fluorescence microscopy.

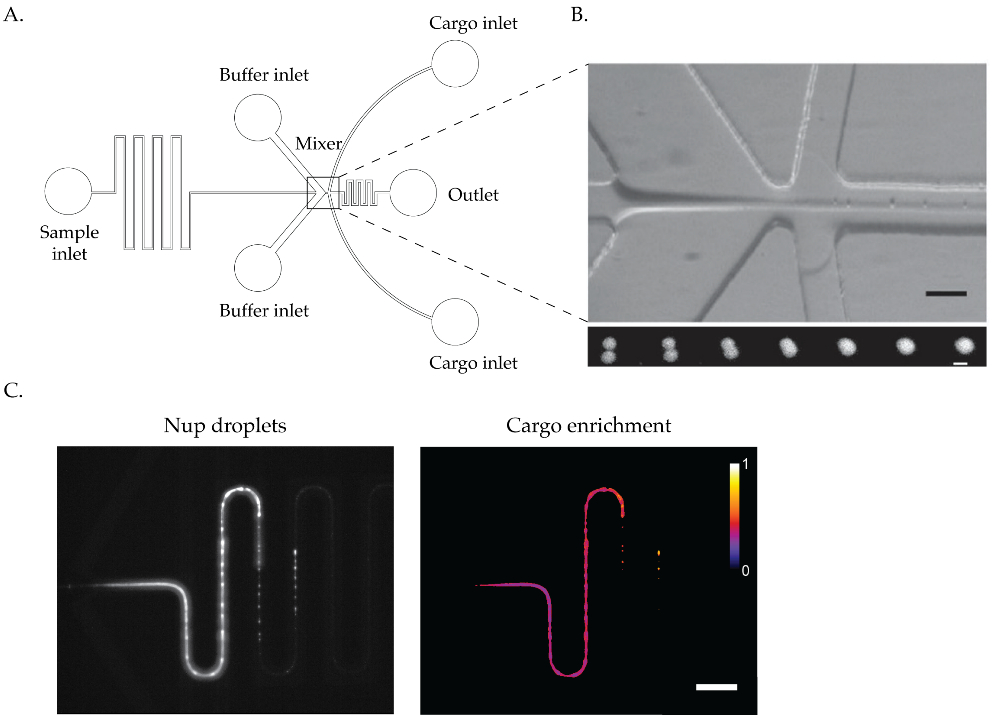

FIGURE 4.2: Microfluidic *in vitro* model of the NPC permeability barrier. (A) Scheme of the microfluidic device. (B) Zoom–in of the mixer region (top), the scale bar corresponds to 50 μm. Representative fusion events between FG–Nup49 droplets (bottom), the scale bar corresponds to 10 μm. (C) Interaction of HBV capsids with FG–Nup49 droplets. The left panel corresponds to the Nup fluorescence, the right one to the HBV enrichment in the droplets. This enrichment was calculated from an intensity ratio analysis of the Nup and cargo channels. The scale bar corresponds to 100 μm.

As a model of the permeability barrier, we used FG–Nup49, a Nup from *S. cerevisiae* that can form tough hydrogels *in vitro*. Strikingly, we could observe the formation of round Nup droplets right after the mixer. The droplets were in a liquid state, as they were observed to coalesce (fuse) and subsequently round up (see the bottom panel of Figure 4.2 B for snapshots of a droplet fusion sequence). We could also verify that the LLPS state of FG–Nups recapitulated several aspects of the NPC permeability barrier, namely: exclusion of passive cargoes > 40 kDa and NLS–bearing cargoes in absence of NTRs and efficient recruitment of NLS–bearing cargoes in presence of NTRs. This data represents the first evidence of a previously undescribed LLPS state of the NPC permeability barrier.
We then tested the interaction of the droplets with HBV capsids (Splitcore construct). As can be seen in Figure 4.2 C, the capsids were recruited into the Nup droplets. The left panel shows the Nup fluorescence and the right panel the enrichment of capsid into the droplet, quantified by an intensity ratio of the Nup and cargo channels.

These experiments offer an initial view on the potential of complementing *in vivo* nuclear import experiments with the *in vitro* permeability barrier model. Interestingly, the *in vitro* tests revealed that large HBV capsids could penetrate FG–Nups droplets, whereas no import was observed for these same cargoes *in vivo*. This suggests that insertion of the capsid into the FG–Nup permeability barrier might not be the limiting step, and this might rather come from the confinement caused by the NPC scaffold. We are currently seeking to test the interaction of the other capsids with the FG–droplets, and investigate the role of #NLSs in this context. Correlating these results with the ones from the cellular transport assays will enable us to shed light on the basic properties that regulate the different steps of large cargo transport through the NPC. At the same time, the large cargoes developed in this thesis can be used to investigate the biological applicability of *in vitro* NPC permeability barrier models, which have so far mostly been characterized according to their interaction with NTRs.

Acknowledgements

I write, erase, rewrite
erase again, and then
a poppy blooms.

Hokushi

This thesis represents the culmination of four years of work and life, and many companions travelled by my side during this time. To all of them, I am extremely grateful.

Thanks to Edward, who welcomed me in his lab and gave me so many opportunities to grow during these years. I am grateful for his guidance and mentoring and for always motivating me. I would also like to thank the members of my thesis advisory committee Dr. Martin Beck, Dr. Peter Lenart and Prof. Dr. Ulrich Schwarz, for their continuous support and feedback on the project.

I am indebted to all past and present members of the Lemke group, who have made the lab a great place for me to work in these years. Thanks to Christine who patiently taught me how to work in a wet lab when I had never held a pipette in my hand before. Big thanks also go to Niccolò who guided me through the first year of my PhD. Thanks to Aritra, PiauSiong, Nataliia, Paul, Christopher, Daniel, Kai for being there during these years: I have learnt a lot from all of you. Special thanks to Gemma: I truly admire your critical scientific attitude and I've really enjoyed all the fun moments with you and Hernando in Heidelberg. Joana, thank you for being the best team–mate I could ever dream of having! You appeared at a very special turn of my project, and I am so glad I got the chance to work with you and be your friend. A big thank you to Iker, beloved bench–mate, motivating German course companion and extremely supportive friend. I will miss our scientific discussions at the corner and the crazy times together at Wilfred, but I am thrilled that our paths will cross again in the UK. Thanks to Sofya, for being a great companion during all these years: from countless hours spent in the TIRF, aligning the (damn) IR laser, to the wine festivals and the cultural discussions. To Giorgia, grazie for being such a caring and supportive friend every single day. We also had lots of fun together observing the "interesting" German behaviours at the pool!

I am extremely grateful to Agnes, Eva, Iria, Emma and Verena who warmly welcomed me in the outreach world. You passion and dedication to communicating science have been a never-ending source of inspirations during the last few years. Keep up with the good work! Special thanks also go to the many people whose work is essential to research at EMBL but is often under appreciated: the mechanical workshop, the Electron Microscopy and Advanced Light Microscopy facilities staff, the kitchen staff. Thanks to Dr. Rackwitz and Dr. Glas from PSL who put a lot of effort in troubleshooting the peptides that enabled this work. Thanks Thorlabs, for all the candy.

I want to thank Clotilde, Ania, Greyson and all the people from 2017 PBoC course, as well as the amazing instructors Rob, Hernan, Julie. We shared some crazy dream-like weeks in Woods Hole, between science and swimming in the ocean! I often think back to our time together and your kindness, generosity and enthusiasm whenever I need a "mood boost". Thanks Lauren, for being close to me even though we are so far away. I really wish we can continue to foster this connection in the future.

Thanks Jin for always being there in these last few years, I am so glad I could share this path with you. I will really miss our lunches together and all the heartfelt discussions about science and life. Thanks Ben end Emmy: I have loved our many thought-provoking discussion and I'm looking forward to many more to come!

A very special thank you goes to Celeste, Mariagrazia and Arianna. Even though we are now all scattered in different places, I really feel that our friendship has only grown deeper in the last few years, and every time we meet it's like no time passed at all! I am so happy to see just how far and in how many different directions we've travelled since our physics studies together. Thank you for your constant support, I can't wait to share what comes next with you. To Dom, thanks for always bringing me joy with your fun Japan and anime – themed messages. Arigatou gozaimasu!

Un forte abbraccio alla mia famiglia. Thanks to my amazing parents, who are always my inspiration. I am really grateful for their neverending trust in me and their support. Vi voglio un mare di bene.

To Fede, thank you for always being my anchor and making me laugh so much. I feel honored to share this life with you and I am proud of what we are building together. May we always follow our own compass, as "not all those who wander are lost".

A Appendix: supporting data

In order to validate the transport assays in permeabilized cells, I performed several controls. In particular, I carried out different experiments in order to rule out the possibility that saturation of the import curves arose from a major depletion of components in the transport mix. Including an ATP–regenerating system (see Methods for details of the composition) in the transport mix did not result in any substantial alteration of the import curves compared to the standard conditions (Figure A.1 A). Similar results were obtaines using a 2–fold excess of GTP (Figure A.1 B). Finally, I tested whether depletion of impα was the source of saturation, as its recycling factor CAS is not included in the transport mix. A 5–fold excess of impα did not result in substantial differences compared to the standard conditions (Figure A.1 C). These experiments thus allowed me to confirm that the saturation of import curves does not likely arise from depletion of transport mix components.

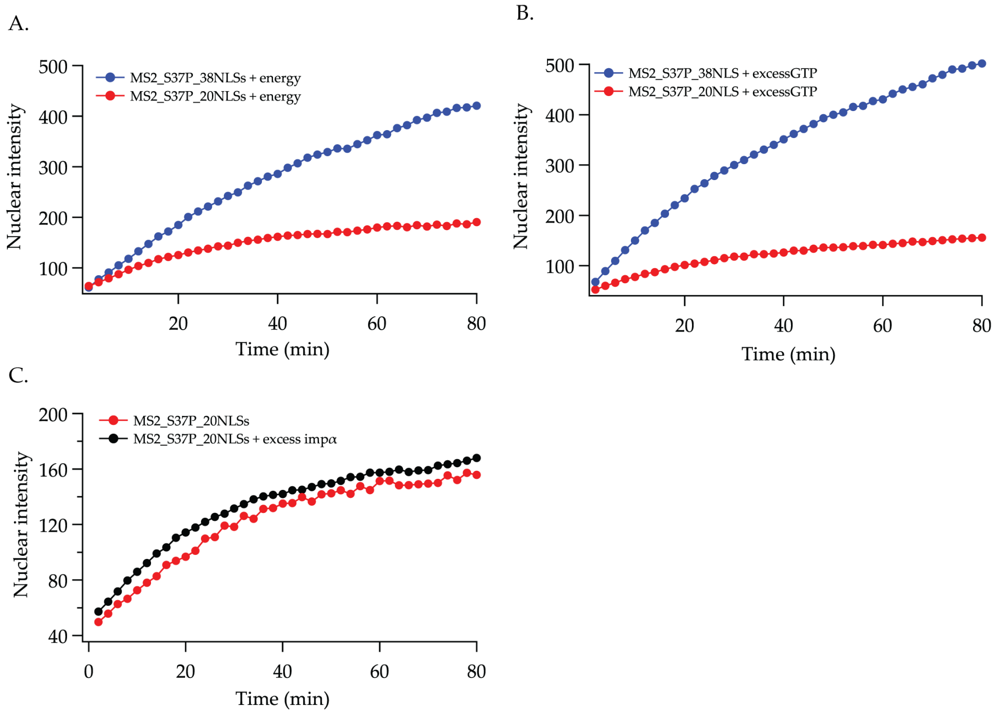

FIGURE A.1: Supporting data for transport assays. MS2_S37P capsid import was measured in presence of (A) ATP–regenerating system (see Methods for details of the components), (B) 2–fold excess of GTP and (C) 5–fold excess of impα. No substantial differences were detected compared to the standard conditions.

Bibliography

[1] R. Reichelt et al. “Correlation between structure and mass distribution of the nuclear pore complex and of distinct pore complex components”. In: *Journal of Cell Biology* 110.4 (1990), pp. 883–894.

[2] Nikta Fay and Nelly Panté. “Nuclear entry of DNA viruses”. In: *Frontiers in Microbiology* 6.MAY (2015), p. 467.

[3] Valerie Le Sage and Andrew J. Mouland. “Viral subversion of the nuclear pore complex”. In: *Viruses* 5.8 (2013), pp. 2019–2042.

[4] Maya Capelson and Martin W. Hetzer. “The role of nuclear pores in gene regulation, development and disease”. In: *EMBO Reports* 10.7 (2009), pp. 697–705.

[5] Anna Szymborska et al. “Nuclear pore scaffold structure analyzed by super-resolution microscopy and particle averaging”. In: *Science* 341.6146 (2013), pp. 655–658.

[6] Alexander Von Appen et al. “In situ structural analysis of the human nuclear pore complex”. In: *Nature* 526.7571 (2015), pp. 140–143.

[7] Daniel H. Lin et al. “Architecture of the symmetric core of the nuclear pore”. In: *Science* 352.6283 (2016), p. 308.

[8] Jan Kosinski et al. “Molecular architecture of the inner ring scaffold of the human nuclear pore complex”. In: *Science* 352.6283 (2016), pp. 363–365.

[9] Nelly Panté et al. “Interactions and three-dimensional localization of a group of nuclear pore complex proteins”. In: *Journal of Cell Biology* 126.3 (1994), pp. 603–617.

[10] Ivan Liashkovich et al. “Exceptional structural and mechanical flexibility of the nuclear pore complex”. In: *Journal of Cellular Physiology* 226.3 (2011), pp. 675–682.

[11] Rainer D. Jäggi et al. “Modulation of nuclear pore topology by transport modifiers”. In: *Biophysical Journal* 84.1 (2003), pp. 665–670.

[12] Julia Mahamid et al. “Visualizing the molecular sociology at the HeLa cell nuclear periphery”. In: *Science* 351.6276 (2016), pp. 969–972.

[13] Alessandro Ori et al. “Cell type-specific nuclear pores: A case in point for context-dependent stoichiometry of molecular machines”. In: *Molecular Systems Biology* 9.1 (2013), p. 648.

[14] Jenny E. Hinshaw and Ronald A. Milligan. “Nuclear pore complexes exceeding eightfold rotational symmetry”. In: *Journal of Structural Biology* 141.3 (2003), pp. 259–268.

[15] Michael P. Rout and Mark C. Field. “The Evolution of Organellar Coat Complexes and Organization of the Eukaryotic Cell”. In: *Annual Review of Biochemistry* 86.1 (2017), pp. 637–657.

[16] André Hoelz, Erik W. Debler, and Günter Blobel. “The Structure of the Nuclear Pore Complex”. In: *Annual Review of Biochemistry* 80.1 (2011), pp. 613–643.

[17] Shyamal Mosalaganti et al. “In situ architecture of the algal nuclear pore complex”. In: *Nature Communications* 9.1 (2018).

[18] K Ribbeck and D Gorlich. “Kinetic analysis of translocation through nuclear pore complexes”. In: *EMBO Journal* 20.6 (2001), pp. 1320–1330.

[19] Steffen Frey, Ralf P. Richter, and Dirk Görlich. “FG-rich repeats of nuclear pore proteins form a three-dimensional meshwork with hydrogel-like properties”. In: *Science* 314.5800 (2006), pp. 815–817.

[20] Steffen Frey and Dirk Görlich. “A Saturated FG-Repeat Hydrogel Can Reproduce the Permeability Properties of Nuclear Pore Complexes”. In: *Cell* 130.3 (2007), pp. 512–523.

[21] Aksana A. Labokha et al. “Systematic analysis of barrier-forming FG hydrogels from Xenopus nuclear pore complexes”. In: *EMBO Journal* 32.2 (2013), pp. 204–218.

[22] Sigrid Milles et al. “Facilitated aggregation of FG nucleoporins under molecular crowding conditions”. In: *EMBO Reports* 14.2 (2013), pp. 178–183.

[23] Hermann B roder Schmidt and Dirk Görlich. “Nup98 FG domains from diverse species spontaneously phase-separate into particles with nuclear pore-like permselectivity”. In: *eLife* 4 (2015), pp. 1–30.

[24] I a N G Macara et al. “Transport into and out of the Nucleus”. In: *Society* 65.4 (2001), pp. 570–594.

[25] Michael P. Rout et al. *Virtual gating and nuclear transport: The hole picture*. 2003.

[26] Reiner Peters. “Translocation through the nuclear pore complex: Selectivity and speed by reduction-of-dimensionality”. In: *Traffic* 6.5 (2005), pp. 421–427.

[27] Roderick Y.H. Lim et al. “Flexible phenylalanine-glycine nucleoporins as entropic barriers to nucleocytoplasmic transport”. In: *Proceedings of the National Academy of Sciences* 103.25 (2006), pp. 9512–9517.

[28] Roderick Y.H. Lim et al. “Nanomechanical basis of selective gating by the nuclear pore complex”. In: *Science* 318.5850 (2007), pp. 640–643.

[29] Justin Yamada et al. "A Bimodal Distribution of Two Distinct Categories of Intrinsically Disordered Structures with Separate Functions in FG Nucleoporins". In: *Molecular & Cellular Proteomics* 9.10 (2010), pp. 2205–2224.

[30] Samir S. Patel et al. "Natively Unfolded Nucleoporins Gate Protein Diffusion across the Nuclear Pore Complex". In: *Cell* 129.1 (2007), pp. 83–96.

[31] Iris Ben-efraim and Larry Gerace. "along the Pathway of Nuclear Import". In: *Cell* 152.2 (2001), pp. 411–417.

[32] Brook Pyhtila and Michael Rexach. "A Gradient of Affinity for the Karyopherin Kap95p along the Yeast Nuclear Pore Complex". In: *Journal of Biological Chemistry* 278.43 (2003), pp. 42699–42709.

[33] Sigrid Milles and Edward A. Lemke. "Mapping multivalency and differential affinities within large intrinsically disordered protein complexes with segmental motion analysis". In: *Angewandte Chemie - International Edition* 53.28 (2014), pp. 7364–7367.

[34] Larisa E. Kapinos et al. "Karyopherin-centric control of nuclear pores based on molecular occupancy and kinetic analysis of multivalent binding with FG nucleoporins". In: *Biophysical Journal* 106.8 (2014), pp. 1751–1762.

[35] Raphael S. Wagner et al. "Promiscuous binding of karyopherinβ1 modulates FG nucleoporin barrier function and expedites NTF2 transport kinetics". In: *Biophysical Journal* 108.4 (2015), pp. 918–927.

[36] Alan R. Lowe et al. "Importin-β modulates the permeability of the nuclear pore complex in a Ran-dependent manner". In: *eLife* 2015.4 (2015), pp. 1–24.

[37] Weidong Yang and Siegfried M. Musser. "Nuclear import time and transport efficiency depend on importin β concentration". In: *Journal of Cell Biology* 174.7 (2006), pp. 951–961.

[38] Benjamin L. Timney et al. "Simple kinetic relationships and nonspecific competition govern nuclear import rates in vivo". In: *Journal of Cell Biology* 175.4 (2006), pp. 579–593.

[39] Benjamin L. Timney et al. "Simple rules for passive diffusion through the nuclear pore complex". In: *Journal of Cell Biology* 215.1 (2016), pp. 57–76.

[40] Bracha Naim et al. "Cargo surface hydrophobicity is sufficient to overcome the nuclear pore complex selectivity barrier". In: *EMBO Journal* 28.18 (2009), pp. 2697–2705.

[41] Steffen Frey et al. "Surface Properties Determining Passage Rates of Proteins through Nuclear Pores". In: *Cell* (2018), pp. 202–217.

[42] Daniel Kalderon et al. "Sequence requirements for nuclear location of simian virus 40 large-T antigen". In: *Nature* 311.5981 (1984), pp. 33–38.

[43] Arie Kaffman et al. "The receptor Msn5 exports the phosphorylated transcription factor Pho4 out of the nucleus". In: *Nature* 396.6710 (1998), pp. 482–486.

[44] José Manuel Mingot et al. "Importin 13: A novel mediator of nuclear import and export". In: *EMBO Journal* 20.14 (2001), pp. 3685–3694.

[45] Makoto Kimura and Naoko Imamoto. "Biological Significance of the Importin-β Family-Dependent Nucleocytoplasmic Transport Pathways". In: *Traffic* 15.7 (2014), pp. 727–748.

[46] Noemi Fukuhara et al. "Conformational Variability of Nucleo-cytoplasmic Transport Factors". In: *Journal of Biological Chemistry* 279.3 (2004), pp. 2176–2181.

[47] Elena Conti, Christoph W. Müller, and Murray Stewart. "Karyopherin flexibility in nucleocytoplasmic transport". In: *Current Opinion in Structural Biology* 16.2 (2006), pp. 237–244.

[48] Jade K. Forwood et al. "Quantitative structural analysis of importin-β flexibility: Paradigm for solenoid protein structures". In: *Structure* 18.9 (2010), pp. 1171–1183.

[49] B Kobe. "Autoinhibition by an internal nuclear localization signal revealed by the crystal structure of mammalian importin α." In: *Nature structural biology* 6.4 (1999), pp. 388–397.

[50] Changxia Sun et al. "Choreography of importin-α/CAS complex assembly and disassembly at nuclear pores." In: *Proceedings of the National Academy of Sciences of the United States of America* 110 (2013), pp. 1584–93.

[51] Ki Lui and Ying Huang. "RanGTPase: A Key Regulator of Nucleocytoplasmic Trafficking". In: *Molecular and cellular pharmacology* 1.3 (2009), pp. 148–156.

[52] Dirk Görlich, Michael J. Seewald, and Katharina Ribbeck. "Characterization of Ran-driven cargo transport and the RanGTPase system by kinetic measurements and computer simulation". In: *EMBO Journal* 22.5 (2003), pp. 1088–1100.

[53] Richard Bayliss et al. "Crystallization and initial X-ray diffraction characterization of complexes of FxFG nucleoporin repeats with nuclear transport factors". In: *Journal of Structural Biology* 131.3 (2000), pp. 240–247.

[54] Richard Bayliss et al. "GLFG and FxFG nucleoporins bind to overlapping sites on importin-β". In: *Journal of Biological Chemistry* 277.52 (2002), pp. 50597–50606.

[55] Timothy A. Isgro and Klaus Schulten. "Binding dynamics of isolated nucleoporin repeat regions to importin-β". In: *Structure* 13.12 (2005), pp. 1869–1879.

[56] Iker Valle Aramburu and Edward A. Lemke. "Floppy but not sloppy: Interaction mechanism of FG-nucleoporins and nuclear transport receptors". In: *Seminars in Cell and Developmental Biology* 68 (2017), pp. 34–41.

[57] Sigrid Milles et al. "Plasticity of an Ultrafast Interaction between Nucleoporins and Nuclear Transport Receptors". In: *Cell* 163.3 (2015), pp. 734–745.

[58] Loren E. Hough et al. "The molecular mechanism of nuclear transport revealed by atomic-scale measurements". In: *eLife* 4.September (2015), pp. 1–23.

[59] Piau Siong Tan et al. "Two Differential Binding Mechanisms of FG-Nucleoporins and Nuclear Transport Receptors". In: *Cell Reports* 22.13 (2018), pp. 3660–3671.

[60] Barak Raveh et al. "Slide-and-exchange mechanism for rapid and selective transport through the nuclear pore complex". In: *Proceedings of the National Academy of Sciences* 113.18 (2016), E2489–E2497.

[61] H. G. Callan and S. G. Tomlin. "Experimental studies on amphibian oocyte nuclei I. Investigation of the structure of the nuclear membrane by means of the electron microscope". In: *Proceedings of the Royal Society of London. Series B - Biological Sciences* 137.888 (1950), 367 LP –378.

[62] Douglass J. Forbes, Marc W. Kirschner, and John W. Newport. "Spontaneous formation of nucleus-like structures around bacteriophage DNA microinjected into Xenopus eggs". In: *Cell* 34.1 (1983), pp. 13–23.

[63] Manfred J. Lohka and Yoshio Masui. "Formation in vitro of sperm pronuclei and mitotic chromosomes induced by amphibian ooplasmic components". In: *Science* 220.4598 (1983), pp. 719–721.

[64] J. Julian Blow and Ronald A. Laskey. "Initiation of DNA replication in nuclei and purified DNA by a cell-free extract of Xenopus eggs". In: *Cell* 47.4 (1986), pp. 577–587.

[65] Bastian B. Hülsmann, Aksana A. Labokha, and Dirk Görlich. "The permeability of reconstituted nuclear pores provides direct evidence for the selective phase model". In: *Cell* 150.4 (2012), pp. 738–751.

[66] Aizhan Bestembayeva et al. "Nanoscale stiffness topography reveals structure and mechanics of the transport barrier in intact nuclear pore complexes". In: *Nature Nanotechnology* 10.1 (2015), pp. 60–64.

[67] Armin Kramer et al. "Atomic force microscopy visualises a hydrophobic meshwork in the central channel of the nuclear pore". In: *Pflugers Archiv European Journal of Physiology* 456.1 (2008), pp. 155–162.

[68] C. Kambach and I. W. Mattaj. "Intracellular distribution of the U1A protein depends on active transport and nuclear binding to U1 snRNA". In: *Journal of Cell Biology* 118.1 (1992), pp. 11–22.

[69] Stephen A. Adam, R S Marr, and L Gerace. "Nuclear protein import in permeabilized mammalian cells requires cytoplasmic factors". In: *J. Cell. Biol.* 111.3 (1990), pp. 807–816.

[70] Katharina Ribbeck et al. "The translocation of transportin-cargo complexes through nuclear pores is independent of both Ran and energy". In: *Current Biology* 9.1 (1999), pp. 47–50.

[71] C. M. Feldherr. "the Effect of the Electron-Opaque Pore Material on Exchanges Through". In: *The Journal of cell biology* 25 (1965), pp. 43–53.

[72] Philip L. Paine. "Nucleocytoplasmic movement of fluorescent tracers microinjected into living salivary gland cells". In: *Journal of Cell Biology* 66.3 (1975), pp. 652–657.

[73] Philip L. Paine, Leonard C. Moore, and Samuel B. Horowitz. "Nuclear envelope permeability". In: *Nature* 254.5496 (1975), pp. 109–114.

[74] David S. Goldfarb et al. "Synthetic peptides as nuclear localization signals". In: *Nature* 322.6080 (1986), pp. 641–644.

[75] R Peters. "Nucleo-cytoplasmic flux and intracellular mobility in single hepatocytes measured by fluorescence microphotolysis." In: *The EMBO Journal* 3.8 (1984), pp. 1831–6.

[76] Dirk Görlich et al. "A novel class of RanGTP binding proteins". In: *Journal of Cell Biology* 138.1 (1997), pp. 65–80.

[77] Ronen Benjamine Kopito and Michael Elbaum. "Reversibility in nucleocytoplasmic transport." In: *Proceedings of the National Academy of Sciences of the United States of America* 104.31 (2007), pp. 12743–8.

[78] Gerhard J. Schütz et al. "Single molecule microscopy of biomembranes. (Review)". In: *Molecular Membrane Biology* 17.1 (2000), pp. 17–29.

[79] W.E. Moerner. "Optical measurements of single molecules in cells". In: *TrAC Trends in Analytical Chemistry* 22.8 (2003), pp. 544–548.

[80] Changxia Sun et al. "Single-molecule measurements of importin alpha/cargo complex dissociation at the nuclear pore." In: *Proceedings of the National Academy of Sciences of the United States of America* 105.25 (2008), pp. 8613–8.

[81] Thomas Dange et al. "Autonomy and robustness of translocation through the nuclear pore complex: A single-molecule study". In: *Journal of Cell Biology* 183.1 (2008), pp. 77–86.

[82] W. Yang, J. Gelles, and S. M. Musser. "Imaging of single-molecule translocation through nuclear pore complexes". In: *Proceedings of the National Academy of Sciences* 101.35 (2004), pp. 12887–12892.

[83] Ulrich Kubitscheck et al. "Nuclear transport of single molecules". In: *The Journal of Cell Biology* 168.2 (2005), pp. 233–243.

[84] David Grünwald and Robert H. Singer. "In vivo imaging of labelled endogenous B-actin mRNA during nucleocytoplasmic transport". In: *Nature* 467.7315 (2010), pp. 604–607.

[85] Hans Mehlin, Bertil Daneholt, and Ulf Skoglund. "Translocation of a specific premessenger ribonucleoprotein particle through the nuclear pore studied with electron microscope tomography". In: *Cell* 69.4 (1992), pp. 605–613.

[86] Gary R Whittaker, Michael Kann, and Ari Helenius. "Viral entry into the nucleus". In: *Annual review cell developmental biology* (2000).

[87] Edward M. Campbell and Thomas J. Hope. "HIV-1 capsid: The multifaceted key player in HIV-1 infection". In: *Nature Reviews Microbiology* 13.8 (2015), pp. 471–483.

[88] Michael Kann, Andre Schmitz, and Birgit Rabe. "Intracellular transportof hepatitis B virus". In: *World Journal of Gastroenterology* 13.1 (2007), pp. 39–47.

[89] C T Yeh, Y F Liaw, and J H Ou. "The arginine-rich domain of hepatitis B virus precore and core proteins contains a signal for nuclear transport." In: *Journal of virology* 64.12 (1990), pp. 6141–6147.

[90] S G Eckhardt, D R Milich, and A. McLachlan. "Hepatitis B virus core antigen has two nuclear localization sequences in the arginine-rich carboxyl terminus." In: *Journal of virology* 65.2 (1991), pp. 575–582.

[91] a Zlotnick et al. "Localization of the C terminus of the assembly domain of hepatitis B virus capsid protein: implications for morphogenesis and organization of encapsidated RNA." In: *Proceedings of the National Academy of Sciences of the United States of America* 94.18 (1997), pp. 9556–9561.

[92] Michael Kann et al. "Phosphorylation-dependent Binding of Hepatitis B Virus Core Particles to the Nuclear Pore Complex". In: *The Journal of Cell Biology* 145.1 (1999), pp. 45–55.

[93] N. Pante. "Nuclear Pore Complex Is Able to Transport Macromolecules with Diameters of 39 nm". In: *Molecular Biology of the Cell* 13.2 (2002), pp. 425–434.

[94] B. Rabe et al. "Nuclear import of hepatitis B virus capsids and release of the viral genome". In: *Proceedings of the National Academy of Sciences* 100.17 (2003), pp. 9849–9854.

[95] André Schmitz et al. "Nucleoporin 153 arrests the nuclear import of hepatitis B virus capsids in the nuclear basket". In: *PLoS Pathogens* 6.1 (2010), e1000741.

[96] Susan K. Lyman et al. "Influence of cargo size on Ran and energy requirements for nuclear protein import". In: *Journal of Cell Biology* 159.1 (2002), pp. 55–67.

[97] R. Moussavi-Baygi et al. "Biophysical coarse-grained modeling provides insights into transport through the nuclear pore complex". In: *Biophysical Journal* 100.6 (2011), pp. 1410–1419.

[98] Colin Dingwall, Stephen V. Sharnick, and Ronald A. Laskey. "A polypeptide domain that specifies migration of nucleoplasmin into the nucleus". In: *Cell* 30.2 (1982), pp. 449–458.

[99] Katharina Ribbeck and Dirk Görlich. "The permeability barrier of nuclear pore complexes appears to operate via hydrophobic exclusion". In: *EMBO Journal* 21.11 (2002), pp. 2664–2671.

[100] Ali Ghavami, Erik Van Der Giessen, and Patrick R. Onck. "Energetics of transport through the nuclear pore complex". In: *PLoS ONE* 11.2 (2016), e0148876.

[101] Joseph M Kelich et al. "Super-resolution imaging of nuclear import of adeno-associated virus in live cells". In: *Molecular Therapy - Methods & Clinical Development* 2.August (2015), p. 15047.

[102] Siegfried M. Musser and David Grünwald. "Deciphering the Structure and Function of Nuclear Pores Using Single-Molecule Fluorescence Approaches". In: *Journal of Molecular Biology* 428.10 (2016), pp. 2091–2119.

[103] Alan R. Lowe et al. "Selectivity mechanism of the nuclear pore complex characterized by single cargo tracking". In: *Nature* 467.7315 (2010), pp. 600–603.

[104] Li Chun Tu et al. "Large cargo transport by nuclear pores: Implications for the spatial organization of FG-nucleoporins". In: *EMBO Journal* 32.24 (2013), pp. 3220–3230.

[105] Jacob B. Bale et al. "Accurate design of megadalton-scale two-component icosahedral protein complexes". In: *Science* 353.6297 (2016), pp. 389–395.

[106] Andreas Walker, Claudia Skamel, and Michael Nassal. *SplitCore: An exceptionally versatile viral nanoparticle for native whole protein display regardless of 3D structure*. 2011.

[107] Joseph R. Lakowicz. *Principles of Fluorescence Spectroscopy*. Second edition. New York : Kluwer Academic/Plenum, [1999] ©1999, 2006, p. 362. ISBN: 978-0-387-31278-1 (Print) 978-0-387-46312-4 (Online).

[108] Kirsten Bacia, Elke Haustein, and Petra Schwille. "Fluorescence correlation spectroscopy: Principles and applications". In: *Cold Spring Harbor Protocols* 2014.7 (2014), pp. 709–725.

[109] Makio Tokunaga, Naoko Imamoto, and Kumiko Sakata-Sogawa. "Highly inclined thin illumination enables clear single-molecule imaging in cells". In: *Nature Methods* 5.2 (2008), pp. 159–161.

[110] Graham T. Dempsey et al. "Evaluation of fluorophores for optimal performance in localization-based super-resolution imaging". In: *Nature Methods* 8.12 (2011), pp. 1027–1040.

[111] Ilaria Testa et al. "Multicolor fluorescence nanoscopy in fixed and living cells by exciting conventional fluorophores with a single wavelength". In: *Biophysical Journal* 99.8 (2010), pp. 2686–2694.

[112] Peter Dedecker et al. "Localizer: fast, accurate, open-source, and modular software package for superresolution microscopy". In: *Journal of Biomedical Optics* 17.12 (2012), pp. 1–5.

[113] F Birnbaum and M Nassal. "Hepatitis B virus nucleocapsid assembly: primary structure requirements in the core protein". In: *J Virol* 64.7 (1990), pp. 3319–30.

[114] A. Zlotnick et al. "Dimorphism of Hepatitis B Virus Capsids Is Strongly Influenced by the C-Terminus of the Capsid Protein". In: *Biochemistry* 35.23 (1996), pp. 7412–7421.

[115] P. A. Kratz, B. Bottcher, and M. Nassal. "Native display of complete foreign protein domains on the surface of hepatitis B virus capsids". In: *Proceedings of the National Academy of Sciences* 96.5 (1999), pp. 1915–1920.

[116] Francis A Galaway and Peter G Stockley. "MS2 Viruslike Particles: A Robust, Semisynthetic Targeted Drug Delivery Platform". In: *Molecular Pharmaceutics* 10.1 (2013), pp. 59–68.

[117] David S. Peabody. "A viral platform for chemical modification and multivalent display". In: *Journal of Nanobiotechnology* 1 (2003), pp. 1–8.

[118] Michael A. Asensio et al. "A Selection for Assembly Reveals That a Single Amino Acid Mutant of the Bacteriophage MS2 Coat Protein Forms a Smaller Virus-like Particle". In: *Nano Letters* 16.9 (2016), pp. 5944–5950.

[119] Gabriel L. Butterfield et al. "Evolution of a designed protein assembly encapsulating its own RNA genome". In: *Nature* 552.7685 (2017), pp. 415–420.

[120] Jan W Slot and Hans J Geuze. "A new method of preparing gold probes for multiple-labeling cytochemistry." In: *European journal of cell biology* 38.1 (1985), pp. 87–93.

[121] Min Wu, William L Brown, and Peter G Stockley. "Cell-Specific Delivery of Bacteriophage-Encapsidated Ricin A Chain". In: *Bioconjugate Chemistry* 6.5 (1995), pp. 587–595.

[122] Carlee E Ashley et al. "Cell-Specific Delivery of Diverse Cargos by Bacteriophage MS2 Virus-like Particles". In: *ACS Nano* 5.7 (2011), pp. 5729–5745.

[123] Robert L. Garcea and Lutz Gissmann. "Virus-like particles as vaccines and vessels for the delivery of small molecules". In: *Current Opinion in Biotechnology* 15.6 (2004), pp. 513–517.

[124] Joshua W. Wang and Richard B. S. Roden. "Virus-like particles for the prevention of human papillomavirus-associated malignancies". In: *Expert Rev Vaccines* 12.2 (2014), pp. 1–22.

[125] Niccolò Banterle. "Advanced Imaging of the Nuclear Pore Complex". PhD thesis. 2014.

[126] Michelle T. Harreman et al. “The auto-inhibitory function of importin ?? is essential in vivo”. In: *Journal of Biological Chemistry* 278.8 (2003), pp. 5854–5863.

[127] Jorge Falces et al. “Recognition of nucleoplasmin by its nuclear transport receptor importin α/β: Insights into a complete import complex”. In: *Biochemistry* 49.45 (2010), pp. 9756–9769.

[128] Chad Gu et al. “Free Energy of Nanoparticle Binding to Multivalent Polymeric Substrates”. In: *Journal of Physical Chemistry B* 121.26 (2017), pp. 6425–6435.

[129] Dagmar Mohr et al. “Characterisation of the passive permeability barrier of nuclear pore complexes”. In: *EMBO Journal* 28.17 (2009), pp. 2541–2553.

[130] Victor Shahin et al. “Steroids dilate nuclear pores imaged with atomic force microscopy”. In: *Journal of Cellular Physiology* 202.2 (2005), pp. 591–601.

[131] Ivana Nikić and Edward A. Lemke. “Genetic code expansion enabled site-specific dual-color protein labeling: Superresolution microscopy and beyond”. In: *Current Opinion in Chemical Biology* 28 (2015), pp. 164–173.

[132] Junhong Min et al. “FALCON: Fast and unbiased reconstruction of high-density super-resolution microscopy data”. In: *Scientific Reports* 4 (2014), p. 4577.

[133] Eran A. Mukamel, Hazen Babcock, and Xiaowei Zhuang. “Statistical deconvolution for superresolution fluorescence microscopy”. In: *Biophysical Journal* 102.10 (2012), pp. 2391–2400.